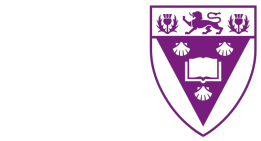

Variability Analysis of a Sample of Southern Calibrators Observed Using MeerKAT

A thesis submitted in fulfillment of the requirements for the degree of

Master of Science

By

ELIZABETH WANJIRU KAMAU

ORCID ID

https://orcid.org/0000-0001-9633-5398

Supervisors:

Prof. Oleg Smirnov

Dr. Nadeem Oozeer

December 18, 2025

Abstract

MeerKAT is a state-of-the-art radio telescope array in South Africa and a precursor to the revolutionary Square Kilometre Array (SKA). Given the critical role of calibration in ensuring that radio interferometers provide accurate scientific products, this thesis investigates the flux stability of a sample of 33 southern sky calibrators observed by MeerKAT. Our work builds upon a previous study of potential southern calibrators observed by the Karoo Array Telescope (KAT-7), a precursor to MeerKAT. The MeerKAT sample was first characterized by creating polynomial spectral models (which included archival data: 80 MHz - 4.8 GHz) using the SPECFIT package. We found that 26% of the calibrators had a peak, while 15% had a trough in their spectra, and 59% were fit with a linear power law. The flux variability analysis involved Long-Term Variability (LTV), corresponding to approximately a 2 year timescale, and Short-Term Variability (STV), corresponding to an order of hours timescale, with a threshold for potential variability set at variability metrics exceeding 3σ. Our LTV analysis across the three MeerKAT bands (U-, L-, and S- band) concluded that the majority of sources were stable below 1.283 GHz. However, PKS J0854+2006, a well-known blazar, exhibited variability at frequencies > 1.283 GHz. For the STV component, we performed a detailed statistical comparison on PKS J2152-2828, utilizing two distinct variability indices: VI_{Aller}, which provides a measure of the maximum fractional variation of the flux density and VI_{debias}, which takes into account the measurement uncertainties and is normalized by the mean flux. We specifically analysed two annular regions (within 0.5°, and between 0.5° - 1.2° from the phase center) to ensure any variability observed was intrinsic to the source. We concluded that PKS J2152-2828 exhibits no significant STV, confirming its reliability as a phase calibrator for similar duration observations.

Acknowledgements

Completing this thesis has been a challenging yet deeply rewarding journey, and I wish to express my heartfelt gratitude to those without whom this work would not have been possible.

First and foremost, I thank my supervisors, Prof. Oleg Smirnov and Dr. Nadeem Oozeer, for their invaluable academic guidance, unwavering support, and patience, particularly during the most challenging periods of this work. I also wish to thank Dr. Dharam Vir Lal for his thorough review, which prompted crucial revisions that led to a clearer and more in-depth final version.

I also want to extend my deep appreciation to my friends, Cyndi, Lexy, Lilian, Harriet, Shanice, and Maz, for their companionship, encouragement, and support throughout this program and beyond. I am particularly grateful to Sihle Gcilitshana for her patience in answering my never-ending questions as a newbie and the entire RATT team for their valuable insights.

I offer my deepest gratitude to my family for their love, care, and encouragement that have helped me pursue my dreams.

This work has only been realized because of the collective guidance and support of these individuals.
Thank you.

Declaration

I, Elizabeth Wanjiru Kamau, fully understand the meaning of plagiarism and hereby declare that all of the work in this document, unless stated otherwise through source acknowledgment, is my original research.

Contents

List of Figures

List of Tables

List of Abbreviations

avg of avg Average of Averages. 117–120, 123, 124, 127

CSS Compact Steep Spectrum. 47

EM Electromagnectic. 2, 14

GLEAM Galactic and Extragalactic All-sky MWA Survey. 29, 31

GMRT Giant Metrewave Radio Telescope. 11, 12

GPS Gigahertz-Peaked Spectrum. 47

IDV Intra-Day Variability. 17

IPS Interplanetary Scintillation. 16, 114, 130, 133

ISS Interstellar Scintillation. 16

LTV Long-Term Variability. iii, xii, xiv, xvii, 16, 26, 27, 61, 89, 92, 95, 97, 103, 109, 111, 114, 129, 131–133, 141, 142, 144, 146, 148

MCMC Markov Chain Monte Carlo. 44, 45

MFS Multi-frequency Synthesis. 80, 81

MRC Molonglo Radio Catalog Survey. 29, 31

NVSS NRAO VLA Sky Survey. 28, 29, 31, 92

PDF Probability Distribution Function. 44

PMN The Parkes-MIT-NRAO Survey. 28, 31

RACS The Rapid ASKAP Continuum Survey. 30

RFI Radio Frequency Interference. xvii, 62–66, 71, 84, 92

RIME Radio Interferometer Measurement Equation. 7–9

S-PASS S-band Polarisation All-Sky Survey. 30, 31

SEFD System Equivalent Flux Density. 10, 11

SKA Square Kilometre Array. iii, 9, 24

STV Short-Term Variability. iii, x, xvii, 17, 27, 61, 73, 81, 89, 93–95, 111, 114, 115, 117, 120, 126, 130, 132–134

SUMSS Sydney University Molonglo Sky Survey. 28, 31, 91, 92

U-band UHF-band. xiv, 9, 27, 60, 61, 63, 65, 69, 72, 74, 77, 79–81, 84, 85, 88–94, 114, 131, 141

VI Variability Index(s). 20, 23, 96, 97, 103, 111, 113–118, 120–123, 125, 126, 129, 132, 133

Chapter 1

An Introduction to Radio Astronomy, the MeerKAT Telescope, and Calibrators

Astronomy is the study of celestial objects beyond our atmosphere and has fascinated humans since the dawn of time. It has led to advances in timekeeping, optics, and mathematics. These advances have been driven by needs such as creating calendars for agricultural purposes, navigating across oceans, and developing advanced communication systems. Before 1931, astronomy was limited to optical observations, even though scientists were aware of the electromagnetic spectrum and that visible light was only a tiny portion of it (GAVRT, 1997). Radio astronomy is the study of natural radio emissions from celestial sources. Karl Guthe Jansky discovered natural radio emissions from our galaxy serendipitously in 1932 while working as a radio engineer at Bell Laboratories (Verschuur, 2007). Years later, Grote Reber, a radio engineer, expanded on Jansky's findings, building a prototype radio telescope in 1937 and publishing the first radio frequency sky maps in 1944 (GAVRT, 1997). After World War II, radio astronomy developed rapidly as a new field of research in astronomy, extending our cosmic horizons. In some sense, radio astronomy is the exploration of an invisible universe, a universe that can sometimes only be detected through its radio emission.

1.1 Radio Astronomy

Radio astronomy is the study of natural radio emissions from celestial sources. Radio waves are a type of electromagnetic (EM) wave. Electromagnetic waves are created by time-varying electric and magnetic fields with different parts of the electromagnetic spectrum characterised by frequency (ν) or wavelength (λ), where for monochromatic waves, $\lambda = c/\nu$, and c is the vacuum speed of light ($c \sim 3.0 \times 10^8\,\mathrm{m\,s^{-1}}$) (Marr et al., 2015). We are familiar with visible light, which our eyes can detect, but many objects emit radio waves that we cannot see with the naked eye. Radio waves are the longest waves on the Electromagnectic (EM) spectrum spanning hundreds of meters to $\approx 0.3\,\mathrm{mm}$, with a frequency range of $\sim 1\,\mathrm{THz}$[1] ($1\,\mathrm{THz} = 10^{12}\,\mathrm{Hz}$) to $\sim 10\,\mathrm{MHz}(30\,\mathrm{m})$ for ground-based radio astronomy (Condon and Ransom, 2016). Radio astronomers analyse and interpret radio waves detected by radio telescopes to study the physics of objects such as radio galaxies. Here are three main advantages of astronomy in the radio regime (Lockman, 2017):

- Some objects do not emit any visible light, but only emit low-energy radio waves. We would not know about such objects without radio astronomy. Examples are pulsars, very cold sources such as interstellar molecular clouds, and the cosmic microwave background from the Big Bang itself.

- Radio waves can travel through media that visible light cannot. Shorter wavelengths of light are easily blocked by the dusty interstellar medium, obscuring a host of different objects from our view, such as the galactic center. Radio waves can travel through these regions, revealing what lies beyond.

- The atmosphere of the Earth blocks a large portion of the electromagnetic spectrum from reaching the ground (see Figure 1.1). This makes ground observations almost impossible at shorter wavelengths. The atmosphere is almost transparent to radio waves; we can observe the sky day or night, in all weather, with radio telescopes on the ground.

[1] https://www.itu.int/dms_pubrec/itu-r/rec/ra/R-REC-RA.314-11-202312-I!!PDF-E.pdf

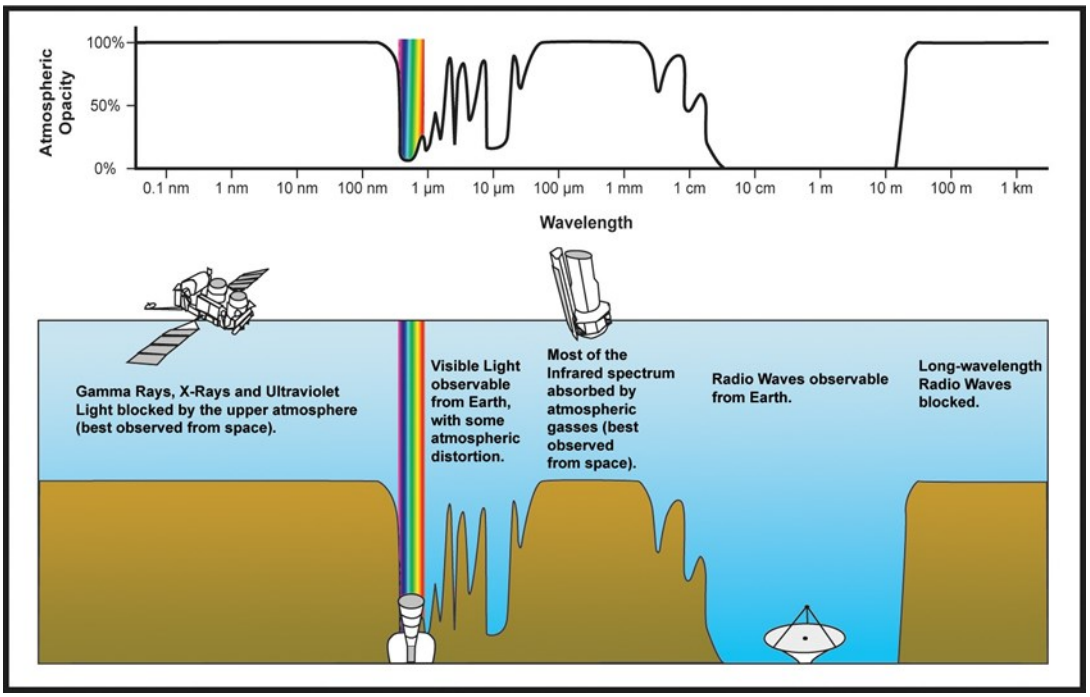

Figure 1.1: This figure shows the fraction of electromagnetic radiation absorbed by the Earth's atmosphere. Only optical/near-IR and radio observations can be conducted from the ground. The visible light window is relatively narrow and spans the wavelengths of peak thermal emission from black bodies ($\lambda \sim 0.4\,\mathrm{nm}$ to $0.7\,\mathrm{nm}$). The radio window is much wider and therefore includes a wide range of astronomical sources and emission mechanisms. Source: (ASSA).

1.1.1 Radio Telescopes

Radio telescopes are designed to detect radio waves that make their way through the atmosphere to us. Most radio telescope antennas are parabolic (dish-shaped) reflectors that gather radio waves and reflect them to a central focus where the radiation is concentrated (GAVRT, 1997). A radio receiver can then amplify the weak signal at the focus, making it strong enough to measure and record. Radio astronomers measure the intensity of radio waves as the power (in Watts) that passes through an aperture of $1\,\mathrm{m}^2$ in $1\,\mathrm{s}$ in a bandwidth of $1\,\mathrm{Hz}$ (Lockman, 2017). The intensity of radio waves is measured in units called Janskys, after Karl G. Jansky:

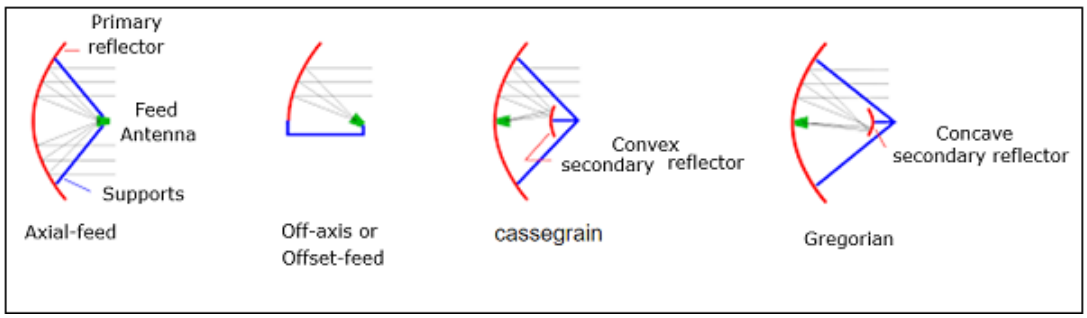

Figure 1.2: The different feed types that are commonly used for parabolic dishes. Source: Google Images

$$1\,\text{Jansky}\,(\text{Jy}) = 10^{-26}\,\text{Wm}^{-2}\text{Hz}^{-1} \tag{1.1}$$

The feed houses the receiver (and amplifier) where the focused radio waves arrive from the reflector. There are a variety of feed configurations as illustrated in Figure 1.2 when using the parabolic dish antenna:

- **Axial/Front Feed** This is the most common feed type, with the feed located at the prime focus in front of the reflector.
- **Off-axis Feed** The reflector is designed such that the focus is located on one side of the dish. This is where the feed is placed. This design has an advantage over the front feed system as the feed and its support do not block radio waves arriving at the reflector.
- **Cassegrain Feed** A primary reflector collects the radio waves and directs them to the focal point. At the focal point is an additional secondary reflector that directs focused radio waves to the feed. This design has a high aperture efficiency. The secondary reflector is convex in shape.
- **Gregorian Feed** This design is similar to the Cassegrain design, which features a secondary reflector in addition to the primary reflector. In this case, the secondary reflector is concave in shape.

An important characterization of telescopes is their angular resolution, θ_{res}. Assuming a circular aperture of size D and a wavelength of EM radiation λ (Marr et al., 2015):

Instrument	λ m	**D** m	θ $''$
Human Eye	5×10^{-7}	0.003	41.9
Hubble Space Telescope	5×10^{-7}	2.4	0.05
Arecibo Radio Telescope	0.3	200	378
Five-hundred-meter Aperture Spherical Telescope (FAST)	0.3	500	151

Table 1.1: A table of apertures and their resolutions at visible and radio wavelengths.

$$\theta_{\text{res}} \approx 1.22\frac{\lambda}{D} \tag{1.2}$$

The resolution determines the amount of detail that can be discerned when observing an object. Table 1.1 illustrates the different angular resolutions achieved by different apertures at visible and radio wavelengths. For example, if one observes in the visible wavelength at $0.5\,\mu$m (micrometers) with an aperture of 3 mm ($\approx$ human pupil), the resolution would be $41.9''$. This is enough to resolve a few details on the moon as observed by the naked eye. On the other hand, if the Hubble Space Telescope were observing at the same wavelength with its 2.4 m aperture, it would achieve a $0.05''$ resolution - a thousand times more powerful than the human eye. The Arecibo Radio Telescope and the Five-hundred-meter Aperture Spherical Telescope (FAST), observing at 1 GHz $(0.3\,\text{m})$ radio wavelengths, have poorer resolution even though they have bigger apertures.

1.1.2 Interferometry

It is clear from Equation 1.2 that longer wavelengths would require large apertures to achieve high resolution. Building substantially large apertures to achieve higher resolutions would be too costly and also not feasible from an engineering perspective. Therefore, radio astronomers adopted the use of a technique called interferometry to achieve high resolutions. The interferometric technique was developed from the Michelson stellar interferometer. It involves the use of multiple single-dish antennas to observe the same source simultaneously. The signals are then combined, with the multiple antennas effectively acting as small pieces

of a single large telescope (Thompson et al., 2001). In this scenario, the angular resolution previously given by Equation (1.2) becomes:

$$\theta_{\text{res}} \sim \lambda / B_{\text{max}} \tag{1.3}$$

where B_{max} is the maximum distance between two telescopes, referred to as the baseline. Astronomical objects such as galaxies emit radiation from multiple independently radiating entities. Such natural processes are random in that the properties of signals are inferred from their statistical manifestation (Kassaye, 2015). An antenna observing such a source will have voltages, commonly referred to as signals, induced by the incoming radiation. A signal in the observer plane is generally represented by the electric field $\mathbf{e}$, and when it arrives at two antennas at the positions $\mathbf{r_1}$ and $\mathbf{r_2}$, the result is defined by the spatial correlation function:

$$V(\mathbf{r_1}, \mathbf{r_2}) = \langle \mathbf{e}(\mathbf{r_1}) \cdot \mathbf{e}^*(\mathbf{r_2}) \rangle \tag{1.4}$$

The angled brackets in Equation 1.4 represent averaging over time, and the asterisk denotes a complex conjugate. $V(\mathbf{r_1}, \mathbf{r_2})$ is referred to as the visibility (fringe visibility function), a fundamental function in interferometry. The visibility function is a Fourier transform ($\mathfrak{F}$) of the intensity distribution of a source (the image). This basic principle originated in optics in the 1930s and was formulated by Van Cittert followed by a more straightforward derivation by Zernike (Thompson et al., 2001). The visibility $\mathrm{V}(u,v,w)$ of a distant spatially incoherent source as measured by an interferometer can be related to the spectral intensity $\mathrm{I}(l,m)$ of the source as follows:

$$\mathrm{V}(u,v,w) = \int\int_s \mathrm{I}(l,m) \frac{\exp\left(-2\pi j[ul+vm+wn]\right) dldm}{\sqrt{1-l^2-m^2}} \tag{1.5}$$

Where (u,v,w) are the baseline in the observer's plane, j is the imaginary unit satisfying the equation $j^2 = -1$ and (l,m) are the direction cosines in the sky. When $w = 0$, the above equation is reduced to:

$$\mathrm{V}(u,v) = \int\int_s \mathrm{I}(l,m) \frac{\exp(-2\pi j[ul+vm]) dldm}{\sqrt{1-l^2-m^2}} \tag{1.6}$$

From the above equation, we can see that the visibility $\mathrm{V}(u,v)$ is the Fourier transform of the intensity distribution $\mathrm{I}(l,m)$ modified by $(\sqrt{1-l^2-m^2})$. Since the intensity distribution is restricted to a small region of the sky, we can simplify: $\sqrt{1-l^2-m^2} \sim 1$. We can then extract the Fourier transform relation where $\mathrm{I}(l,m)$ (the sky brightness) can be obtained from an inverse Fourier transform of the visibility function $\mathrm{V}(u,v)$.

$$\mathrm{V}(u,v) = \int\int_s \mathrm{I}(l,m)\, \exp(-2\pi j[ul+vm])\, dldm \tag{1.7}$$

1.1.3 Radio Interferometer Measurement Equation (RIME)

As discussed in the previous section, for each pair of antennae in an interferometer, we measure a visibility function. The visibilities we measure are not a perfect representation of the sky, since the signal is distorted as it travels from the source to an antenna. A Fourier transform of such a visibility function usually produces a distorted intensity distribution (image). Calibration is the process of correcting measured visibilities for instrumental and atmospheric effects. Technically, calibration consists of using a sky model formed from our existing knowledge of the observed field to fit the measured data in a well-defined mathematical framework (Sob, 2017). An example of such a framework is the Radio Interferometer Measurement Equation (RIME).

The measurement equation (RIME) is a set of equations for visibility values measured for a given source, the effects along the signal path, the characteristics of the individual antenna, and any other effects that may influence a signal (Thompson et al., 2001). The formulation of these equations began with the analysis by Hamaker et al. (1996) and was further developed by Smirnov (2011) and others (Thompson et al., 2001). The distortion caused by effects extrinsic to the source can be corrected by using RIME.

A simple form of RIME is its 2×2 matrix, also known as the Jones formalism. An electromagnetic plane wave can be described by a 2-column vector of its electric field components in the x and y directions: $\mathbf{e} = \begin{pmatrix} e_x \\ e_y \end{pmatrix}$. The RIME leverages this two-column vector representation of the EM wave to provide accurate visibility calculations. For any specified

intensity distribution and specific interferometer, the RIME provides accurate values of the visibility to be observed (Smirnov, 2011). Consider a signal that arrives at two antennas (p and q) and is converted into complex voltages with a linear relationship to the electric field **e**. In the Jones formalism, the RIME of a point source gives the visibility matrix $\mathrm{V}_{p,q}$ as a product of the intrinsic source brightness matrix B and per-antenna Jones matrices J_p, J_p (Smirnov, 2011):

$$\mathrm{V}_{p,q} = J_p \mathrm{B} J_q^H \tag{1.8}$$

The Jones matrices describe the total signal paths to antennas p and q, respectively. They each have individual propagation effects represented by a Jones chain

$$J_p = J_{p,n} J_{p,n-1} \ldots\ldots J_p, \tag{1.9}$$

Which leads to the 'onion' form of the RIME:

$$\mathrm{V}_{p,q} = J_{p,n}(\ldots(J_{p,2}(J_{p,1}\mathrm{B}J_{q,1}^H)J_{q,2}^H)\ldots)J_{q,m}^H \tag{1.10}$$

In practice, the RIME requires a set of matrices: each describing specific effects which are then input in the equation above. These matrices tend to have single-letter designations, for example, the term K_p describes the geometric phase delay to the antenna p and is given by :

$$K_p = \exp(-2\pi j(u_p l + v_p m + w_p(n-1))) \tag{1.11}$$

Using this format, the onion form of the RIME can be split into Direction Independent Effects (DIEs) denoted by G_p and Direction Dependent Effects (DDEs) denoted by E_p. DIEs affect the signal from all directions equally, while DDEs vary depending on the sky position of the signal. The RIME for multiple discrete sources, such as that of an extended source, can then be written as:

$$\mathrm{V}_{p,q} = G_p(\sum_s E_{s,p} K_{s,p} \mathrm{B} K_{s,q}^H E_{s,q}^H) G_q^H \tag{1.12}$$

Substituting the term $K_p K_q^H$ into the equation, we get the Fourier transform kernel in the full sky RIME where all matrix terms under the integration sign are functions of the direction cosines (l,m):

$$\mathrm{V}_{p,q} = G_p\left(\int\int_{l,m} E_p \mathrm{B} E_q^H e^{(-2\pi j(u_{p,q}l+v_{p,q}m))} dldm\right) G_q^H \tag{1.13}$$

Therefore, the primary goal of calibration is to solve for the unknown terms in the G_p and E_p matrices. These solutions are achieved through the observation of calibrator sources, whose intrinsic brightness (B) and positions are well known, thereby isolating and allowing measurement of the system's gain errors.

1.2 MeerKAT: Technical Specifications

MeerKAT is an interferometer located in the Karoo region of the Northern Cape Province in South Africa that is set to be integrated into the mid-frequency component of SKA Phase 1. The MeerKAT array comprises 64, 13.5 m diameter antennas. The antennas have an offset Gregorian design chosen for the efficient collection of radio waves as discussed in Section 1.1.1. The array has a 'core heavy' configuration, with a dense inner core containing 70% of the antennas. The minimum baseline is 29 m and the maximum baseline is 7.7 km (Jonas and MeerKAT Team, 2016). MeerKAT antennas are equipped with S-band, L-band, and U-band receivers. These provide good frequency coverage for carrying out multi-frequency observations of radio sources. These specifications are summarized in Table 1.2.

With a variety of baseline combinations and frequency ranges, MeerKAT can observe a host of radio sources of various angular sizes. As discussed in Section 1.1.1, different angular resolutions provide different capabilities to observers, viz., the capability to observe celestial sources with large angular sizes or to resolve their finer details. To capture diffuse and extended emission, the short baselines are critical, while the longest baselines are useful in capturing point/compact sources. Table 1.3 summarizes the three frequency bands and their corresponding angular resolutions.

Additionally, the sensitivity of a radio telescope is an important specification that deter-

Number of antennas	64 (offset Gregorian)
Dish diameter	13.5 m
Minimum baseline	29 m
Maximum baseline	7700 m
Array phase center	30°42′39.8″South, 21°26′38.0″ East, 1086.6 m Elevation

Table 1.2: MeerKAT Specifications Summary Table. Source: (SARAO)

Band	Frequency range [MHz]	Central Frequency [MHz]	θ_{min} [′]	θ_{max} [″]
UHF-band (U-band)	580 - 1015	856	50.7	11.4
L-band	900 - 1670	1347	32.2	7.3
S-band	S0: 1750 - 2625 S1: 1968 - 2843 S2: 2187 - 3062 S3: 2406 - 3281 S4: 2625 - 3500	2919	14.9	3.4

Table 1.3: Achievable angular resolutions per MeerKAT band's central frequency using the minimum and maximum baseline provided in Table 1.2. Source: (SARAO)

mines the depth and detail of the sky that the telescope can observe. Sensitivity is influenced by system temperature (T_{sys}) and System Equivalent Flux Density (SEFD). T_{sky} represents the combined temperature contributions of elements along the signal path as seen in Equation 1.14 (Thompson et al., 2017).

$$T_{\text{sys}} = T_{\text{sky}}(RA, Dec, \nu) + T_{\text{spill}}(El, \nu) + T_{\text{atm}}(El, \nu) + T_{\text{rec}} \tag{1.14}$$

where

- T_{sys} represents the temperature of the sky that varies according to the Right Ascension

(*RA*), the Declination (*Dec*), and the frequency (ν).

- T_{spill} represents the spillover temperature that occurs when some of the signals intended for one receiver leak into another. This parameter depends on the elevation angle (el) and frequency (ν).
- T_{atm} represents atmospheric temperature dependent on elevation angle (el) and frequency (ν).
- T_{rec} represents the constant contributions of system components such as the receiver, the correlator, and the antenna.

The theoretical noise S_{rms} of an interferometer with N antennas is given by equation 1.15:

$$S_{\text{rms}} = \frac{2\text{k}T_{\text{sys}}}{A_e \eta_Q \sqrt{2N(N-1)\Delta\nu t_{\text{int}}}} \tag{1.15}$$

where k is Boltzmann's constant, T_{sys} is the system temperature, A_e is the effective collecting area of an antenna, η_Q is quantisation efficiency, $\Delta\nu$ is the bandwidth in Hz, t_{int} is the integration time in seconds, and (N) is the number of antennas (Thompson et al., 2001). Equation 1.15 can be simplified to:

$$S_{\text{rms}} = \frac{\text{SEFD}}{\sqrt{2N(N-1)\Delta\nu t_{\text{int}}}} \tag{1.16}$$

The SEFD is the flux density equivalent to the system temperature T_{sys}. The SEFD helps quantify the sensitivity of a radio telescope, that is, the weakest radio emission that can be detected.

From equations 1.15 and 1.16, we can deduce that the sensitivity of a radio telescope can be improved by increasing the integration time (t_{int}), increasing the number of antennas (N), expanding the bandwidth ($\Delta\nu$), and lowering the system temperature.

Take, for example, the sensitivity of a 2 hour observation in the L-band, with an average SEFD of 460 Jy (Camilo et al., 2018) for MeerKAT and an equivalent 2 hour observation with an SEFD of $\approx$ 250 Jy at 100 MHz for the Giant Metrewave Radio Telescope (GMRT) (with 30 antennas) (Lal, 2015):

$$S_{\text{rms}}(\text{MeerKAT}) = \frac{460\,\text{Jy}}{\sqrt{2 \times 64(64-1) \times (856 \times 10^6\,\text{Hz}) \times 7200\,\text{s}}} = 2.06\,\mu\text{Jy}$$

$$S_{\text{rms}}(\text{GMRT}) = \frac{250\,\text{Jy}}{\sqrt{2 \times 30(30-1) \times (100 \times 10^6\,\text{Hz}) \times 7200\,\text{s}}} = 7.06\,\mu\text{Jy}$$

This comparison highlights the higher sensitivity of MeerKAT, which enables the detection of faint radio emissions from astronomical phenomena that might be undetectable with less sensitive arrays.

1.3 Calibrators

A calibrator is a radio source whose parameters, such as flux density, position, and spectral properties, are well known (Thompson et al., 2001). They serve as essential references to calibrate the observed data. As discussed in Section 1.1.3, calibration deals with errors resulting from instrumental and atmospheric variables. The former stems from the electronic devices that make up the system and antenna malfunctioning, while the latter originates from interactions of the signal with the intervening medium along the signal path.

The net correction factors are usually determined by observing these known sources and transferring their parameters to the observed data. This process relies on two main types of calibrators (Thompson et al., 2001):

- **Primary Calibrators**

  These are typically bright radio sources whose flux density is well known and are used to determine the absolute flux density scale of the array, converting raw instrumental units to Janskys (flux calibrators). They are also often used to determine the receiver's frequency response (bandpass calibrators).

- **Secondary Calibrators**

  Ground-based telescopes primarily measure phase differences. Therefore, observations of compact, point-like sources are essential in establishing an absolute phase

reference. These sources are observed frequently over the observation period to track and correct for time-variable atmospheric phase and time-variable instrumental gain changes (phase/gain calibrators).

Calibrator sources are selected based on the following desirable properties (Thompson et al., 2001):

- A sufficiently strong source to ensure a good signal-to-noise (SNR) ratio.
- An isolated source in the target region with no other strong, confusing radio sources within the primary beam of the telescope.
- A compact, unresolved point source.
- A source with non-variable characteristics during the period of observation.
- A source with a known position in the sky, preferably, close to the science target.

While suitable calibrators are radio sources defined by the above criteria, in practice, this means that they would be powered by Active Galactic Nuclei (AGN) as these sources meet the brightness and compactness criteria. Radio emission from radio-loud AGN, predominantly produced via non-thermal processes, varies on the timescales of years to less than a day in all frequency bands of the EM spectrum (Wagner and Witzel, 1995). This makes the issue of calibrator variability important, as changes in their properties would directly impact the veracity of the calibration process and subsequent scientific products if not properly accounted for.

1.4 Active Galactic Nucleus (AGN)

The radiation from most galaxies is the sum of the emission from the different components of the galaxy, such as stars and gas. In contrast, galaxies with an active nucleus emit substantially larger amounts of radiation, up to a thousand times more, originating from a localized region at the center of the galaxy referred to as the Active Galactic Nucleus (AGN) (Sparke

and Gallagher, 2010). A defining characteristic of AGN is a rapid change in luminosity, which can occur over short timescales such as days or even hours. Such rapid variability implies that the emitting region must be incredibly compact, typically no more than a few light-weeks across, due to the finite speed of light (Sparke and Gallagher, 2010). The radiation from AGN is emitted strongly over the whole electromagnetic spectrum: in the X-ray, γ-ray, and radio regions, where most galaxies hardly radiate at all (Sparke and Gallagher, 2010).

The currently accepted model for the mechanism that powers AGN is an accreting Super Massive Black Hole (SMBH) (Lockman, 2017). SMBHs are gravitationally powerful enough to attract and consume surrounding gas and dust in a galaxy. This infalling matter typically forms a rapidly rotating disk of material threaded with strong magnetic fields called an accretion disk. From the nucleus, powerful jets of relativistic particles are launched, extending along magnetic fields perpendicular to the accretion disk. Within these jets, particles spiral around the magnetic field lines, generating synchrotron radiation that is detected at radio wavelengths and forms the observed radio jets in some AGN (Lockman, 2017). A remarkable feature of these jets is their ability to travel immense distances without substantial energy loss, resulting in a considerable release of energy when they finally encounter resistance (Lockman, 2017). The interaction of the jets of magnetic fields and relativistic particles with the intergalactic medium forms the large radio lobes observed in radio images. Figure 1.3 illustrates the different classes of AGN, such as radio galaxies, which are characterised by a large amount of non-thermal emission peaking at radio wavelengths.

1.4.1 AGN Variability

As discussed in Section 1.3, calibrators are radio sources that should ideally be non-variable. However, they also have AGN. Emissions from radio-loud AGN predominantly produced via non-thermal processes vary on timescales of years to less than a day in all frequency bands of the EM spectrum (Wagner and Witzel, 1995). Various monitoring programs across the EM spectrum have been implemented to probe these objects. These programs have provided critical information on the mechanisms driving these sources and have offered significant

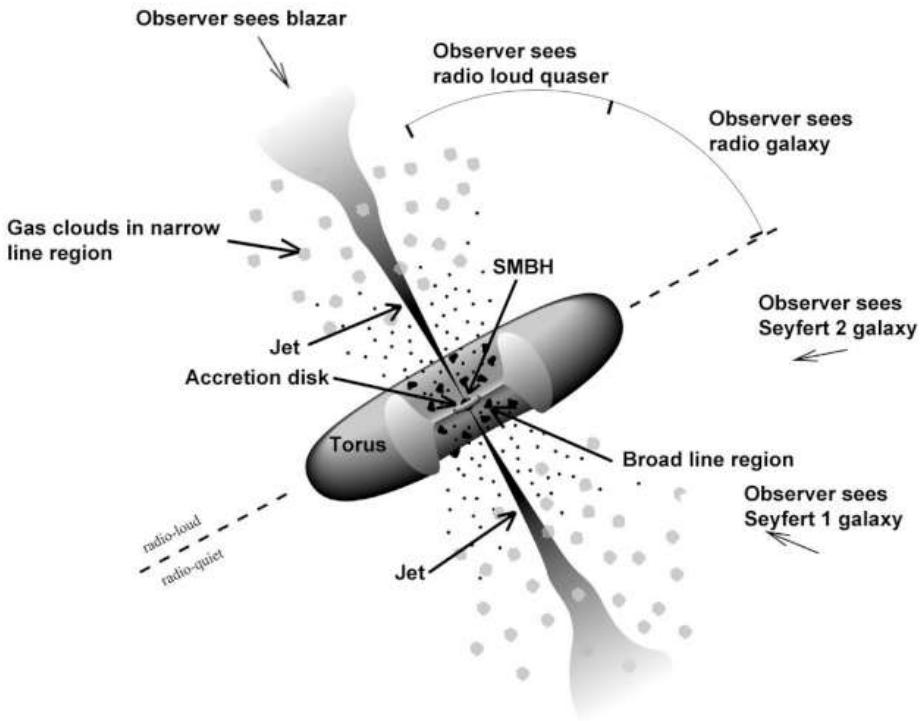

Figure 1.3: Illustration of AGN classes based on the observer's viewing angle. Source: Google Images

implications for quasar modeling (Fan et al., 2007). In the radio regime, the variability of these sources has been attributed to various mechanisms such as shocks in jets, changes in the direction of forward beaming, and precession in a binary black-hole system, as discussed by Fan et al. (2007). Radio source variability has served as a powerful probe in the study of extragalactic source structure and the physics of the environmental interactions of radio galaxies (Ross et al., 2020).

Intrinsic variability is a type of variability whose origin arises from the dynamics of the source itself. This variability gives researchers a crucial observational window into key physical processes such as changes in the accretion state and jet evolution of a source (Ross et al., 2020), as well as insight into photon populations in the localized emitting regions (Wagner and Witzel, 1995).

Extrinsic variability arises from the interaction of the sources' radiation with the intervening media along the line of sight. The density inhomogeneities of electrons in the interstellar medium (ISM) on different spatial scales introduce temporal fluctuations in the flux

density registered by an observer. These temporal fluctuations are referred to as Interstellar Scintillation (ISS) (Wagner and Witzel, 1995). ISS is frequency-dependent and dominant at radio frequencies up to 10 GHz, with any source with a high degree of compactness bound to scintillate (Roland et al., 2009). Depending on the frequency of the radiation, ISS typically varies the brightness of the source on time scales of months to years (Ross et al., 2020). ISS has two subcategories (Ross et al., 2020):

- Refractive - which produces long (months to years) timescale variability.
- Diffractive - which produces short (days to weeks) timescale variability.

Another cause of extrinsic variability is Interplanetary Scintillation (IPS), which occurs when radio waves are distorted as they travel through the solar wind (Ross et al., 2020). IPS typically manifests on very short timescales (a few seconds) and primarily affects compact sources with small angular sizes, especially at frequencies below a few GHz (Morgan et al., 2017; Thompson et al., 2001).

Before exploring intrinsic variability as an explanation for observed rapid variations, extrinsic causes must be investigated. Simultaneous multi-frequency spectral coverage can be used to distinguish between intrinsic or extrinsic processes as the cause of variability (Ross et al., 2020). Variability can be categorized according to the timescales in which it occurs:

- **Long-Term Variability (LTV)**
  Long-Term Variability (LTV) can have time scales of several years (Gupta et al., 2004). Studies on LTV are valuable, as they can inform future outburst predictions and provide information on the dynamic nature of these sources. For example:

  1. Utilizing data from the University of Michigan Radio Astronomy Observatory (UMRAO), in three radio frequency bands (4.8 GHz, 8.0 GHz, and 14.5 GHz), Fan et al. (2007) investigated potential periodicity in radio-light curves. The analysis revealed significant astrophysical periodicities with periods ranging from 2.2 to 20.8 years across the three frequencies.

2. Perley and Butler (2013) carried out a 40-year monitoring of standard radio flux density calibrators over a range of radio frequencies. They found that the radio sources; 3C123, 3C196, 3C286, and 3C295 vary at a level of less than ∼5% per century at all frequencies between 1 and 50 GHz.

- **Short-Term Variability (STV)**

  Short-Term Variability (STV) occurs on the time scales of weeks to months (Gupta et al., 2004). Intra-Day Variability (IDV) describes rapid flux density variations in the radio regime that occur on timescales of a day to a few hours or even minutes (Roland et al., 2009). We will group IDV as STV for our discussion. Rapid variations such as those of IDV and STV tightly constrain the emitting radius of the emitting region to $r < c \times \lambda t$, with a light travel time (λt) corresponding to the timescale of variations discussed by Wagner and Witzel (1995). This provides information on source structures existing on linear scales smaller than the solar system. The origin of all types of variability has been attributed to both source intrinsic and extrinsic mechanisms (Roland et al., 2009).

1.5 Literature Review

Kassaye (2015) investigated the suitability of a sample of sources as potential flux density calibrators for the Karoo Array Telescope (KAT-7, Foley et al. (2016)), a precursor to MeerKAT. The analysis (based on a sample of 38 potential calibrators) focused on source variability as a determining parameter, a crucial factor in the calibration process. Two main metrics were employed to assess variability:

1. **Variability Index (VI)**

$$\mathrm{VI} = \frac{S_{\max} - S_{\min}}{S_{\max} + S_{\min}} \tag{1.17}$$

Where $S_{\max}$ and $S_{\min}$ represent the maximum and minimum flux densities of a source in the entire observation, respectively. The VI provides a measure of the maximum

fractional variation of the flux density of a source. However, it has limitations. It relies on only two data points and can be sensitive to outliers, potentially overlooking relevant variability patterns.

2. **Modulation Index (MI)**:

$$\mathrm{MI} = \frac{\sigma}{\langle S \rangle} \tag{1.18}$$

Where $\langle S \rangle$ is the mean flux density of a source and σ is the standard deviation - the spread of the flux density in each source about the mean $\langle S \rangle$. The MI offers a more comprehensive assessment by quantifying the fractional variation of the peak flux density relative to the mean. Since it utilizes all available flux density measurements, MI provides a stronger indication of variability strength.

Based on these metrics, Kassaye (2015) proposed a classification scheme to identify potential calibrators:

- Class A (Good Candidate): Sources with both MI and VI values between 0 and 0.05 and no confusing sources (all the sources in the field had less than 10% of the peak flux density of the calibrator candidate). These sources had a high likelihood of being suitable calibrators due to their minimal variability. 18 sources (47% of the sample) fell into this class.

- Class B and C (Require further study): Sources with either MI or VI values between 0.05 and 0.09 required further investigation to determine their suitability as flux calibrator candidates. Additionally, sources with limited data (only two observations) or insufficient information available in the literature could not be analysed definitively, requiring further study. 16 sources (42% of the sample) fell into this class.

- Class D (Bad Candidate): Sources with either MI or VI values exceeding 0.09 were classified as bad calibrator candidates due to their potentially high variability, with previous studies of these sources supporting the conclusion that these sources are significantly variable. 5 sources (13% of the sample) fell into this class.

The flux variability of the sources was studied at a single frequency (1.83 GHz), and no polarization characteristics were considered. It was noted that these were important factors that would need to be studied in order to fully declare the suitability of the calibrators.

These indices (VI and MI) provide quantitative and normalized metrics for variability, allowing for objective and reliable identification of sources whose flux densities remain sufficiently stable for calibration purposes.

Oozeer et al. (2015) undertook a study to investigate the short-term radio variability (10-30 days) of PKS 1510-089 (a blazar at a redshift $z = 0.361$) using KAT-7 at 1822 MHz. Their observations began in October 2011 and continued for over two years as part of the telescope's science commissioning phase. The study used several statistical metrics.

The variability index used is given by:

$$V_{\text{rms}} = \frac{100}{\langle S \rangle} \sqrt{\frac{\Sigma[S_i - \langle S \rangle]^2 - \Sigma \Delta S_i^2}{N}} \tag{1.19}$$

where S_i are the flux density measurements and ΔS_i the uncertainty in the measurement. The Modulation Index (MI) was used to provide a measure of the strength of observed variability of a source without taking into account the error of the individual measurement:

$$\text{MI} = 100 \times \frac{2\sigma_I}{\langle S \rangle} \tag{1.20}$$

where σ_I is the standard deviation of a source's observed flux density from the mean flux density $\langle S \rangle$ raised by a factor of two and expressed as a percentage (Oozeer et al., 2015). They also calculated the Amplitude Variability (Y), which is given by:

$$\text{Y} = 3\sqrt{\text{MI}^2 - \text{MI}_0^2} \tag{1.21}$$

Here, MI_0^2 is the modulation index of a non-variable source, the calibrators 3C286 or PKS 1934-638 in this case (Oozeer et al., 2015). Subtracting MI_0^2 from the observed MI of a source effectively accounts for a baseline noise variability, allowing the Y value to quantify the source's intrinsic variability. Oozeer et al. (2015) concluded that PKS 1510-089 exhibits significant variability due to a modulation index of $\approx 16\%$ and a Y factor of 46%.

The variability metrics presented by Kassaye (2015) and Oozeer et al. (2015) formed the basis for the metrics used in our variability analysis, as detailed in the next section.

1.5.1 Variability Metrics

To sufficiently capture all aspects of variability while taking into account noise and systematic errors, we used a set of different variability metrics. All calculated uncertainties (Δ) for the variability metrics were derived using the method of propagation of errors (also known as propagation of uncertainty) (Taylor, 1997).

1. **Variability Index**

   The Variability Index(s) (VI) introduced by Aller et al. (1999) that we will refer to as $\mathrm{VI}_{\mathrm{Aller}}$, is defined as:

$$\mathrm{VI}_{\mathrm{Aller}} = \frac{S_{\mathrm{max}} - S_{\mathrm{min}}}{S_{\mathrm{max}} + S_{\mathrm{min}}} \tag{1.22}$$

   where S_{max} and S_{min} represent the maximum and minimum fluxes in one scan, respectively.

$$\Delta\mathrm{VI}_{\mathrm{Aller}} = \left(\frac{\sigma_{S_{\mathrm{max}}} + \sigma_{S_{\mathrm{min}}}}{S_{\mathrm{max}} - S_{\mathrm{min}}} + \frac{\sigma_{S_{\mathrm{max}}} + \sigma_{S_{\mathrm{min}}}}{S_{\mathrm{max}} + S_{\mathrm{min}}} \right) \times \mathrm{VI}_{\mathrm{Aller}} \tag{1.23}$$

   The error $\Delta\mathrm{VI}_{\mathrm{Aller}}$ is calculated as in Equation 1.23, where σ_{max} and σ_{min} are the corresponding errors in the maximum (S_{max}) and minimum flux (S_{min}). Crucially, $\mathrm{VI}_{\mathrm{Aller}}$ provides a measure of the maximum observed fractional variation. However, this quantity is sensitive to outliers because it uses only two points per sample.

   Fan et al. (2007) introduced another VI, originally implemented by Aller et al. (1999). We refer to it as $\mathrm{VI}_{\mathrm{Fan}}$, defined as:

$$\mathrm{VI}_{\mathrm{Fan}} = \frac{(S_{max} - \sigma_{S_{max}}) - (S_{min} + \sigma_{S_{min}})}{(S_{max} - \sigma_{S_{max}}) + (S_{min} + \sigma_{S_{min}})} \tag{1.24}$$

where $S_{\max}$ and $S_{\min}$ are the peak and minimum flux densities, and $\sigma_{S_{\max}}$ and $\sigma_{S_{\min}}$ are the associated measurement errors of the fluxes. The uncertainties in $\mathrm{VI}_{\mathrm{Fan}}$ are calculated as:

$$\sigma_{\mathrm{VI}_{\mathrm{Fan}}} = \sqrt{\left(\frac{4S_{\min}\,\sigma_{S_{\max}}}{D^2}\right)^2 + \left(\frac{4S_{\max}\,\sigma_{S_{\min}}}{D^2}\right)^2}, \quad \text{with} \quad D = S_{\max} + S_{\min} - \sigma_{S_{\max}} + \sigma_{S_{\min}}. \tag{1.25}$$

The result of equation 1.24 is a value that indicates the relative extent of variability in the light curve while factoring in uncertainties. The numerator gives the difference between the adjusted peak flux (subtracting its error) and the adjusted minimum flux (adding its error) to show the true range of variability. The denominator gives the sum of the adjusted peak flux and the adjusted minimum flux, normalising the variability range. Subtracting from the peak and adding to the trough provides a conservative, realistic estimate of variability by accounting for measurement errors, thus reflecting a conservative range of variability as opposed to adding to the peak and subtracting from the trough, which would inflate the variability index and potentially misrepresent the true variability due to measurement errors. Though $\mathrm{VI}_{\mathrm{Fan}}$ is sensitive to outliers, it is quite useful in analysing cases of sudden bursts or flaring.

2. **Normalized Variability Amplitude (NVA)**

The normalized variability amplitude (NVA) is calculated as (Fan et al., 2007):

$$\mathrm{NVA} = \frac{\sqrt{\sigma_{\mathrm{tot}}^2 - \sigma_{\mathrm{err}}^2}}{\langle X \rangle} \tag{1.26}$$

where $\langle X \rangle$ is the average flux, σ_{tot}^2 is the total standard deviation of the flux points, and σ_{err}^2 is the mean error level in the flux measurements per band. The NVA (Equation 1.26) indicates how much the flux varies relative to its mean, independent of instrumental effects. The uncertainty is calculated as:

$$(\Delta\mathrm{NVA})^2 = \frac{1}{4\,\mathrm{NVA}^2\,\langle S \rangle^4}\left[\left(\sigma_{\mathrm{tot}}^2 - \sigma_{\mathrm{err}}^2\right)^2 \left(\frac{\Delta\langle S \rangle}{\langle S \rangle}\right)^2 + \langle S \rangle^2\,\Delta(\sigma_{\mathrm{tot}}^2) + \langle S \rangle^2\,\Delta(\sigma_{\mathrm{err}}^2)\right], \tag{1.27}$$

$$\Delta\text{NVA} = \sqrt{(\Delta\text{NVA})^2}. \tag{1.28}$$

3. **The Root Mean Square Dispersion (RMSD)**

Although variability metrics are constructed to account for the effect of measurement uncertainties as in Equation 1.24, the quantity is only well defined when the variability is significantly greater than the measurement errors. It can yield negative values for sources with low SNR or little intrinsic variability. To determine if the observed variability is real or not when a source has been observed at several epochs, one can compare the distribution of flux at the different epochs with a model in which the flux of the source is assumed to be non-variable. The Root Mean Square Dispersion (RMSD), (Fan et al., 2007), allows us to perform this check and is defined as:

$$\text{RMSD} = \frac{1}{\langle S \rangle}\sqrt{\frac{1}{N-1}\sum_{i=1}^{N}(S_i - \langle S \rangle)^2} \tag{1.29}$$

In Equation 1.29, $\langle S \rangle$ is the mean, while S_i represents the measured fluxes. This equation gives the spread of the flux measurements around the mean flux, relative to the mean flux, indicating the relative variability. The uncertainty in the mean (μ) is given by:

$$\Delta\mu = \frac{\sqrt{\sum_{i=1}^{N}\sigma_i^2}}{N}, \tag{1.30}$$

where σ_i are the flux density errors, and the uncertainty in the variance term is given by:

$$\Delta\left(\sum(S_i - \langle S \rangle)^2\right) = \sqrt{\sum_{i=1}^{N} 4\,(S_i - \langle S \rangle)^2\,\sigma_i^2}, \tag{1.31}$$

Finally, the uncertainty in RMSD is given by:

$$\Delta\text{RMSD} = \sigma_{\text{RMSD}}\sqrt{\left(\frac{\Delta\mu}{\langle S \rangle}\right)^2 + \frac{1}{4}\left(\frac{\Delta(\sum(S_i - \langle S \rangle)^2)}{\sum(S_i - \langle S \rangle)^2}\right)^2 + \left(\frac{\Delta\mu}{\langle S \rangle}\right)^2}. \tag{1.32}$$

The χ^2 value from Equation 1.33 compares the observed flux distribution to a model where the source is non-variable (Kembhavi and Narlikar, 1999). A χ^2 value greater than 1 suggests variability beyond random noise.

$$\chi^2 = \frac{1}{N}\sum_{i=1}^{N}\left(\frac{S_i - \langle S\rangle}{\sigma_i}\right)^2 \tag{1.33}$$

4. **Debiased Variability Index**

The debiased VI, $(\mathrm{VI}_{\mathrm{debias}})$ as given by Barvainis et al. (2005), quantifies the intrinsic variability of the source, corrected for N measurement uncertainties and normalized by the mean flux. In the following equations, S_i are the fluxes, σ_i their measurement errors, μ is the sample mean of S_i, and std(S) is the sample standard deviation.

$$\mathrm{VI}_{\mathrm{debias}} = \frac{\sqrt{\sum_{i=1}^{N}[S_i - \langle S_i\rangle]^2 - \sum_{i=1}^{N}(\sigma_i^2)}}{N\langle S_i\rangle} \tag{1.34}$$

One can rewrite the above equation to calculate the uncertainties as:

$$\mathrm{VI}_{\mathrm{debias}} = \frac{\sqrt{A}}{B}, \quad A \equiv \sum_{i=1}^{N}\big(S_i - \mu\big)^2 - \sum_{i=1}^{N}\sigma_i^2, \quad B \equiv N\mu, \tag{1.35}$$

$$\Delta_{\mathrm{VI}_{\mathrm{debias}}} = \sqrt{\left(\frac{\partial \mathrm{VI}_{\mathrm{debias}}}{\partial A}\,\sigma_A\right)^2 + \left(\frac{\partial \mathrm{VI}_{\mathrm{debias}}}{\partial B}\,\sigma_B\right)^2} \tag{1.36}$$

$$= \sqrt{\left(\frac{1}{2\sqrt{A}}\,\frac{1}{B}\,\sigma_A\right)^2 + \left(-\frac{\sqrt{A}}{B^2}\,\sigma_B\right)^2}, \tag{1.37}$$

$$\sigma_A = \sqrt{\sum_{i=1}^{N}\big(2\,(S_i - \mu)\,\sigma_i\big)^2}, \qquad \sigma_B = \sqrt{\big(N\,\mathrm{std}(S)\big)^2} = N\,\mathrm{std}(S). \tag{1.38}$$

It is important to note that the numerator in Equation 1.34 represents the intrinsic variance (observed variance minus measurement error variance). If the numerator is negative, it indicates that the source is not variable relative to the noise.

In summary, these variability indices provide complementary perspectives on flux density variations, thereby improving the reliability of our variability assessment in this study.

1.6 Objectives

Calibrators, as defined in Section 1.3, are expected to be non-variable radio sources that are well-studied and reliable. However, many calibrators are strong radio sources, some of which have an AGN at their core and therefore exhibit variability as detailed in Section 1.4.1. With radio emissions from radio-loud AGN varying on the timescales of years to less than a day in all frequency bands of the EM spectrum (Wagner and Witzel, 1995), monitoring calibrator variability is important for the long-term operations and fidelity of scientific products produced by MeerKAT.

We therefore aim to:

1. Characterise a sample of southern sky calibrators observed by MeerKAT through detailed source modeling.

2. Conduct a comprehensive flux stability analysis of a sample of southern sky calibrators observed by MeerKAT.

These objectives are crucial in optimizing calibration strategies for ongoing SKA precursor science, e.g, MeerKAT, which relies on stable calibrator sources.

1.7 Thesis Layout

The objectives of this body of work are achieved across five chapters as follows:

1. Chapter 1 provides a foundational introduction to radio astronomy, covering radio telescopes and the application of interferometry techniques. It then presents an overview of the MeerKAT telescope, introduces calibrators, Active Galactic Nuclei (AGN), and the phenomenon of AGN variability. The chapter concludes with a review of previous relevant works and variability metrics, and outlines the specific objectives of this study.

2. Chapter 2 presents the selected calibrator sample, and details the known properties of each calibrator, drawn from existing literature. This is followed by the methodology used to characterise the calibrator sample through the creation of polynomial spectral models. The polynomial spectral models, including the classification of the sample into peaked (26%), upturn (15%), and linear (59%) spectral types, are presented at the end of the chapter.

3. Chapter 3 details the entire radio data reduction process from raw visibilities - flagging - calibration and imaging undertaken to produce radio light curves utilised in the flux stability analysis in 4.

4. Chapter 4 presents the comprehensive flux stability analysis, encompassing both Long-Term Variability (LTV) over approximately two years and Short-Term Variability (STV) over a single observation period (an 8 hour observation).

5. Finally, in Chapter 5, a comprehensive summary of the entire work is presented, drawing together the conclusions from the source modeling and variability analyses. This chapter also provides recommendations for future work.

Chapter 2

Characterising Southern Sky Calibrators: Sample Selection and Source Modeling

In this chapter, we undertake our first objective as outlined in Section 1.6 to: Characterise a sample of southern sky calibrators observed by MeerKAT through source modeling. Section 2.1 details the steps followed to create our sample from the MeerKAT calibrator lists [1], followed by a summary of the known properties of the sample from existing literature in Section 2.1.1. Finally, in Section 2.2, we introduce spectral models, the methodology and software (see Section 2.2.1) used to characterise our sample of calibrators, and present the results in Section 2.2.2.

2.1 Calibrator Sample

MeerKAT has, to date, observed over a hundred southern sky calibrators in the course of its operation. We created our subsample by choosing calibrators that had been observed in all three MeerKAT bands (U-, L-, and S-band) and that had at least 4 flux density measurements over $\approx$ 2 years (33 calibrators). This was done in consideration of the LTV analysis to follow.

[1] https://skaafrica.atlassian.net/wiki/spaces/ESDKB/overview?homepageId=41025669

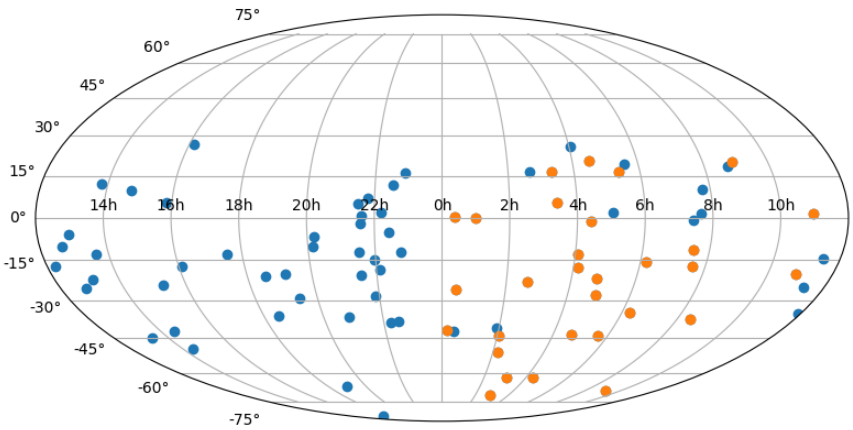

Figure 2.1: Distribution of MeerKAT calibrators across the sky in blue, the orange circles highlight sources in our sample.

The data used is not from observations dedicated to this study; rather, we exclusively utilised pre-existing MeerKAT data. More information on the data used in the LTV and STV analyses is given in Sections 3.5 and 3.1, respectively. It should be noted that this selection process introduces a potential bias favouring bright, frequently observed calibrators. Therefore, the resulting sample and subsequent conclusions may not be fully representative of the general population of southern sky calibrators. For the characterisation of the sample as detailed in this chapter, we used the flux densities and accompanying uncertainties published in the MeerKAT Knowledge Base [2] for the three bands: (U-band[3], L-band[4], and S-band[5]). The distribution of our sample of calibrators in the sky is shown in Figure 2.1.

A Spectral Energy Distribution (SED) provides a multi-wavelength fingerprint of an astronomical source, providing insight into its physical processes, energy output, and underlying emission mechanisms (Ross et al., 2020). To accurately capture the intrinsic spectral shape, particularly the presence of curvature that may be present in the spectra of the calibrators in our sample, a broadband SED was required. We therefore supplemented the 3-band

[2]https://skaafrica.atlassian.net/wiki/spaces/ESDKB/overview?homepageId=41025669
[3]https://skaafrica.atlassian.net/wiki/spaces/ESDKB/pages/1479802903/UHF+gain+calibrators
[4]https://skaafrica.atlassian.net/wiki/spaces/ESDKB/pages/1452146701/L-band+gain+calibrators
[5]https://skaafrica.atlassian.net/wiki/spaces/ESDKB/pages/1589477389/S-band+gain+calibrators

MeerKAT data with additional archival survey data.

We used the virtual observatory (VO) database Vizier (Ochsenbein, F. et al., 2000) to directly query several surveys by running a proximity search (within the synthesized beam of each survey) to collate the known properties of each calibrator in our sample. This included measurements of their flux densities (S_ν) at an observed frequency ν and their corresponding uncertainties. Table 2.1 summarizes the key characteristics of the radio surveys from which additional flux density data were obtained for our calibrator sources. The following surveys were queried for our analysis:

- **The Parkes-MIT-NRAO Survey (PMN)**

  The PMN survey (Wright et al., 1994) was carried out by the Parkes 64 m radio telescope at a frequency of 4.8 GHz with a spatial resolution of $\approx 4.2'$ (FWHM) in June and November 1990. The survey was divided into several zones distinguished by their declination. The Southern zone covered a declination (δ) range of $-87.5^\circ \leq \delta \leq -37^\circ$. A source catalog was compiled from each of the survey zones using an optimum filter method as described by Wright et al. (1994). Sources with flux densities between 20 mJy to 50 mJy were detected in the Southern zone. Additionally, a set of images was produced for each zone with an effective resolution of $\approx 5'$ (FWHM).

- **Sydney University Molonglo Sky Survey (SUMSS)**

  The SUMSS (Mauch et al., 2003b) was carried out by the Molonglo Observatory Synthesis Telescope (MOST) in its upgraded wide-field capability at a frequency of 843 MHz. The survey consists of $4.3^\circ \times 4.3^\circ$ mosaic images with $45'' \times 45''$ resolution and a sensitivity of 1 mJy (1σ noise level). The initial catalog lists 107,765 radio sources and covers approximately $3500^\circ \times 3500^\circ$ of the Southern sky with declination $\delta \leq 30^\circ$ excluding areas within 10° of the Galactic plane. SUMSS together with the NRAO VLA Sky Survey (NVSS) provide a complete (i.e, a full, systematic sky coverage) survey of the radio sky with 7,000 sources found in the overlap region of the two.

- **Molonglo Radio Catalog Survey (MRC)**

  The MRC survey (Large et al., 1981) was conducted by the Molonglo Radio Telescope at a frequency of 408 MHz and a declination range of $18.5^\circ \geq \delta \geq -85.0^\circ$. The survey produced a catalog of 12,141 sources with flux densities ≥ 0.7 Jy whose source positions have a standard error between $3''$and$10''$. The catalog also contains notes on source morphology and cross-references with the Parkes Catalogues.

- **Galactic and Extragalactic All-sky MWA Survey (GLEAM)**

  The GLEAM survey (Hurley-Walker et al., 2017) was conducted using an SKA precursor, the Murchison Wide-field Array (MWA) telescope in Western Australia. The first extra-galactic catalog from the survey utilizes only the first year of observations covering declinations South of 30°, excluding the Galactic plane and other areas such as the Magellanic Clouds. The catalog contains 307,456 radio sources selected from an integrated image centered at 200 MHz with a resolution of $\approx 2'$. The catalog is 90% complete (i.e, the fraction of real sources detected above a given brightness) at a flux density of 170 mJy and 55% complete at a flux density of 55 mJy with a reliability of 99.97% above the detection threshold of 5σ (≈ 50 mJy).

- **NVSS**

  Using the NRAO Very Large Array (VLA), the NVSS (Condon et al., 1998a) mapped the sky North of declination -40° at a frequency of 1.4 GHz. The survey produced 2,326 continuum 'cubes' with three axes containing Stokes I, Q, and U images covering a $4^\circ \times 4^\circ$ area and a catalog listing ≈ 2 million discrete radio sources detected above a flux density of ≈ 2.5 mJy. The images all have $45''$ (FWHM) angular resolution and near uniform sensitivity. The RMS brightness fluctuations are ≈ 0.45 mJy/beam (0.14K) for Stokes I and ≈ 0.29 mJy/beam (0.09K) for Stokes Q and U.

- **Texas Survey**

  The Texas Survey (Douglas et al., 1996) was conducted between 1974 and 1983 by the Texas Interferometer at a frequency of 365 MHz. The survey covers a declination range of -35.5°to71.5°. The survey lists positions, flux densities, indications of source variability, and simple structure models for 66,841 sources. Compared to other available

surveys, the Texas survey is estimated to be 90% complete at 0.4 Jy and 80%, complete at 0.25 Jy, and nearly free of spurious sources (Douglas et al., 1996). It should be noted that poor UV coverage leads to irregular beam shapes and lobe shifts, hampering the accurate modeling of extended sources.

- **S-band Polarisation All-Sky Survey (S-PASS)**

  Using the 64 m Parkes radio telescope, the S-PASS (Meyers et al., 2017) mapped the entire Southern sky excluding the galactic plane between October 2007 and January 2010 at 2.3 GHz. Using a set of 107 Stokes I images with 10.75′ resolution from the survey data, Meyers et al. (2017) created a catalog of 23,389 extra-galactic sources. The S-PASS source catalog at a flux density of 225 mJy is more than 95% complete with source positions accurate to within 35″ and ≈ 8% of the sources resolved (Meyers et al., 2017).

- **The Rapid ASKAP Continuum Survey (RACS)**

  The RACS survey is the first large sky survey using the Australian Square Kilometre Array Pathfinder (ASKAP) and covering declinations South of 41° at a central frequency of 887.5 MHz (Hale et al., 2021). The resulting first extra-galactic catalog from ASKAP lists ≈ 2.1 million sources with coverage excluding the galactic plane and has a 95% point source completeness at an integrated flux density of ≈ 3 mJy (Hale et al., 2021).

2.1.1 Known Properties

In this section, we present a summary of the known properties of the calibrators in our sample as reported in various published literature sources. This includes the classes, such as Radio Source (RG), Blazar (BL), Quasar (QSO), the redshift z, and flux density measurements at different frequencies. In some cases, the available information in the literature was limited.

Survey	Frequency (MHz)	Sensitivity (mJy/beam)	Resolution ($''$)	Dec limit
GLEAM	72-216	7	~ 120	$\leq 30^\circ$
TEXAS	365	0.25	~ 50	-35.5°to71.5°
MRC	408	0.7	45	$18.5^\circ$to-85°
SUMSS	843	1	45	$\leq -30^\circ$
NVSS	1400	0.45	45	$\geq -40^\circ$
S-PASS	2300	0.225	~ 600	$\leq -1^\circ$
PMN	4800	0.2 - 0.5	~ 252	$-87.5^\circ$to-37°

Table 2.1: The table summarizes the key characteristics of the radio surveys from which additional flux density data were obtained for our calibrator sources. The first column gives the survey name, followed by the observing frequencies and the average survey sensitivities. The fourth column gives the survey resolution. It should be noted that some of the resolutions for the surveys are declination and frequency dependent; therefore, an approximate value is given. The last column gives the declination limit for each of the surveys.

PKS J0010-4153

This source is classified as an AGN with the designation ICRF J001052.5-415310 in the newly updated map of the celestial sphere (ICRF3) based on nearly 40 years of precise radio observations that have replaced the previous ICRF2 frame adopted in 2009 (Charlot et al., 2020). It is located at a redshift $z = 1.13$. Labiano et al. (2007) identified optical counterparts of the Gigahertz Peaked Spectrum (GPS) radio source, where previous attempts had failed, as the galaxy is faint and lacks clear emission lines. The flux density measurements of the source at 5500 MHz are ~ 1.31 Jy as reported in Wright and Otrupcek (1990), and ~ 1.35 Jy from the Australia Telescope 20 GHz (AT20G) Survey by Australia Telescope Compact Array (ATCA). The AT20G is a blind radio survey carried out at 20 GHz with ATCA from 2004 - 2008 (Murphy et al., 2010). At 1410 MHz, the flux density reported was ~ 4.44 Jy by Wright and Otrupcek (1990). MeerKAT's L, U, and S band flux densities are ~ 4.45 Jy,~ 5.78 Jy, and ~ 2.63 Jy respectively.

PKS J0022+0014

This source is classified as a flat-spectrum radio quasar (FSRQ). It is located at a redshift $z = 0.31$ with an average flux density of ~ 1.1 Jy measured at 5500 MHz between 2011 - 2013 (Kassaye, 2015). A flux density of ~ 2.2 Jy was measured at 2100 MHz at the end of 2010 (ATCA Database). MeerKAT's L, U, and S band flux densities are ~ 2.9 Jy, ~ 3.21 Jy, and ~ 2 Jy respectively.

PKS J0025-2602

This source is classified as a flat-spectrum radio quasar (FSRQ). It is located at a redshift $z = 0.33$. It is additionally classified as a Compact Steep Spectrum (CSS) source because of its radio spectrum that peaks at a frequency lower than 500 MHz (Kassaye, 2015). Flux density measurements between 2009 - 2013 at 2100 MHz were of similar magnitude at ~ 6.8 Jy. Similarly, flux density measurements taken at 5500 MHz between 2009 and 2014 were of a magnitude of ~ 3.3 Jy. MeerKAT's L, U, and S band flux densities are ~ 8.73 Jy, ~ 10.81 Jy, and ~ 6.15 Jy respectively.

PKS J0059+0006

This source is classified as a quasar (QSO). It is located at a redshift $z = 0.72$. The source has a unique high level of polarization, a compact core, and a jet extending over 20 millionths of an arcsecond from observations at 4.8 GHz frequencies (Edwards and Tingay, 2004). The flux density measurements at 5000 MHz are ~ 1.37 Jy from Laurent-Muehleisen et al. (1997) and ~ 1.43 Jy from Wright and Otrupcek (1990). At 1400 MHz, the flux density is ~ 2.4 Jy from Wright and Otrupcek (1990) and ~ 1.37 Jy from Ching et al. (2017). MeerKAT's L, U, and S band flux densities are ~ 2.45 Jy, ~ 2.82 Jy, and ~ 2.07 Jy respectively.

PKS J0137+3309 (3C48)

This source is classified as a quasar (QSO) with the alternate identifier 3C48. It is located at a redshift $z = 0.37$. This source is reported to have a complex radio morphology attributed to the interaction of the jet with the host galaxy's interstellar medium, a conclusion further supported by the properties of the blue-shifted gas detected in forbidden emission lines (Gupta et al., 2006). This quasar shows no flux variations as expected and has been in use as a primary flux calibrator (Peng et al., 2000). The flux densities at 1400 MHz are similar at ~ 15.7 Jy from Laing and Peacock (1980), ~ 15.9 Jy from Kuehr et al. (1981), ~ 15.8 Jy from White and Becker (1992), ~ 16.0 Jy from Condon et al. (1998b) and ~ 15.9 Jy from Matthews and Reid (2007). MeerKAT's L, U, and S band flux densities are ~ 16.11 Jy, ~ 21.5 Jy, and~ 10.26 Jy respectively.

PKS J0203-4349

The source is classified as a radio galaxy (RG). It is located at a redshift $z = 0.45$. The source appears to be stable with different flux density measurements at 5000 MHz being similar; ~ 1.01 Jy as reported in Wright and Otrupcek (1990), ~ 1.01 Jy as reported in the Molonglo Southern 4Jy Sample II in 2006 (Burgess and Hunstead, 2006) and ~ 1.02 Jy from the AT20G Survey (Murphy et al., 2010). MeerKAT's L, U, and S band flux densities are ~ 2.73 Jy, ~ 3.55 Jy, and ~ 1.8 Jy respectively.

PKS J0210-5101

This source is classified as a quasar (QSO) with the alternate identifier QSO B0208-512 and is located at a redshift $z = 1.00$. It emits intense γ-rays with short-term variation (tens of days) and was the second southern AGN (after 3C 279) detected at γ-ray energies, making it a good candidate for study when exploring a correlation between γ-rays and radio waves (Shen et al., 1998). The flux densities measured at 5000 MHz decrease over the years with the first being ~ 3.21 Jy as reported by Wright and Otrupcek (1990), ~ 3.04 Jy from the AT20G Survey (Murphy et al., 2010), and ~ 2.95 Jy as reported in Burgess and Hunstead (2006). MeerKAT's L, U, and S band flux densities are ~ 3.4 Jy, ~ 2.82 Jy, and ~ 3.33 Jy respectively.

PKS J0240-2309

This source is classified as a quasar (QSO). It is located at a redshift $z = 2.22$. It exhibits a core-jet structure with its compact core dominating at 2 GHz and 5 GHz (Edwards and Tingay, 2004). The variability indices of this source at 1.4 GHz, 2.5 GHz, 4.8 GHz, and 8.6 GHz are 1.0%, 2.0%, 3.0%, and 5.0% respectively as reported by the ATCA Monitoring Observations of 202 Compact Sources at 16 epochs between October 1996 and February 2000 (Tingay et al., 2003). The flux densities measured at 2100 MHz (~ 5.1 Jy) between 2009 - 2013, and at 5500 MHz (~ 2.1 Jy) between 2009 - 2013 show little fluctuation for each respective frequency (ATCA Database). MeerKAT's L, U, and S band flux densities are ~ 5.94 Jy, ~ 5.34 Jy and ~ 5.3 Jy respectively.

PKS J0252-7104

PKS J0252-7104 (also known as PKS 0252-71) is classified as a compact steep-spectrum (CSS) radio source with a spectral index of $\alpha \simeq -1.02$ (Tadhunter et al., 1993; Randall et al., 2011). Optical spectroscopy places the source at a redshift of $z \simeq 0.568$, consistent with its identification as a host galaxy in the CSS population (Tadhunter et al., 1993). Its compact nature (linear size $\lesssim 20$ kpc) makes it unresolved at arcsecond resolution in L- and S-band MeerKAT observations, where it is frequently employed as a phase and gain calibrator. Po-

larimetric calibration studies also show that PKS J0252-7104 exhibits very low instrumental leakage (of the order $\sim 0.02 - 0.03\%$), further supporting its suitability as a stable calibrator source [6]. MeerKAT's L, U, and S band flux densities are ~ 5.81 Jy, ~ 7.97 Jy, and ~ 3.32 Jy respectively.

PKS J0303-6211

This source is classified as a flat-spectrum radio quasar (FSRQ). It is located at a redshift $z = 1.35$ (Kassaye, 2015). The variability indices of this source at 1.4 GHz, 2.5 GHz, 4.8 GHz, and 8.6 GHz are 4.0%, 4.0%, 2.0%, and 2.0% respectively as reported by Tingay et al. (2003). The flux density of the source increased from ~ 2.8 Jy in 2009 to ~ 3.5 Jy in 2010 at 2100 MHz. Flux density measurements were recorded at 5500 MHz between 2009 - 2014 with the maximum being ~ 2.4 Jy in 2009 and the minimum ~ 1.8 Jy in 2013 (ATCA Database). MeerKAT's L, U, and S band flux densities are ~ 3.19 Jy, ~ 2.26 Jy, and ~ 2.62 Jy respectively.

PKS J0318+1628

This source is classified as a quasar (QSO). It is located at a redshift $z = 0.91$. The source exhibits a steep spectrum at frequencies greater than 1 GHz and either a flat or inverted spectrum at low frequencies (Kassaye, 2015). MeerKAT's L, U, and S band flux densities are ~ 7.62 Jy, ~ 8.43 Jy, and ~ 5.33 Jy respectively.

PKS J0323+0534

This source is categorized as a Gigahertz-Peaked Spectrum (GPS) source. It is located at a redshift $z = 0.18$ (Kassaye, 2015). Very-long-baseline interferometry (VLBI) observations show that the source shows a strong diffuse component and a weak extended component in the South (Liu et al., 2007). The flux density measurements taken at 5500 MHz in 2011 - 2014 are similar; ~ 0.8 Jy (ATCA Database). MeerKAT's L, U, and S band flux densities are

[6] https://archive-gw-1.kat.ac.za/public/meerkat/MeerKAT64-Widefield-Polarimetry-of-DEEP2.pd

~ 2.77 Jy, ~ 3.75 Jy, and ~ 1.65 Jy respectively.

PKS J0405-1308

This source is a steep-spectrum quasar (SSQ) with a compact core. It is located at a redshift $z = 0.57$ and exhibits faint jet emission to the southeast (Edwards and Tingay, 2004). The variability indices of this source at 1.4 GHz, 2.5 GHz, 4.8 GHz, and 8.6 GHz are 1.0%, 3.0%, 5.0%, and 15.0% respectively as reported by Tingay et al. (2003). At 2100 MHz, its flux density decreased from ~ 3.6 Jy in 2009 to ~ 3.3 Jy in 2011 (Kassaye, 2015). At 5500 MHz, flux densities were measured between 2009 - 2012, two of which were similar at ~ 2.7 Jy and one slightly lower at ~ 2.5 Jy at the end of 2011 (ATCA Database). MeerKAT's L, U, and S band flux densities are ~ 3.95 Jy, ~ 4.6 Jy, and ~ 3.42 Jy respectively.

PKS J0409-1757

This source is a steep-spectrum quasar (SSQ). It is located at a redshift $z = 0.72$ (Kassaye, 2015). The flux densities of the source measured at 2100 MHz in 2009 and 2012 were similar at ~ 1.6 Jy. The flux density was ~ 0.7 Jy measured at 5500 MHz in 2009, 2011, and 2012 (ATCA Database). MeerKAT's L, U, and S band flux densities are ~ 2.2 Jy, ~ 2.97 Jy, and ~ 1.44 Jy respectively.

PKS J0420-6223

This source is a steep-spectrum radio galaxy (RG). It is located at a redshift $z = 0.81$ (Kassaye, 2015). The flux densities of the source measured at 2100 MHz between 2007 - 2012 were ~ 2.2 Jy. The flux densities measured at 5500 MHz were ~ 1.9 Jy between 2009 -2012 (ATCA Database). MeerKAT's L, U, and S band flux densities are ~ 3.33 Jy,~ 4.86 Jy, and ~ 1.88 Jy respectively.

PKS J0423-0120

This source is classified as a quasar (QSO) with the alternate identifier QSO B0420-0127. It is located at a redshift $z = 0.92$. It has a dominant core with a complex polarization pattern, implying the presence of a multi-component substructure (Jorstad et al., 2005). The flux density measurements at 1400 MHz are reported as ~ 2.24 Jy by Wright and Otrupcek (1990) and ~ 2.73 Jy from the The NRAO VLA Sky Survey (Condon et al., 1998b). MeerKAT's L, U, and S band flux densities are ~ 1.2 Jy, ~ 1.1 Jy, and ~ 3.1 Jy respectively.

PKS J0431+2037

This source is classified as a radio galaxy (RG) in the ICRF3 with the alternate identifier OF +247. It is located at a redshift $z = 0.23$ (Charlot et al., 2020). It is a very compact source whose spectrum peaks at 1 GHz and has a turnover at lower frequencies. Therefore, it is better classified as a GPS rather than a CSS source as discussed by Tyul'Bashev and Chernikov (2000b). The flux density measurements at 1400 MHz are ~ 3.8 Jy from Wright and Otrupcek (1990) and ~ 3.76 Jy from Condon et al. (1998b). MeerKAT's U and S band flux densities are ~ 3.41 Jy, and ~ 3.62 Jy respectively.

PKS J0440-4333

This source is an extremely luminous quasar (QSO). It is located at a redshift $z = 2.86$. It exhibits a flat spectrum at low frequencies and a steep spectrum at frequencies above 5 GHz (Kassaye, 2015). VLBI observations of the source reveal a core-jet structure at 2.3 GHz. The variability indices of this source at 1.4 GHz, 2.5 GHz, 4.8 GHz, and 8.6 GHz are 2.0%, 5.0%, 10.0%, and 10.0% respectively as reported by Tingay et al. (2003). The flux density measured at 2100 MHz decreased from ~ 3.9 Jy in 2009 to ~ 3.3 Jy in 2012 (Kassaye, 2015). The flux densities measured at 5500 MHz between 2011 and 2013 have similar magnitudes of~ 1.9 Jy with 2009 having a higher measurement of~ 2.5 Jy (ATCA Database). MeerKAT's L, U, and S band flux densities are ~ 3.59 Jy, ~ 4.56 Jy, and ~ 2.88 Jy respectively.

PKS J0447-2203

This source is classified as a radio source (RG) in the ICRF3 (Charlot et al., 2020). The flux density measurement ~ 2.0 Jy from the Parkes Catalog in 1990 at 1410 MHz is similar to that reported in 1998 by the NRAO VLA Sky Survey at 1400 MHz; ~ 2.09 Jy (Condon et al., 1998b). MeerKAT's L and U band flux densities are ~ 2.03 Jy, and ~ 2.79 Jy respectively.

PKS J0453-2807

This is a flat-spectrum quasar (FSRQ) with a jet structure. It is located at a redshift $z = 2.56$ (Scott et al., 2004). The variability indices of this source at 1.4 GHz, 2.5 GHz, 4.8 GHz, and 8.6 GHz are 2.0%, 3.0%, 5.0%, and 9.0% respectively as reported by Tingay et al. (2003). The flux density measured at 2100 MHz of the source decreased slightly from ~ 2.3 Jy in 2009 to ~ 2.1 Jy in 2011 (Kassaye, 2015). The two flux densities measured at 5500 MHz in 2011 had almost equal magnitudes of ~ 1.9 Jy (ATCA Database). MeerKAT's L, U, and S band flux densities are ~ 2.19 Jy, ~ 2.14 Jy, and ~ 1.85 Jy respectively.

PKS J0521+1638

This source is classified as a quasar (QSO) with the designation ICRF J052109.8+163822 and alternate identifier 3C138. The source has a bright radio core and a jet embedded in the northeastern lobe (Axon et al., 2000). It is located at a redshift $z = 0.76$ with a projected jet length of 3.2 kpc (Liu and Zhang, 2002). The source shows no flux variations and has been used as a primary flux calibrator, as reported in the long-term monitoring of a selection of radio sources by Peng et al. (2000). The flux densities measured at 5500 MHz are ~ 4.04 Jy, and ~ 4.04 Jy by Wright and Otrupcek (1990). The flux density measured by the Effelsberg radio telescope in 2005 at 4850 MHz was ~ 4.12 Jy (Mantovani et al., 2009). MeerKAT's L, U, and S band flux densities are ~ 8.33 Jy, ~ 9.98 Jy, and ~ 6.39 Jy respectively.

PKS J0538-4405

This source is classified as a flat-spectrum quasar (FSRQ). It is located at a redshift $z = 0.89$ and has shown variability in almost all the wavelengths detected (Kassaye, 2015). The variability indices of this source at 1.4 GHz, 2.5 GHz, 4.8 GHz, and 8.6 GHz are 22.0%, 24.0%, 30.0%, and 35.0% respectively as reported by Tingay et al. (2003). VLBI imaging of the source at 5 GHz showed an asymmetric core-jet structure (Shen et al., 1998). As mentioned, the source is highly variable, with its flux density changing significantly from ~ 4.0 Jy in 2006 to ~ 7.8 Jy in 2011 as measured at 2100 MHz (Kassaye, 2015). The flux densities measured between 2008 - 2013 at 5500 MHz also show high variance with the highest flux density value being~ 10.9 Jy in 2011 and the minimum ~ 4.9 Jy in 2013 (ATCA Database). MeerKAT's L, U, and S band flux densities are ~ 2.16 Jy, ~ 2.03 Jy, and ~ 3.45 Jy respectively.

PKS J0609-1542

This source is classified as a quasar (QSO) with the alternate identifier QSO B0607-157. It is located at a redshift $z = 0.32$. It has an extremely compact core (Scott et al., 2004). Its flux density measurements reported at 5000 MHz are ~ 1.77 Jy (Wright and Otrupcek, 1990), ~ 3.76 Jy from the AT20G Survey (Murphy et al., 2010), and ~ 4.2 Jy as reported by the VSOP 5 GHz Active Galactic Nucleus Survey in 2004 (Scott et al., 2004). MeerKAT's L, U, and S band flux densities are ~ 1.67 Jy, ~ 1.81 Jy, and ~ 4.16 Jy respectively.

PKS J0616-3456

This source has the designation ICRF J061635.9-345616 (Charlot et al., 2020). It is located at a redshift $z = 0.33$ and is associated with a pair of galaxies. The source has the measured flux densities ~ 2.76 Jy at 1400 MHz as reported by Tingay et al. (2003) in 2003, ~ 0.13 Jy at 2300 MHz in 2005 as reported in the Fourth extension of the VLBA Calibrator Survey and ~ 1.54 Jy at 5000 MHz from the AT20G Survey (Murphy et al., 2010). MeerKAT's L, U, and S band flux densities are ~ 2.90 Jy, ~ 3.37 Jy, and ~ 2.31 Jy respectively.

PKS J0632+1022 (4C10.20)

This source is classified as a radio galaxy (RG) with the alternate identifier 4C10.20. The source has the flux densities ~ 2.91 Jy from White and Becker (1992), and ~ 2.38 Jy from the NRAO VLA Sky Survey at 1400 MHz (Condon et al., 1998b). MeerKAT's L, U, and S band flux densities are ~ 2.43 Jy, ~ 2.56 Jy, and ~ 1.63 Jy respectively.

PKS J0730-1141

This source is classified as a quasar (QSO) by Véron-Cetty and Véron (2006). It is located at a redshift $z = 1.59$ and is situated within 10° of the galactic plane. Imaging the source to investigate its substructure revealed a jet that appeared to have a $\geq 90^{\circ}$ bend (Kellermann et al., 1998). The source has the flux densities ~ 2.22 Jy at 5000 MHz, ~ 1.95 Jy at 2700 MHz from Wright and Otrupcek (1990) and ~ 2.22 Jy at 1400 MHz (Kharb et al., 2010). MeerKAT's L, U, and S band flux densities are ~ 2.26 Jy, ~ 2.54 Jy, and ~ 3.42 Jy respectively.

PKS J0735-1735

This source is classified as a radio source (RG) by Charlot et al. (2020). The flux density measurement of the source at 5500 MHz is ~ 2.02 Jy (Wright and Otrupcek, 1990). The flux density measurement ~ 2.7 Jy by Wright and Otrupcek (1990) is lower than ~ 2.98 Jy reported in 1998 by Condon et al. (1998b) at 1410 MHz and 1400 MHz respectively. MeerKAT's L, U, and S band flux densities are ~ 2.6 Jy, ~ 2.76 Jy, and ~ 2.33 Jy respectively.

PKS J0828-3731

This source is classified as a quasar (QSO). It has the measured flux density of ~ 3.6 Jy at 5500 MHz, slightly higher than the ~ 3.4 Jy at 1410 MHz as reported by Wright and Otrupcek (1990). MeerKAT's L, U, and S band flux densities are ~ 2.09 Jy,~ 1.58 Jy, and ~ 2.34 Jy respectively.

PKS J0854+2006 (OJ+287)

This source is classified as a blazer (BL) by Lin et al. (2012) with the alternate identifier OJ+287. It is located at a redshift $z = 0.306$. This is a well-studied BL Lac object with a possible brightening and dimming 12 year cycle in the optical regime, possibly due to a binary black hole system as discussed by Hovatta et al. (2008). Previous studies found cycles on timescales of 1.66 and 1.12 years in total flux and polarization, explained by a shock-in-jet model. The source also revealed multiple timescales of variability as well as an intriguing gap in their presence between 1993 and 2000 (Hovatta et al., 2008). The flux density measurements at 1400 MHz are reported as ~ 2.16 Jy by White and Becker (1992), ~ 1.51 Jy by Condon et al. (1998b), and ~ 2.28 Jy by Witzel et al. (1979). MeerKAT's L, U, and S band flux densities are ~ 2.05 Jy, ~ 1.77 Jy, and ~ 5.09 Jy respectively.

PKS J0906-6829

This source is classified as a radio galaxy (RG). It is located at a redshift $z = 0.56$. The optical field of the source is partially obscured by the star HD 78913 (Burgess and Hunstead, 2006). The source has the flux density measurements ~ 0.42 Jy, and ~ 1.7 Jy at 5000 MHz, and ~ 1.7 Jy at 1400 MHz (Wright and Otrupcek, 1990). MeerKAT's L, U, and S band flux densities are~ 1.81 Jy, ~ 2.72 Jy, and ~ 0.91 Jy respectively.

PKS J1008+0730

This source is classified as a radio galaxy (RG) with the alternate identifier 3C237.0. It is located at a redshift $z = 0.88$. The numerous observations of this source at various frequencies and resolutions indicate that it has an east-west double structure with one arc-second separation (Tyul'Bashev and Chernikov, 2000a). The source has the flux densities ~ 6.01 Jy (Matthews and Reid, 2007), and ~ 6.62 Jy (Best et al., 2014) at 1400 MHz. MeerKAT's L, U, and S band flux densities are ~ 6.53 Jy, ~ 8.77 Jy, and ~ 3.88 Jy respectively.

PKS J1051-2023

This source is classified as a radio galaxy (RG). It is located at a redshift $z = 1.12$ (Burgess and Hunstead, 2006). The measured flux densities of the source at 5000 MHz and 2700 MHz are ~ 0.4 Jy and ~ 0.46 Jy from Murphy et al. (2010) and Wright and Otrupcek (1990) respectively. MeerKAT's L and U band flux densities are ~ 1.44 Jy, and ~ 2.13 Jy respectively.

PKS J1058+0133

This source is classified as a high optical polarization quasar(HPQ) with the designation ICRF J105829.6+013358 and alternate identifier QSO B1055+018. It is located at a redshift $z = 0.89$ (Lister et al., 1998). Early studies report that observations of the source at 43 GHz revealed three jet components: a core, a compact inner jet, and a more extended outer jet displaying proper motion and recurring flares in radio brightness every 1–2 years (Lister et al., 1998). More recent studies based on observations made over 20 years over multiple frequencies report that the source exhibits recurring brightness flares about every 4.3 years at lower frequencies (22 GHz and 37 GHz) (Hovatta et al., 2008). In comparison, the pattern is less clear at higher frequencies. This reveals that the source has a jet structure with multiple components with flares and twists, suggesting a complex and dynamic environment (Hovatta et al., 2008). The flux density measurements at 1400 MHz over the years seem fairly stable; ~ 3.36 Jy (Wright and Otrupcek, 1990), ~ 3.22 Jy (Ching et al., 2017), and ~ 3.07 Jy (Tingay et al., 2003). MeerKAT's L, U, and S band flux densities are ~ 3.67 Jy, ~ 3.42 Jy, and ~ 4.29 Jy respectively.

PKS J1939-6342

This source is classified as a Seyfert 2 Galaxy in the ICRF3 with the designation ICRF J193925.0-634245. It is located at a redshift $z = 0.185$. The source is one of the earliest known GPS sources (Edwards and Tingay, 2004). VLBI imaging reveals a compact double morphology with a separation of ≈ 40 mas (Dodson et al., 2008). The source is used as a flux calibrator by ATCA because of its stable flux density and compact structure (Kedziora-Chudczer et al., 1998). The flux density measurements are ~ 16.4 Jy (Kuehr et al., 1981) and

$\sim$ 15.0 Jy (ATCA Database) at 1400 MHz and $\sim$ 13.7 Jy from the SUMSS survey (Mauch et al., 2003a) at 843 MHz. Data from the Australia Telescope National Facility (ATNF) shows that its flux density has varied by less than $\sim 2\%$ at 1384 MHz and less than $\sim 0.4\%$ at 1757 MHz between the years 2000 - 2010 (Kassaye, 2015). MeerKAT's L and U band flux densities are $\sim$ 14.55 Jy and $\sim$ 13.96 Jy respectively.

PKS J2152-2828

This source is classified as a steep-spectrum radio galaxy (RG). It is located at a redshift $z = 0.479$ with an average flux density of $\sim$ 1.1 Jy measured at 5500 MHz between 2010 - 2013 (Kassaye, 2015). A flux density of $\sim$ 2.1 Jy was measured at 2100 MHz at the end of 2010 (ATCA Database). MeerKAT's L, U, and S band flux densities are $\sim$ 2.92 Jy, $\sim$ 4.05 Jy, and $\sim$ 1.82 Jy respectively.

2.2 Source Modeling

Spectral energy distribution (SED) analysis is of direct relevance as the creation of accurate, frequency-dependent models for radio calibrators is foundational to the calibration process. Spectral models describe how the flux density of radiation varies as a function of frequency (Thompson et al., 2001). Spectral models are essential for correcting frequency-dependent effects and ensuring the fidelity of all subsequent science observations.

The spectral models of calibrator sources used in the calibration process are typically calculated from careful measurements and published in catalogs as polynomial models (Molteno, 2024). These models are a polynomial fit of the spectral flux density ($\log S$) as a function of the logarithm of the normalized frequency ν' as given by Equation 2.1. The normalized frequency is defined as $\nu' \equiv \frac{\nu}{\nu_0}$, where ν is the observed frequency and ν_0 is the reference frequency, e.g. 1 GHz (Molteno, 2024).

$$\log S(\nu') = a_0 + a_1 \log(\nu') + a_2 \log(\nu')^2 + ... + a_n \log(\nu')^n \tag{2.1}$$

Although the function above does not reflect the nature of the underlying phenomena, it is useful for estimating the fluxes at different frequencies through interpolation. It is essential to note that the coefficients $(a_0, a_1, a_2, ...)$ of these equations are not entirely independent. There is significant covariance in these polynomial coefficients, meaning that the values of different coefficients are not statistically independent; a change in one coefficient tends to be associated with a change in another. This relationship is the correlation structure of the flux-density model parameters, arising because the coefficients are intrinsically linked as they collectively define the shape of the polynomial curve across the entire frequency range (Molteno, 2024).

Molteno (2024) posits that ignoring this relationship while sampling from a spectral model can result in the loss of spectral information, as demonstrated by the Probability Distribution Function (PDF) of the model spectrum of the calibrator PKS J1939-6342 in Figure 2.2. The PDF is drawn from samples of polynomial coefficients taken from a Markov Chain Monte Carlo (MCMC) chain. Figure 2.2 illustrates that when the covariance between polynomial coefficients is not taken into account, flux samples from the spectral model exhibit an artificially large variance, leading to a significant loss of spectral information compared to when the covariance is included.

2.2.1 Methodology: SPECFIT

Polynomial spectral models of our calibrator sample were constructed using the SPECFIT package[7]. This modeling process utilized a broadband dataset, including 3-band MeerKAT and archival survey flux densities with their corresponding uncertainties, covering a total frequency range from 80 MHz to 4.8 GHz as discussed in Section 2.1. SPECFIT uses Bayesian methods to perform a polynomial fit of the flux density $\log(S)$ as a function of the normalized frequency $\log(\nu')$. Even though standard polynomial fitting software can provide a full correlation matrix, Bayesian methods have the advantage of allowing the use of robust likelihoods that deal with any outliers present in the data well (Molteno, 2024). Furthermore, the posterior probability of the parameters can have interesting structures, such as non-Gaussian

[7] https://github.com/tmolteno/specfit

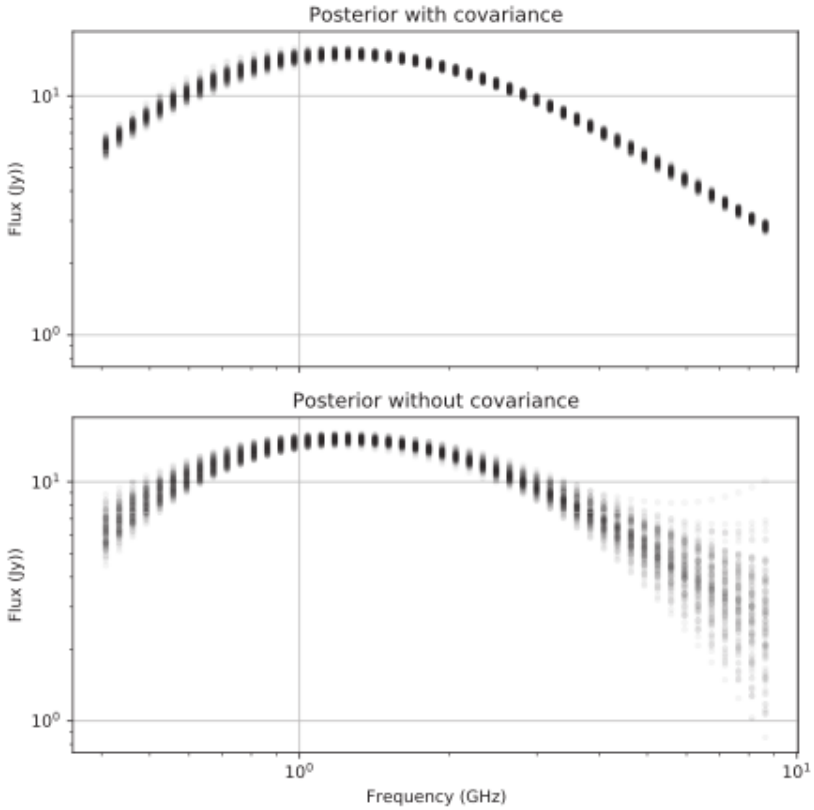

Figure 2.2: Sample model spectrum of PKS J1939-6342 without vs with covariance taken into account. Greater variance is present when the off-diagonal elements of the covariance are not taken into account. Source: Molteno (2024)

.

distributions, that may be of interest.

SPECFIT uses the MCMC technique to sample the posterior probability distribution of the polynomial coefficients ($a_0, a_1, and\ a_2$) given the data (S_ν, and ν). This is achieved by exploring the parameter space and creating a statistical ensemble of the coefficient values that provide a good fit to the data. This sample effectively represents the range of possible models, with the most probable coefficient values being sampled most often. Once the inference process is complete, a scatter plot is produced; the original data points, $\log S$ as a function of $\log \nu'$, overlaid with the fitted polynomial curve. This fitted curve is the non-physical model of the calibrator source's spectrum, obtained by taking the mean of the coefficients in the

ensemble that provide a good fit to the data. As anticipated, some of the sources required a second-order polynomial to capture the complexity and curvature of the data, having a maximum turnover frequency ($\nu_{\rm max}$) or a minimum turnover frequency ($\nu_{\rm min}$). The coefficients of the polynomial models are listed in Table 2.2 for each source.

It is important to note that the turnover frequencies, $\nu_{\rm max}$ and $\nu_{\rm min}$ represented by red dashed lines in our spectral models, may not perfectly align with the minimum or maximum of the polynomial curve. This is not a failure of the fit but an expected outcome of the methodology. For every set of polynomial coefficients sampled in the MCMC process, there is a corresponding maximum/minimum frequency value. This generates a large statistical ensemble (a distribution) of plausible turnover frequencies that are consistent with the data's uncertainty. For the turnover frequencies we report, we fit a Gaussian function to the resulting histogram of the sampled frequencies. The final $\nu_{\rm max}$ or $\nu_{\rm min}$ values are the statistical mean of this fitted Gaussian distribution. This approach robustly estimates the mode of the distribution, providing the most probable turnover frequency. An example is Figure 2.5c, where the minimum frequency $\nu_{\rm min}$ falls to the left of the lowest point of the fitted mean curve, reflecting the scatter and uncertainty of the data.

To quantify the quality and uncertainty of fit, we utilized the output of the MCMC sampling to calculate Credible Intervals (CIs). In the context of our Bayesian analysis, these CIs represent the range of plausible spectral shapes consistent with the posterior probability distribution of the polynomial coefficients. The two key intervals in our spectral plots are:

1. The 68% Credible Interval (CI). This region is indicated with dark shading in the plots (e.g., Figure 2.3a), representing the highest posterior density region, containing the most probable spectral shapes.

2. The 95% Credible Interval (CI). This wider region is indicated with dark shading in the plots (e.g., Figure 2.3a), representing the full range of spectral shapes that are statistically compatible with the observed data at a high degree of certainty.

As discussed earlier, our spectral models are based on published MeerKAT and archival survey flux density data. The survey data are from instruments with different angular resolutions, calibration standards, and sensitivities. Consequently, the measured flux densities may

contain systematic offsets that directly contribute to the observed heterogeneity and width of the confidence intervals (e.g., Figure 2.7f). This systematic uncertainty, rather than purely random noise, often dominates the model uncertainty.

2.2.2 Spectral Model Results

Three distinct classes of spectral models, distinguished by how $\log(S_{\nu'})$ changes with frequency $\log(\nu')$), emerged from our analysis as detailed below:

Peaked Spectrum Sources

In our sample of calibrators, 26% of the sources exhibited a peaked spectrum. For these sources, the flux density $\log(S_{\nu'})$ increases up to a maximum turnover frequency ($\nu_{\max}$), then decreases with increasing frequency. These were a result of fitting a second-order polynomial to capture the data's complexity:

$$\log S(\nu') = a_0 + a_1 \log(\nu') + a_2 \log(\nu')^2 \tag{2.2}$$

The coefficients of the polynomial equation are listed in Table 2.2 for each source.

Extra-galactic peaked-spectrum radio sources are thought to be the progenitors of larger, radio-loud AGN (O'Dea, 1998). Synchrotron self-absorption (SSA) and/or Free-Free absorption (FFA) are believed to be the cause of the characteristic spectral peaks of these sources (de la Parra et al., 2024). There exist various types of peaked-spectrum sources. High-frequency peaked (HFP) sources have spectral peaks above 5 GHz and parsec-scale radio morphologies. Gigahertz-Peaked Spectrum (GPS) and Compact Steep Spectrum (CSS) radio sources make up a significant portion of the bright radio source population (10% and 30% respectively), with GPS sources more compact ($\leq$ 1 kpc) than CSS sources (between 1 and 20 kpc) (O'Dea, 1998). GPS sources have spectral turnovers around 1 GHz while CSS sources peak at frequencies below 1 GHz (O'Dea, 1998). Though there exists some overlap in the properties of peaked-spectrum radio sources, these spectral signatures are an effective means of distinguishing between them. See Keim et al. (2019) and references therein for a

Peaked Spectrum Sources

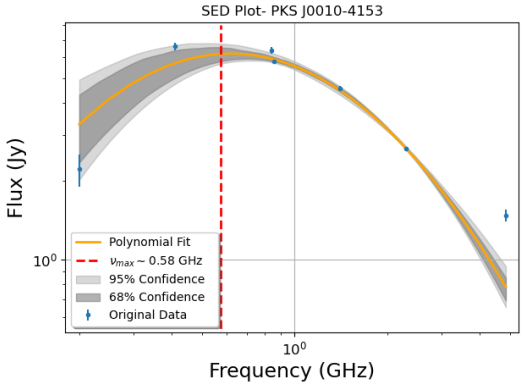

(a) PKS J0010-4153

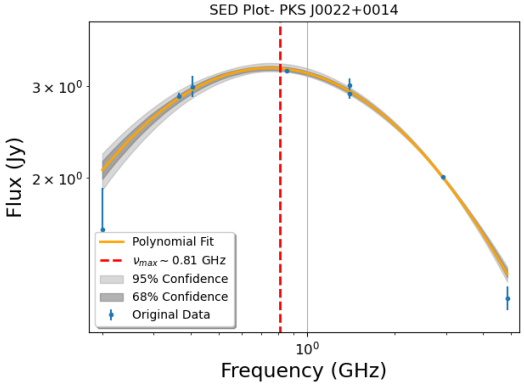

(b) PKS J0022+0014

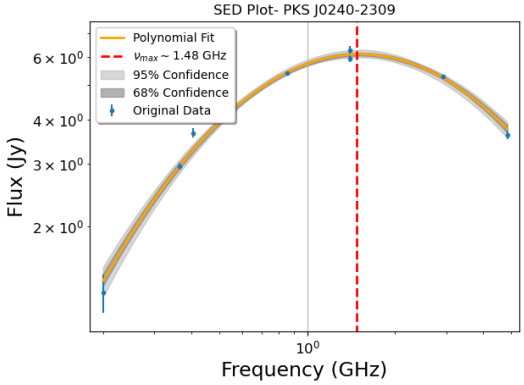

(c) PKS J0240-2309

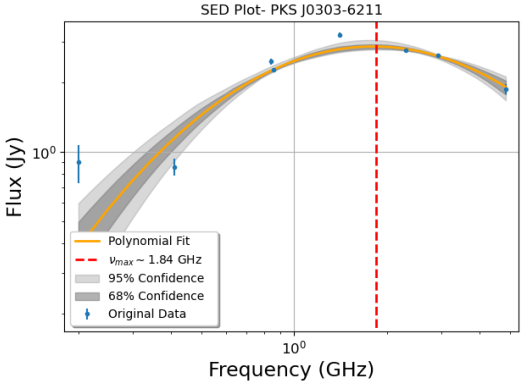

(d) PKS J0303-6211

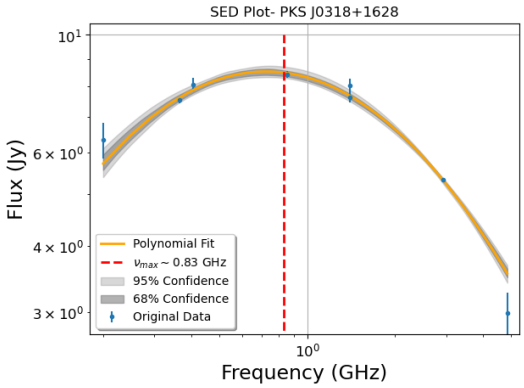

(e) PKS J0318+1628

Figure 2.3: Peaked spectral models of $\log(S_{\nu'})$ on the y-axis vs $\log(\nu')$ on the x-axis. The data points (in blue), with their measurement uncertainties, are overlaid with a second-order polynomial (orange). Overlaid on the fit are the Credible Intervals (CIs), which characterize the model uncertainty: the dark shading shows the 68% CI and the light shading shows the 95% CI.

detailed discussion on peaked-spectrum sources.

Our peaked-spectrum sources are shown in Figures 2.3 and 2.4. They are: PKS J0010-4153, PKS J0022+0014, PKS J0318+1628, PKS J0431+2037, PKS J0735-1735, and PKS J1939-6342, all known GPS sources. As well as PKS J0240-2309, PKS J0828-3731, and PKS J0303-6211.

Upturn Spectrum Sources

In our sample of calibrators, 15% of the sources exhibited an upturn in the spectrum where the flux density $\log(S_{\nu'})$ decreases to a minimum turnover frequency (ν_{min}), then increases with increasing frequency. These were also fit with a second-order polynomial (Equation 2.2) to capture the complexity of the data. The coefficients of the polynomial equation are listed in Table 2.2 for each source.

Sadler et al. (2006) observed a spectral class of sources whose radio emission was observed to fall at low frequencies but turn up and begin to rise around 5 GHz using multi-frequency data from the ATCA 20 GHz pilot survey, referring to them as 'Upturn Sources'. We also adopt this naming convention. This phenomenon is predicted to occur when the AGN radio emission transitions from being dominated by extended, optically thin lobes (steep spectrum) to being dominated by compact core emission (flat spectrum) (Tucci et al., 2008). The core emission is typically optically thick and beamed, and thus its contribution emerges and dominates at higher frequencies.

The sources that show such spectral behaviour are presented in Figure 2.5. They are: PKS J0210-5101, PKS J0423-0120, PKS J0538-4405, PKS J0609-1542 and PKS J1058+0133. All of them are classified as quasars (QSOs) in published literature.

Linear Spectrum Sources

In our sample of calibrators, 59% of the sources exhibit no distinct curvature in their spectrum, with the flux density and frequency variables having a predominantly linear relationship. This characteristic is indicative of sources dominated by a single, non-thermal process

like synchrotron emission modelled best by a simple power-law; $S_\nu \propto \nu^\alpha$ where S is the flux density, ν frequency, and α the spectral index (Thompson et al., 2001). Therefore, the equation used for the fit was a first-order polynomial, where the coefficient a_1 directly represents the spectral index α.

$$\log S(\nu') = a_0 + a_1 \log(\nu') \tag{2.3}$$

These sources typically fall into two fundamental spectral types defined by the sign and magnitude of the spectral index α:

1. Steep-Spectrum Sources ($\alpha < -0.5$) (de la Parra et al., 2024): Characterized by a flux density that generally reduces significantly with increasing frequency. Emission from these sources is predominantly dominated by optically thin emission from extended lobes Tucci et al. (2008). In our analysis, they are; PKS J0059+0006, PKS J0405-1308, PKS J0440-4333, PKS J0521+1638, PKS J0616-3456, PKS J0632+1022.

2. Flat-Spectrum Sources ($\alpha \geq -0.5$) de la Parra et al. (2024): Characterized by flux density that remains relatively stable or sometimes increases slightly with increasing frequency. Emission from these objects is dominated by the compact core, where optical depth effects (such as synchrotron self-absorption in the core) result in a flatter, less frequency-dependent spectrum Tucci et al. (2008). In our analysis, they are; PKS J0025-2602, PKS J0137+3309, PKS J0203-4349, PKS J0252-7104, PKS J0323+0534, PKS J0409-1757, PKS J0420-6223, PKS J0447-2203, PKS J0453-2807, PKS J0730-1141, PKS J0854+2006, PKS J0906-6829, PKS J1008+0730, and PKS J1051-2023.

The sources that show such spectral behaviour are shown in Figures 2.6, 2.7, 2.8 and 2.9.

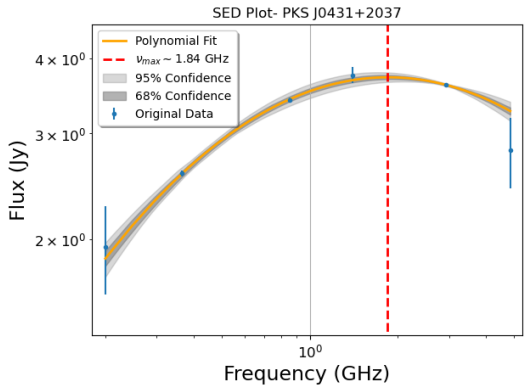

(a) PKS J0431+2037

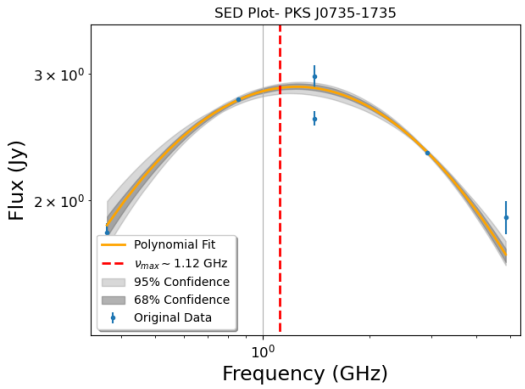

(b) PKS J0735-1735

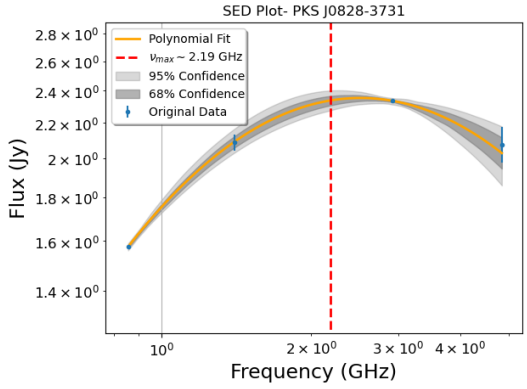

(c) PKS J0828-3731

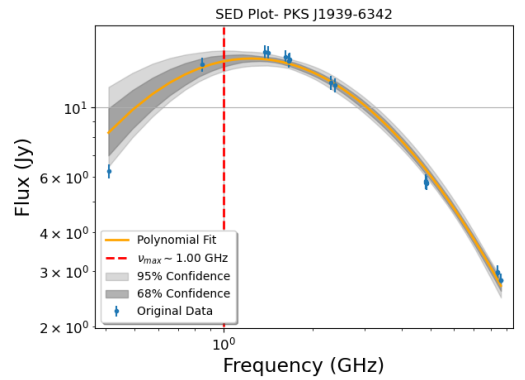

(d) PKS J1939-6342.

Figure 2.4: Peaked spectral models of $\log(S_{\nu'})$ on the y-axis vs $\log(\nu')$ on the x-axis. The data points (in blue), with their measurement uncertainties, are overlaid with a second-order polynomial (orange). Overlaid on the fit are the Credible Intervals (CIs), which characterize the model uncertainty: the dark shading shows the 68% CI and the light shading shows the 95% CI.

Upturn Spectrum Sources

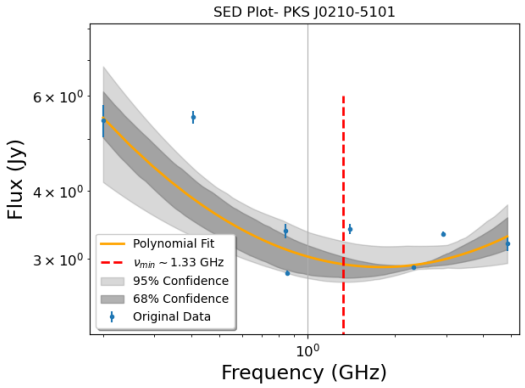

(a) PKS J0210-5101

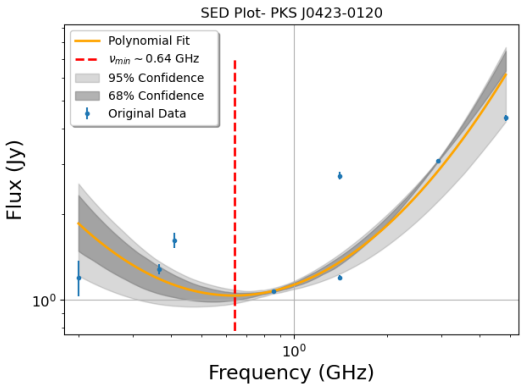

(b) PKS J0423-0120

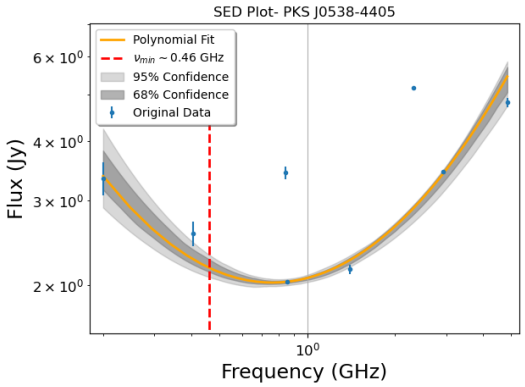

(c) PKS J0538-4405

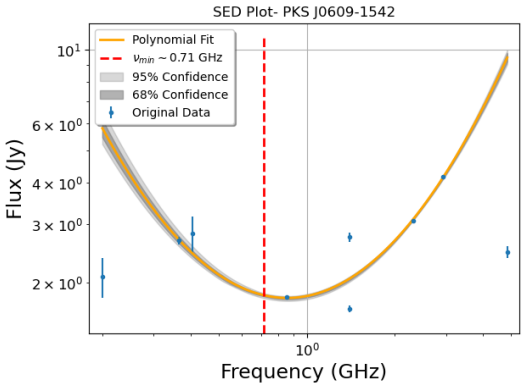

(d) PKS J0609-1542

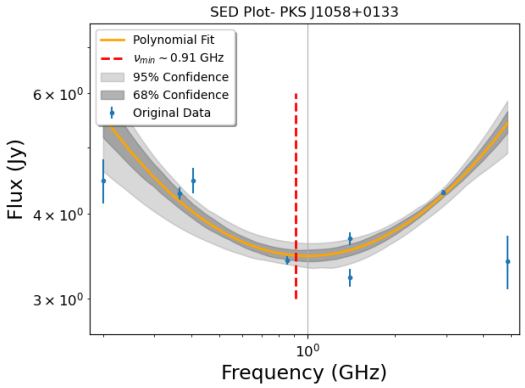

(e) PKS J1058+0133.

Figure 2.5: Upturn spectral models of $\log(S_{\nu'})$ on the y-axis vs $\log(\nu')$ on the x-axis. The data points (in blue), with their measurement uncertainties, are overlaid with a second-order polynomial (orange). Overlaid on the fit are the Credible Intervals (CIs), which characterize the model uncertainty: the dark shading shows the 68% CI and the light shading shows the 95% CI.

Linear Spectrum Sources

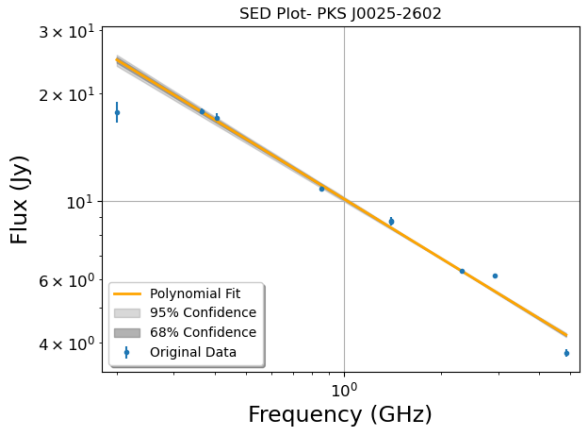

(a) PKS J0025-2602

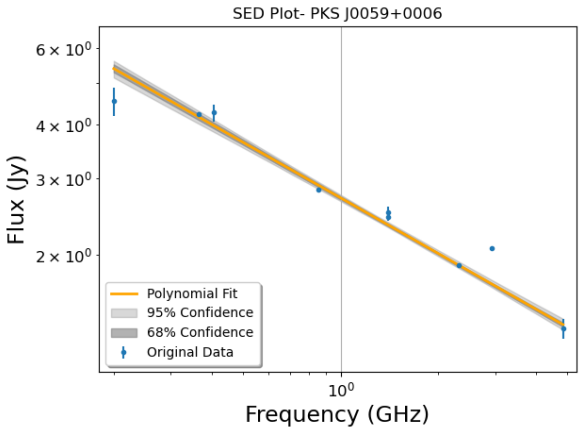

(b) PKS J0059+0006

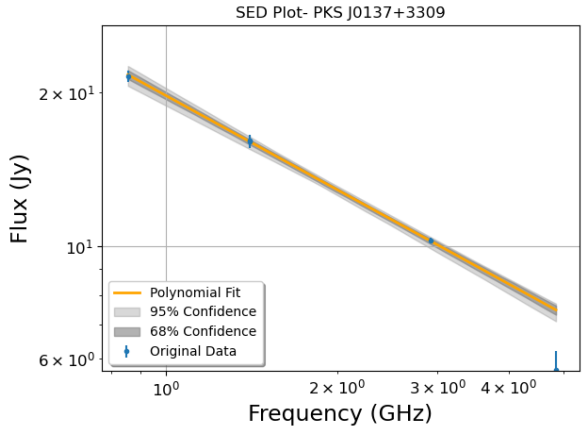

(c) PKS J0137+3309

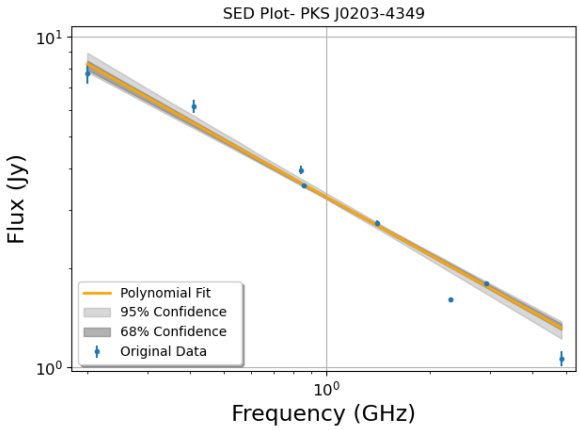

(d) PKS J0203-4349

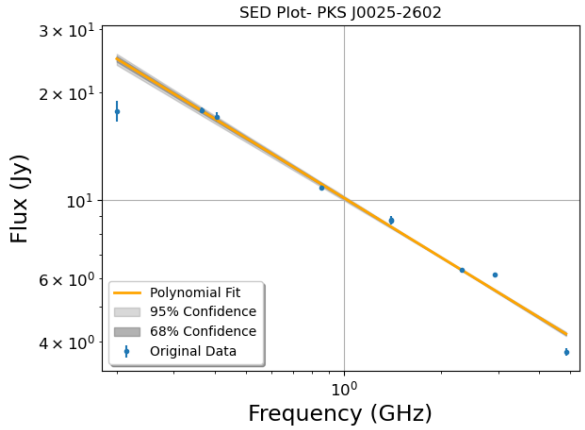

(e) PKS J0252-7104

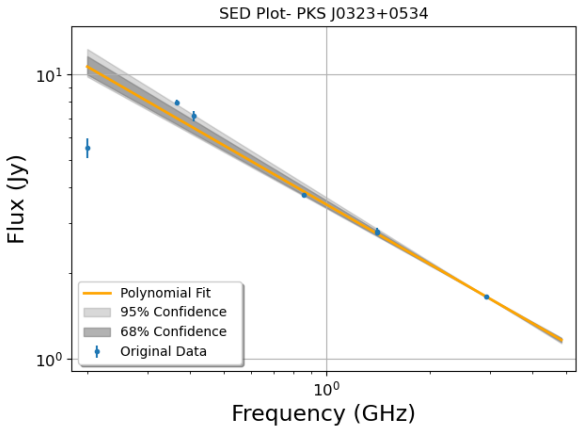

(f) PKS J0323+0534

Figure 2.6: Linear spectral models of $\log(S_{\nu'})$ on the y-axis vs $\log(\nu')$ on the x-axis. The data points (in blue), with their measurement uncertainties, are overlaid with a first-order polynomial (orange). Overlaid on the fit are the Credible Intervals (CIs), which characterize the model uncertainty: the dark shading shows the 68% CI and the light shading shows the 95% CI.

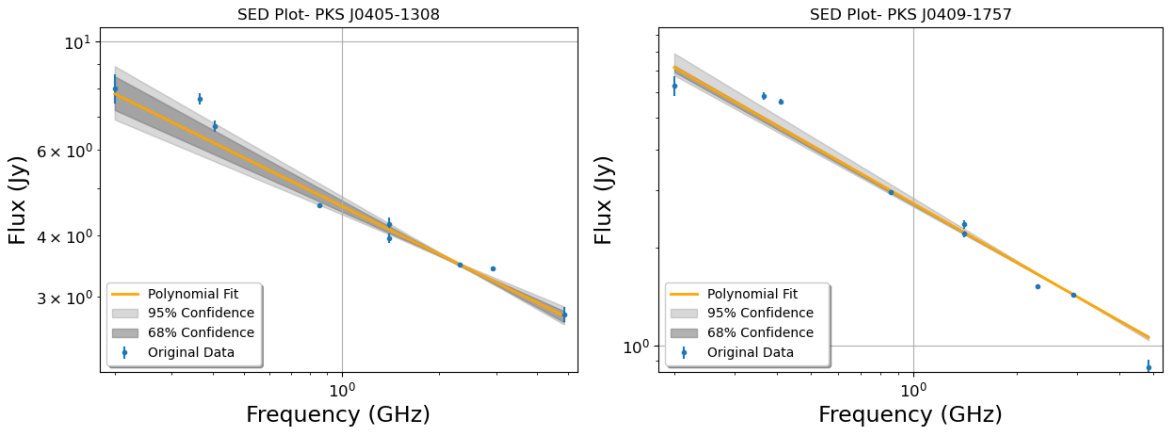

(a) PKS J0405-1308

(b) PKS J0409-1757

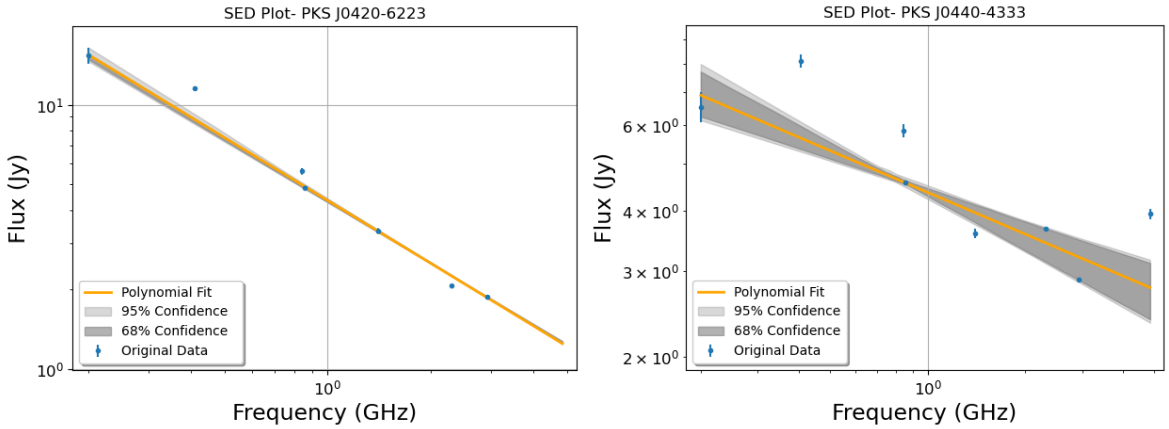

(c) PKS J0420-6223

(d) PKS J0440-4333

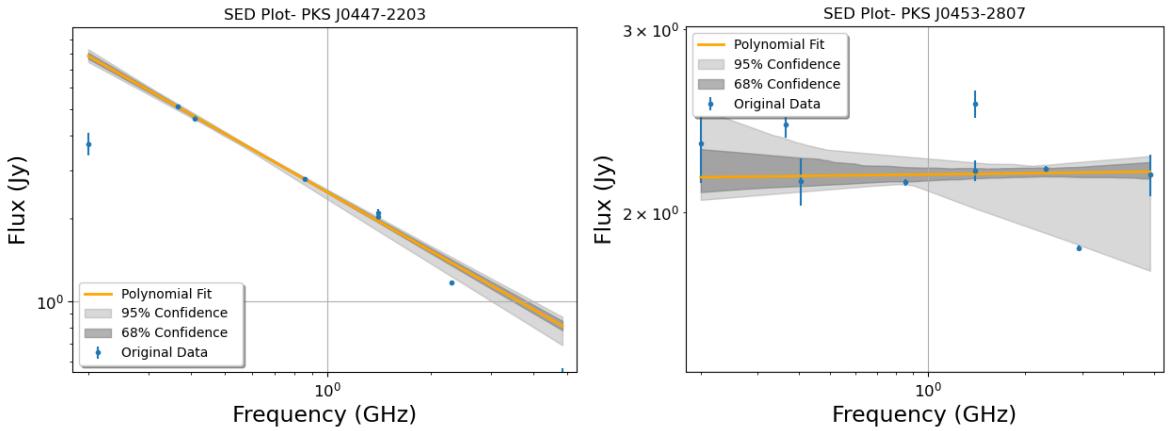

(e) PKS J0447-2203

(f) PKS J0453-2807

Figure 2.7: Linear spectral models of $\log(S_{\nu'})$ on the y-axis vs $\log(\nu')$ on the x-axis. The data points (in blue), with their measurement uncertainties, are overlaid with a first-order polynomial (orange). Overlaid on the fit are the Credible Intervals (CIs), which characterize the model uncertainty: the dark shading shows the 68% CI and the light shading shows the 95% CI.

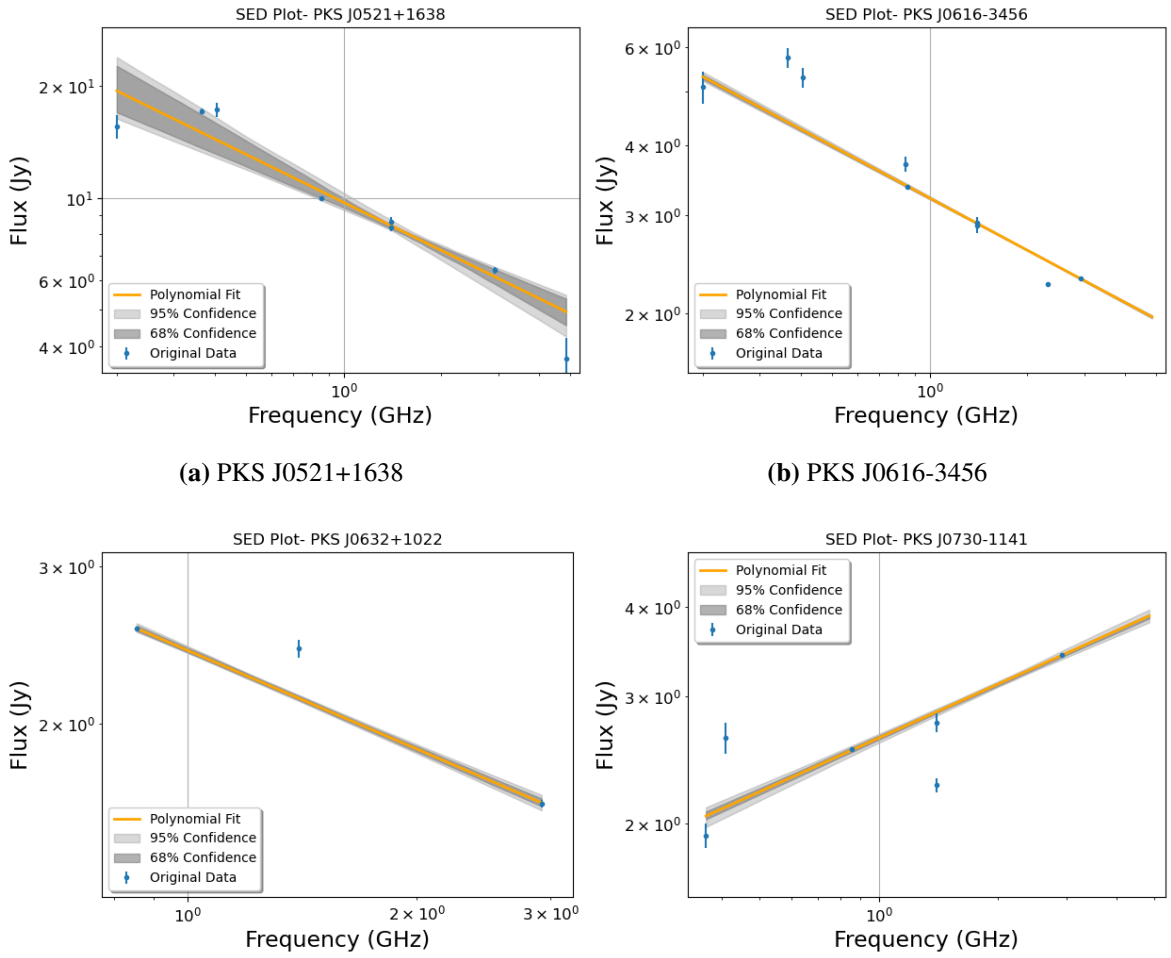

(a) PKS J0521+1638

(b) PKS J0616-3456

(c) PKS J0632+1022

(d) PKS J0730-1141

Figure 2.8: Linear spectral models of $\log(S_{\nu'})$ on the y-axis vs $\log(\nu')$ on the x-axis. The data points (in blue), with their measurement uncertainties, are overlaid with a first-order polynomial (orange). Overlaid on the fit are the Credible Intervals (CIs), which characterize the model uncertainty: the dark shading shows the 68% CI and the light shading shows the 95% CI.

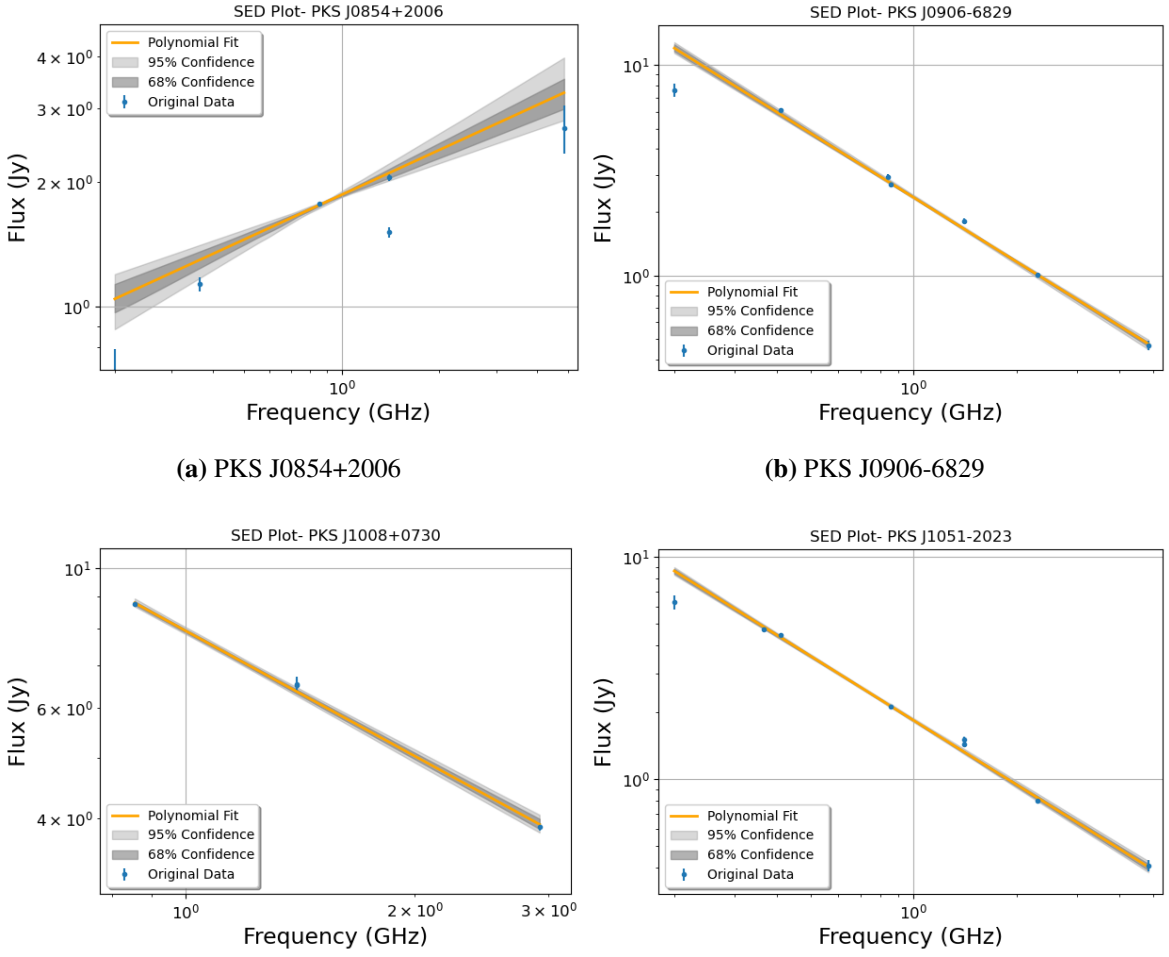

(a) PKS J0854+2006

(b) PKS J0906-6829

(c) PKS J1008+0730

(d) PKS J1051-2023

Figure 2.9: Linear spectral models of $\log(S_{\nu'})$ on the y-axis vs $\log(\nu')$ on the x-axis. The data points (in blue), with their measurement uncertainties, are overlaid with a first-order polynomial (orange). Overlaid on the fit are the Credible Intervals (CIs), which characterize the model uncertainty: the dark shading shows the 68% CI and the light shading shows the 95% CI.

Name	*RA* **h:m:s**	*Dec* **d:m:s**	a_0	a_1	a_2	α	z	**Type**
PKS J0010-4153	00:10:53	-41:53:11	1.82	0.07	-0.49	-0.95	1.13	RG
PKS J0022+0014	00:22:25	+00:14:56	1.18	-0.04	-0.26	-0.43	0.94	RG
PKS J0025-2602	00:25:49	-26:02:13	3.21	-0.56	***	-0.56	0.33	QSO
PKS J0059+0006	00:59:06	+00:06:52	1.68	-0.43	***	-0.41	0.72	QSO
PKS J0137+3309	01:37:41	+09:33.35	3.08	-0.61	***	-0.71	0.37	QSO
PKS J0203-4349	02:3:41	-43:49:51	2.11	-0.58	***	-0.74	0.45	RG
PKS J0210-5101	02:10:46	-51:01:02	1.07	-0.08	0.13	-0.21	1.00	QSO
PKS J0240-2309	02:40:08	-23:09:16	1.81	0.02	-0.36	-0.10	2.22	QSO
PKS J0252-7104	02:52:46	-71:04:35	3.17	-0.75	***	-0.81	0.56	RG
PKS J0303-6211	03:03:51	-62:11:26	1.05	-0.01	-0.41	0.20	1.35	QSO
PKS J0318+1628	03:18:58	+16:28:33	2.14	-0.07	-0.24	-0.32	0.91	QSO
PKS J0323+0534	03:23:20	+05:34:12	2.37	-0.70	***	-0.81	0.18	RG
PKS J0405-1308	04:05:34	-13:08:14	2.05	-0.33	***	-0.48	0.57	QSO
PKS J0409-1757	04:09:07	-17:57:10	1.97	-0.60	***	-0.72	0.72	RG
PKS J0420-6223	04:20:56	-62:23:39	2.73	-0.79	***	-1.02	0.81	RG
PKS J0423-0120	04:23:16	-01:20:33	0.11	0.04	0.35	0.34	0.92	QSO
PKS J0431+2037	04:31:04	+20:37:34	1.31	0.00	-0.14	0.31	0.22	RG
PKS J0440-4333	04:40:17	-43:33:09	1.93	-0.29	***	-0.24	2.86	QSO
PKS J0447-2203	04:47:37	-22:03:37	2.06	-0.71	***	-0.71	***	RG
PKS J0453-2807	04:53:15	-28:07:37	0.77	0.00	***	0.13	2.56	QSO
PKS J0521+1638	05:21:10	+16:38:22	2.96	-0.43	***	-0.54	0.76	QSO
PKS J0538-4405	05:38:50	-44:05:09	0.78	-0.28	0.29	0.05	0.89	QSO
PKS J0609-1542	06:09:41	-15:42:41	0.62	-0.24	0.47	0.08	0.32	QSO
PKS J0616-3456	06:16:36	-34:56:17	1.67	-0.31	***	-0.54	0.32	RG
PKS J0632+1022	06:32:15	+10:22:02	0.94	-0.37	***	-0.28	***	RG
PKS J0730-1141	07:30:19	-11:41:13	1.36	0.25	***	0.15	1.59	QSO
PKS J0735-1735	07:35:46	-17:35:49	1.05	0.06	-0.29	-0.36	***	RG

PKS J0828-3731	08:28:05	-37:31:06	0.85	0.10	-0.35	0.57	***	QSO
PKS J0854+2006	08:54:49	+06:20:31	1.18	0.36	***	0.41	0.31	QSO
PKS J0906-6829	09:06:52	-68:29:40	2.17	-0.66	***	-1.03	0.56	RG
PKS J1008+0730	10:08:00	+07:30:17	2.17	-0.66	***	-0.76	0.88	RG
PKS J1051-2023	10:51:32	-20:23:47	2.16	-0.96	***	0.72	1.12	RG
PKS J1058+0133	10:58:30	+01:33:59	1.24	-0.03	0.18	-0.16	0.89	QSO
PKS J1939-6342	19:39:25	-63:42:46	2.64	0.18	-0.44	1.57	0.19	QSO

Table 2.2: This table presents a summary of the known properties of our sample of calibrators and the coefficients of the polynomial fit to the data using SPECFIT. The columns are; Source Name, Right Ascension (J2000), Declination (J2000), Coefficients a(0), a(1) and a(2). Specfind spectral index (α), Redshift (z) and Source Types (broad classifications Radio Galaxy (RG) and Quasar (QSO)), all from published literature. **PKS J0137+3309** (3C48), **PKS J0521+1638** (3C138) and **PKS J1939-6342** are used as flux calibrators, while the other sources are used as phase calibrators. Additionally, **PKS J0137+3309** and **PKS J0521+1638** are also used as polarization calibrators (Perley and Butler, 2013).

2.3 Summary

In this chapter, we undertook our first objective to characterise a sample of southern sky calibrators observed by MeerKAT through detailed source modeling. The calibrator sample is summarised in Table 2.2. The table lists Source Names, Right Ascension (J2000), Declination (J2000), Specfind spectral index (α), Redshift (z), and broadly classified Source Types, (RG) and (QSO). The spectral models were created using the SPECFIT package and are presented in Section 2.2.2. Table 2.2 also lists the coefficients of the polynomial fit to the data, with the coefficient a_1 directly representing the spectral index α. Three distinct classes emerged from the analysis of the spectral models:

1. **Peaked Spectrum Sources**

   26% of the sample of calibrators exhibited a peaked spectrum. For these sources, the flux density $\log(S_{\nu'})$ increases up to a maximum turnover frequency ($\nu_{\max}$) in lower frequencies, then decreases with increasing frequency.

2. **Upturn Spectrum Sources**

   15% of the sample of calibrators exhibited an upturn 'bend' in the spectrum where the flux density $\log(S_{\nu'})$ decreases to a minimum turnover frequency ($\nu_{\min}$) in lower frequencies, then increases with increasing frequency.

3. **Linear Spectrum sources**

   59% of the sample of calibrators exhibited a linear spectrum where the flux density reduced, and less frequently, increased with increasing frequency. These sources typically fell into two fundamental spectral types as defined by de la Parra et al. (2024); Steep-Spectrum Sources ($\alpha < -0.5$) and Flat-Spectrum Sources ($\alpha \geq -0.5$).

SED modeling provides essential data for high-precision calibration with MeerKAT, aiming to significantly improve the reliability and accuracy of astronomical observations across multiple frequency bands. Furthermore, the classification of calibrators into distinct spectral types offers valuable insights into their underlying astrophysical properties, which can aid in distinguishing and separating classes of unknown radio objects in broader astronomical surveys.

Chapter 3

Radio Interferometry Data Reduction and Light Curve Extraction

As discussed in Section 1.1.2, radio visibilities are the measurements a pair of antennas makes while observing a science target source. Other than the visibilities, information about an observation, such as the number and condition of the antennas used, the science target, calibrators observed, frequency information, and more, is stored in a measurement set (MS). In this chapter, we detail the data reduction process undertaken to identify, remove corruptions, and recover the true sky brightness from measured visibilities in a MS. The process undertaken to produce the calibrator images in Sections 3.3.2, 3.4.5, and the radio light curve extraction detailed in Section 3.4.12 involved:

- First-Generation Calibration (1GC); We performed 1GC using the CARACal pipeline (Jozsa et al., 2020)[1], see Section 3.2.1.

- Second-generation calibration (2GC) and Light Curve Extraction; After 1GC, we performed 2GC and extracted radio light curves of the calibrator PKS J2152-2828 in the (U-band) and other sources within its field using the Madroon/PARROT pipeline (Smirnov et al., 2024)[2], see Section 3.4.

[1] https://github.com/caracal-pipeline/caracal

[2] https://github.com/ratt-ru/parrot-stew-recipes/tree/parrot1

Date of Observation	2022-09-30	2019-06-30
Start time (UTC)	18:07:35	00:45:15
End time (UTC)	23:51:51	02:41:05
No. of antennas	64	61
Dump rate (s)	4	8
Science Target Name	MACS J2140.2-2339	MACS J2140.2-2339
Calibrator Names	PKS J1939-6342 PKS J2152-2828 PKS J0521+1638	PKS J1939-6342 PKS J2152-2828
Frequency Band	U-band	L-band
File Size (GB)	1410	215

Table 3.1: Summary of the MeerKAT observations for the analysed data.

3.1 MeerKAT STV Observations

Table 3.1 provides a summary of the details of the MeerKAT observations analysed for the Short-Term Variability STV analysis. The two observations used the same flux/bandpass calibrator - PKS J1939-6342, and phase calibrator - PKS J2152-2828.

Due to the extensive computational demands and time constraints, the full data reduction workflow described in this chapter was performed only for a few calibrators from our main sample. For the STV analysis, two MeerKAT observations were chosen arbitrarily from the publicly available data in the MeerKAT archive. For the Long-Term Variability (LTV) analysis, data were obtained from the pre-processed products of the MeerKAT Science Data Processing (SDP) pipeline (detailed in Section 3.5).

3.2 First-Generation Calibration (1GC)

As discussed in Sections 1.1.3 and 1.3, calibration is a crucial step in radio astronomy, as it removes, insofar as possible, the effects of instrumental and atmospheric contributions from measured visibilities (Thompson et al., 2001). The ultimate goal of this process is to recover the true astronomical signal of the science target. Various calibration techniques exist and are often used together to achieve the best possible result (Sob, 2017). These techniques can be broadly classified into three categories, namely First (1GC), Second (2GC), and Third generation (3GC) calibration (Noordam and Smirnov, 2010). First-Generation Calibration (1GC) is generally the first step in the radio data reduction process (Noordam and Smirnov, 2010), addressing Direction Independent Effects (DIEs) using a known (prior or iteratively constructed) model of the sky.

A major part of 1GC is the excising of Radio Frequency Interference (RFI), which can introduce significant artifacts into images if not effectively handled (Thompson et al., 2017). A short discussion on RFI is outlined below.

Radio Frequency Interference (RFI)

RFI, also known as Electromagnetic Interference (EMI), is unwanted 'noise' picked up by radio telescopes that impacts the desired astronomical signal. RFI can be of natural origin, such as the Sun or lightning (as Jansky studied (Verschuur, 2007)), or of terrestrial origin. Human-generated interference poses an enormous challenge to the science of radio astronomy. With an increasingly technological society, man-made radio emissions are orders of magnitude greater than those of the astronomical sources of interest, as discussed by Sihlangu et al. (2022). Moreover, significant advancements have been made in radio astronomy instrumentation and technology, resulting in a far more sensitive generation of radio telescopes, such as the LOw Frequency ARray (LOFAR) [3] and MeerKAT (Sihlangu et al., 2022). This has been a double-edged sword, with the increased sensitivity facilitating the detection of fainter sources, but at the same time picking up ever fainter RFI contributions.

[3] https://lofar-uk.org/

Source		Frequency band [MHz]	
		Lower	Upper
UHF-TV		470	854
GSM			
	GSM-900 Uplink	890	915
	GSM-900 Downlink	935	960
	GSM-1800 Uplink	1710	1785
DME			
	Air-to-Ground	1025	1150
	Ground-to-Air	962	1024
		1151	1213
GPS			
	L1	1567.7	1582.7
	L2	1222.1	1232.1
	L3	1375.9	1385.9
	L4	1374.8	1384.8
	L5	1170.2	1182.2

Table 3.2: Frequency of known sources of RFI in the MeerKAT observing band.

The MeerKAT RFI environment is affected by groups of known man-made RFI contributors. These are Global Systems for Mobile Communication (GSM), Distance Measurement Equipment (DME), and UHF TV transmitters (U-TV) in the U-band. The L-band is affected by GSM, DME, Global Positioning System (GPS), and Global Navigation Satellite System (GNSS) bands (Sihlangu et al., 2022).

Various spectrum management policies have been set up to mitigate the effects of man-made RFI on radio telescope sites. For example, the Independent Communications Authority of South Africa (ICASA) states that the frequency bands between 970 MHz - 1080 MHz and 1300 MHz - 1500 MHz are reserved for radio astronomy purposes with the GPS L3 band sandwiched within. For example, Figure 3.1 shows the MeerKAT L-band with the black arrows indicating the less corrupted frequency bands referred to as 'clean' bands at 970 MHz - 1080 MHz and 1300 MHz - 1500 MHz with the GPS L3 band sandwiched between them.

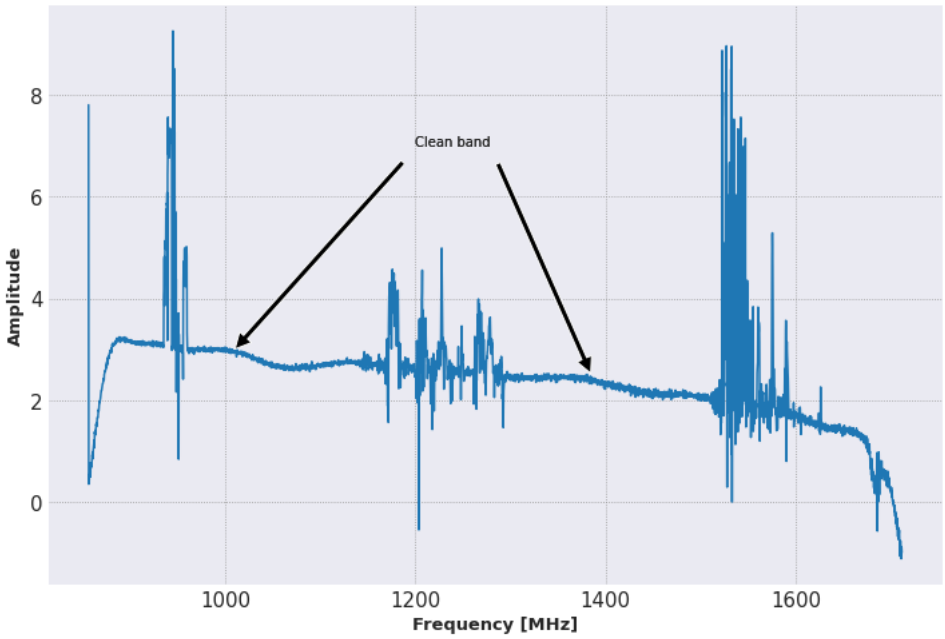

Figure 3.1: An example of the MeerKAT L-band Bandpass with some known RFI and the 'clean' band. (Sihlangu et al., 2022)

These RFI mitigation measures do not fully eliminate corruption of the desired signal; therefore, extra steps in the data reduction process are required to excise persistent RFI from data before any science can be conducted (see Section 1).

3.2.1 CARACal

We carried out 1GC using the CARACal pipeline. The CARACal pipeline was selected to conduct 1GC due to its flexibility, comprehensive suite of tools, and proven capability to achieve high-fidelity calibration for MeerKAT observations. The pipeline consists of Python/Stimela[4] scripts that reduce radio interferometry continuum and spectral line data (Jozsa et al., 2020). Stimela is a platform-independent radio interferometry scripting framework that allows users to execute tasks from various radio data reduction packages, for example, Common Astronomy Software Applications (CASA Team et al., 2022)[5] and MeqTrees[6] (Jozsa et al., 2020). Within CARACal are individual Stimela 'scripts' that correspond to a

[4]https://github.com/caracal-pipeline/stimela
[5]https://casa.nrao.edu/
[6]http://meqtrees.net/

step in the data reduction process. A user directs CARACal on what to do and which parameters to use in a sequence of blocks referred to as 'workers' to suit their data reduction needs via a Yet Another Markup Language (YAML)[7] configuration file. We set up CARACal to calibrate the U-band MeerKAT observation in Table 3.1 as follows:

1. **Flagging**

   (a) **An Overview**

   Flagging is the process of isolating and removing extremely corrupted data in the visibility domain that would eventually introduce significant errors in the image domain. A robust flagging strategy relies on a multifaceted approach that combines visual inspection with statistical, algorithmic, and a priori knowledge. For example, known problematic RFI frequency ranges can be flagged early on in the calibration process, as this interference often occupies specific bands as discussed in Section 3.2. CARACal enables the implementation of advanced RFI flagging strategies, such as Tricolour[8], which utilises SumThreshold and MAD interference detection algorithms, and AOFlagger [9] (Jozsa et al., 2020). These algorithms go beyond simple visual inspection to identify and excise corruptions. Furthermore, when manually inspecting the visibilities, data corruptions can also be identified by their deviation from the expected smooth, slowly varying behaviour of astronomical signals (Thompson et al., 2017). Highly scattered outliers and unexpected amplitude or phase variations are therefore key visual indicators of corrupted data (e.g, malfunctioning antennas and/or RFI).

   (b) **Implementation and Workflow**

   We directed CARACal to use its default flagging strategy; CASA's `flagdata` (Jozsa et al., 2020) to flag the auto-correlations, and spectral windows 544 MHz - 575 MHz, 1050 MHz - 1088 MHz at the beginning and end of the U-band. These areas are referred to as 'bandpass roll-off regions'. Receivers are engineered to

[7] YAML was defined as Yet Another Markup Language in the beginning and later it became 'YAML Ain't Markup language' - https://yaml.org/

[8] https://github.com/ratt-ru/tricolour

[9] https://gitlab.com/aroffringa/aoflagger

perform optimally within a specific frequency range, and at the lower and upper frequency limits of this optimal range, electronic components like amplifiers and filters become less efficient, leading to a rapid decrease in the signal-to-noise ratio (SNR) in these edge channels (Thompson et al., 2017). Flagging these regions is therefore essential to maintain data quality and prevent the introduction of systematic errors into the analysis.

In addition to flagging the natural receiver roll-off, we directed CARACal to use the Tricolour algorithm[10] (Hugo et al., 2022) to flag any persistent RFI corrupting the visibilities. This resulted in the gap around channel **3000** as can be seen in the bandpass solutions in Figure 3.6, where strong, narrow-band RFI was excised.

2. **Cross-calibration**

Cross-calibration is the process of using well-known calibrator properties to determine the net correction factors that mitigate observational errors, followed by the transfer and application of these solutions to the science target visibilities.

(a) **An Overview**

The crosscal worker in CARACal enables users to define a unique sequence of calibration and flagging steps to solve for instrumental and atmospheric corruptions. The calibration and flagging choices available within the worker include:

i. **K** - delay calibration with CASA `gaincal`.

This is the process through which the observed visibilities are corrected for effects caused by geometric and instrumental time delays that exist in interferometric systems (Thompson et al., 2017). Geometric time delays arise due to the physical positions of antennas, where radio signals from the same source arrive at different times at the antenna pairs (Kassaye, 2015). Instrumental time delays, however, are a separate effect caused by differences in the electronic path lengths of the receiving systems (Thompson et al., 2017). Both types of delays must be corrected to ensure accurate calibra-

[10] https://github.com/ratt-ru/tricolour

tion for although smaller delays do not necessarily result in a complete loss of coherence, they can affect the phase relationships between baselines and distort the synthesized beam, leading to image artifacts such as sidelobes or blurring in the final image (Thompson et al., 2017).

ii. **B** - bandpass calibration with CASA `bandpass`.
Bandpass calibration is done to solve for the frequency-dependent effects on the observed visibilities. This is necessary because, if done well, it facilitates spectral analysis. Any retained frequency-dependent amplitude errors would interfere with the detection of any weak spectral lines present, while any frequency-dependent phase errors can lead to positional offsets of spectral features, therefore, mimicking Doppler motions (CASA Documentation).

iii. **G** - gain amplitude and/or phase calibration with CASA `gaincal`.
Systematic, time-dependent complex gain errors are typically the most significant calibration issue, requiring resolution before any other calibration steps can be undertaken. Traditionally, this type of calibration encompasses a range of related effects, such as the relative amplitude and phase gains for each antenna and polarization, drifts in phase and amplitude within the electronics of each antenna, variations in amplitude response due to elevation changes (known as the gain curve), and the amplitude and phase effects caused by the troposphere (CASA Documentation).

iv. **A** - automatic flagging with CASA `flagdata` using the tfcrop algorithm. This is an inbuilt, automatic flagging strategy that a user can choose as part of the cross-calibration process within the CARACal pipeline (Jozsa et al., 2020). It can be executed at various stages of a calibration sequence (e.g., as step 4 in the KGBAKGB sequence).

v. **F** - gain amplitude and/or phase calibration with CASA `gaincal`, followed by bootstrapping of the flux scale from the primary calibrator with CASA `fluxscale` for the secondary calibrator only (Jozsa et al., 2020). The 'G' or 'T' solutions obtained by `gaincal` for calibrators for which the flux density was unknown and assumed to be 1 Jy are correct in a time- and antenna-

relative sense, but are mis-scaled by a factor equal to the inverse of the square root of the true flux density. This scaling can be corrected by enforcing the constraint that mean gain amplitudes determined from calibrators of unknown flux density should be the same as those determined from those with known flux densities (CASA Documentation).

(b) **Implementation and Workflow**

We began by filtering the data by selecting baselines $> 150\,\mathrm{m}$ to obtain a compact model of our calibrator and prevent contamination from diffuse emissions (Serra et al., 2023). A detailed sky model of the calibrator field was generated by Crystalball[11]. Crystalball is a model prediction tool that creates detailed sky models by predicting visibilities from lists of WSClean components for the calibrator fields. Unlike traditional point-source models, which are often inadequate for wide-field interferometers like MeerKAT and can introduce significant errors by ignoring faint off-axis sources, Crystalball utilizes a comprehensive multi-component model to ensure the highest possible calibration accuracy.

We then directed CARACal to solve for delay, complex-gain, and complex-bandpass corrections in the order **KGBAKGB** to get the measured primary calibrator (PKS J1939-6342) visibilities as close as possible to its model visibilities. This order was chosen to ensure that more stable and fundamental corrections are applied first, providing a robust foundation for subsequent, more sensitive adjustments. Following the primary calibration step, the resulting final bandpass solutions (**B**) were applied to the secondary calibrator (PKS J2152-2828), with its delay and complex-gain corrections solved in the order **KGAKF**. In the step (**F**), CASA's `fluxscale` task was used to bootstrap the absolute flux scale from the primary calibrator onto the secondary calibrator to scale the secondary gain solutions. The initial solution intervals were set to infinite (inf) to maximize signal-to-noise ratio (SNR), while the subsequent stages used a 60 s solution interval to track rapid time variations.

[11] https://github.com/caracal-pipeline/crystalball

3. **Diagnostic Plots**

A crucial part of the 1GC data reduction process is the plotting and inspection of the calibrated visibilities (Corrected_Data) to evaluate the calibration's performance. We carried out the plotting using the inspection worker in CARACal (ShadeMS[12]). The plots produced are detailed below and were visualized using radiopadre[13], a Jupyter notebook framework for quick and easy visualization of the data products and pipelines.

(a) **Delay Solutions**

We inspected the final delay solutions for all antennas throughout the duration of observation for both the primary and secondary calibrators. As the frequency response should be coherent over the desired bandwidth, a phase difference ($\Delta\phi$) over the bandwidth ($\Delta\nu$) that is ≥ 1 radian would produce a recognizable loss of coherence across the band (Thompson et al., 2017). This relationship is defined by the phase difference equation, where ΔT_g is the geometric time delay and ΔT_r is the instrumental time delay (Kassaye, 2015):

$$\Delta\phi = 2\pi\Delta\nu(\Delta T_g - \Delta T_r) \tag{3.1}$$

Therefore, to maintain coherence across the U-band (816 MHz bandwidth), the delay between signals must be less than ≈ 0.2 ns. The residual delay of both calibrators fell into a range of $\approx \pm 0.3$ ns as seen in Figures 3.2 and 3.3, which show the delay solutions vs antennas for PKS J1939-6342 and PKS J2152-2828, respectively. This value is comparable to the threshold value ≈ 0.2 ns calculated in Equation 3.1. This indicates that while the calibration was effective in significantly reducing the initial, uncalibrated delays, there remained small, uncorrected residual delays that could introduce minor image artifacts.

(b) **Plots of the Ratio of Corrected to Model Data**

Figure 3.4 displays the plot of the ratio of Corrected to Model Data of the primary calibrator (PKS J1939-6342), coloured by scan number (3). During the

[12] https://github.com/ratt-ru/shadeMS
[13] https://github.com/ratt-ru/radiopadre

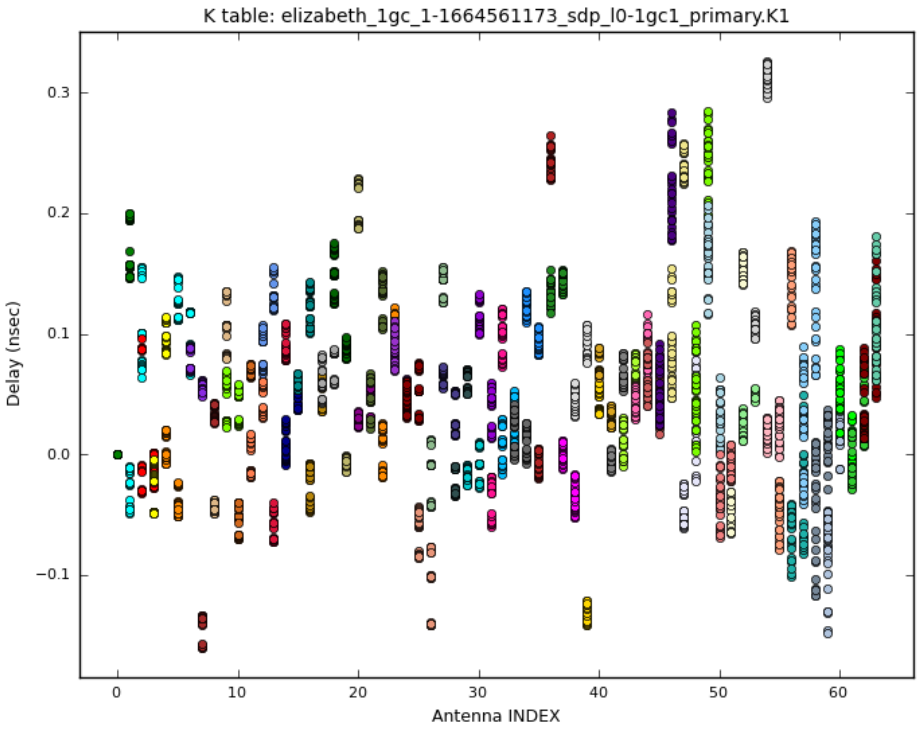

Figure 3.2: Delay Solutions vs Antennas for PKS J1939-6342. The horizontal axis represents the antenna index, where the antenna number corresponds to the antenna index + 1. For example, Antenna INDEX = 0 is equivalent to antenna 1 also known as m000, and so on.

observation of a science target, the calibrators are observed intermittently over the duration of the observation; we refer to these calibrator observations henceforth as scans. The primary calibrator had 3 scans, while the secondary had 11 scans.

For a well-calibrated source, the calibrated data would ideally be equal to the model, giving a ratio of $1+0j$ where the real component is 1, and the imaginary component is 0 (Thompson et al., 2017). In Figure 3.4, the residuals cluster tightly around $1,0$ and the three scans evenly contribute to the cluster. This indicates that 1GC of the primary calibrator was successful, with the time-dependent systematic gain and phase effects effectively removed, resulting in a unity residual amplitude (Real ≈ 1.0 – x axis) and minimal residual phase er-

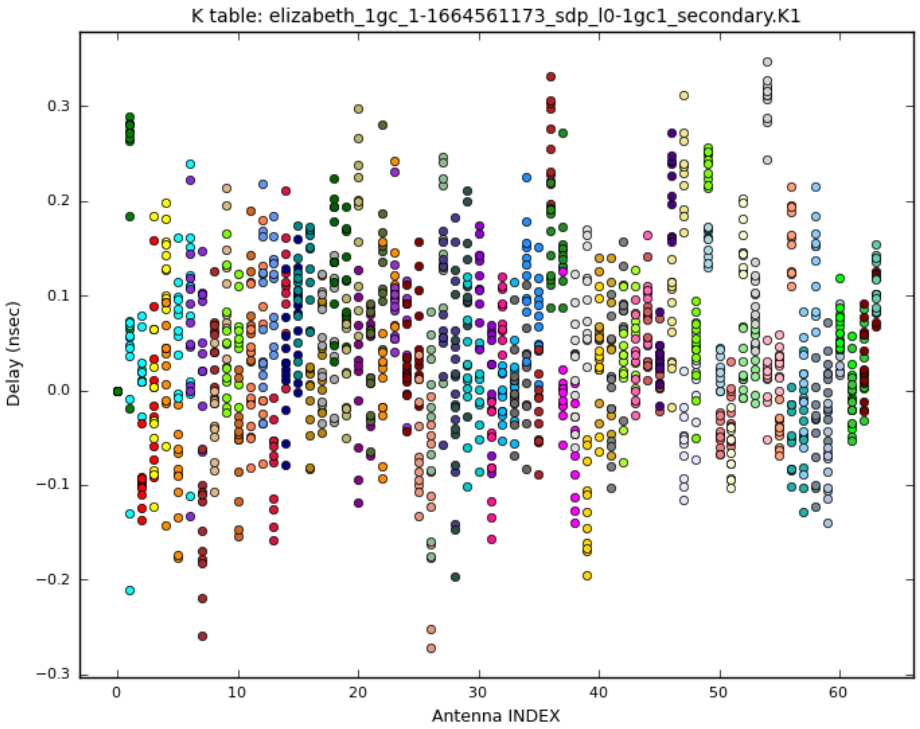

Figure 3.3: Delay Solutions vs Antennas for PKS J2152-2828. The horizontal axis represents the antenna index, where the antenna number corresponds to the antenna index + 1. For example, Antenna INDEX = 0 is equivalent to antenna 1, also known as m000.

ror (Imaginary ≈ 0.0 – y axis). Figure 3.5 shows the secondary calibrator's (PKS J2152-2828) ratio of corrected to model data, coloured by scan number (11). The plot shows a clustered distribution around $\approx 5,0$ with all scans evenly distributed. This confirms that 1GC was effective overall in reducing time-dependent systematic effects for the secondary calibrator. However, the increased scatter and deviation from unity amplitude indicate that the inherent uncertainty in its assumed sky model and lower flux density (resulting in lower SNR) introduced larger complex residual errors that 1GC was unable to remove fully. Such plots are highly useful in visually inspecting whether the temporal gain corrections were successful, as any clustering of points from one scan would indicate a systematic error or unflagged RFI that occurred during that specific scan.

(c) **Bandpass Amplitude and Phase Solutions**

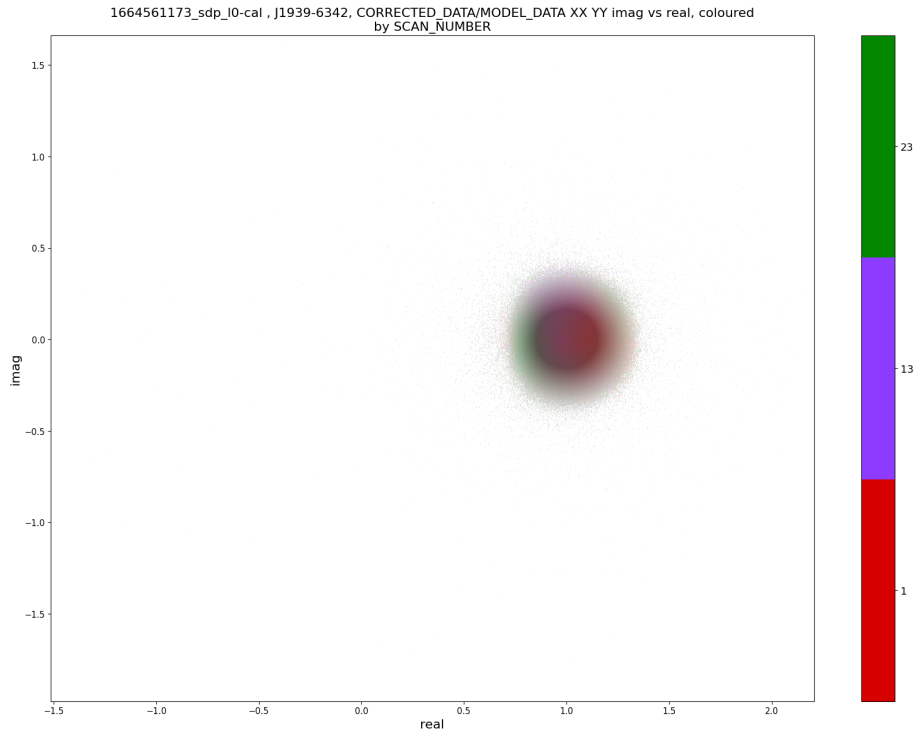

Figure 3.4: Plot of the Ratio of Corrected to Model Data (XX and YY polarization) of PKS J1939-6342 coloured by scan number (3 scans).

In Figure 3.6, we plotted the final bandpass amplitude (top) and phase (bottom) solutions vs 4K channels for PKS J1939-6342 (U-band). The different colours show the various antennas used in this observation. As discussed previously, for a well-characterised calibrator, the derived complex gain solutions should be close to unity in amplitude and near zero in phase after calibration. In practice, we expect the amplitudes to scatter around 1.0 ± 0.2 (i.e., within $\sim 20\%$ of unity) (Thompson et al., 2017). This spread arises from realistic contributions such as thermal noise, small receiver gain drifts, atmospheric opacity variations, and occasional pointing errors.

The phase solutions are expected to remain within $\pm 20^{\circ}$ of zero (Thompson et al., 2017). Residual fluctuations at this level are introduced by atmospheric or ionospheric path-length variations, instrumental instabilities (e.g., clocks, cables), and finite signal-to-noise limitations. If the phases remain confined to this range, it indicates that the calibrator is compact and unresolved, and that the array

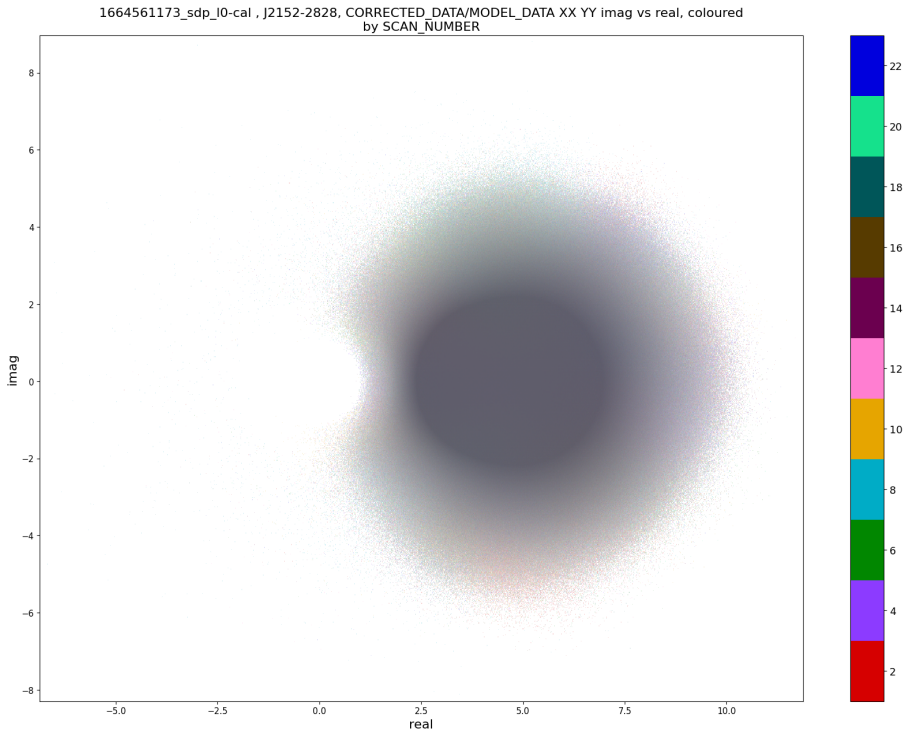

Figure 3.5: Plot of the Ratio of Corrected to Model Data (XX and YY polarization) of PKS J2152-2828 coloured by scan number (11 scans).

is operating in a stable regime. Larger excursions in either amplitude or phase typically signal unmodeled structure, poor weather conditions, or data corruption (Thompson et al., 2001). The final bandpass amplitude and phase solutions in Figure 3.6 fell within the expected range, demonstrating that the calibration steps were effective in correcting for major instrumental and atmospheric effects.

The 1GC process ensures initial data calibration, serving as an essential stepping stone for high-fidelity astronomical imaging and any other subsequent calibration processes. A similar process was followed for the L-band MeerKAT observation in Table 3.1. After 1GC, we split the initial calbrator MS into individual primary and secondary MS's using CASA's `split` task. This was done to perform the subsequent imaging, 2GC, and light curve extraction individually for each calibrator field, to accurately isolate and analyse their STV.

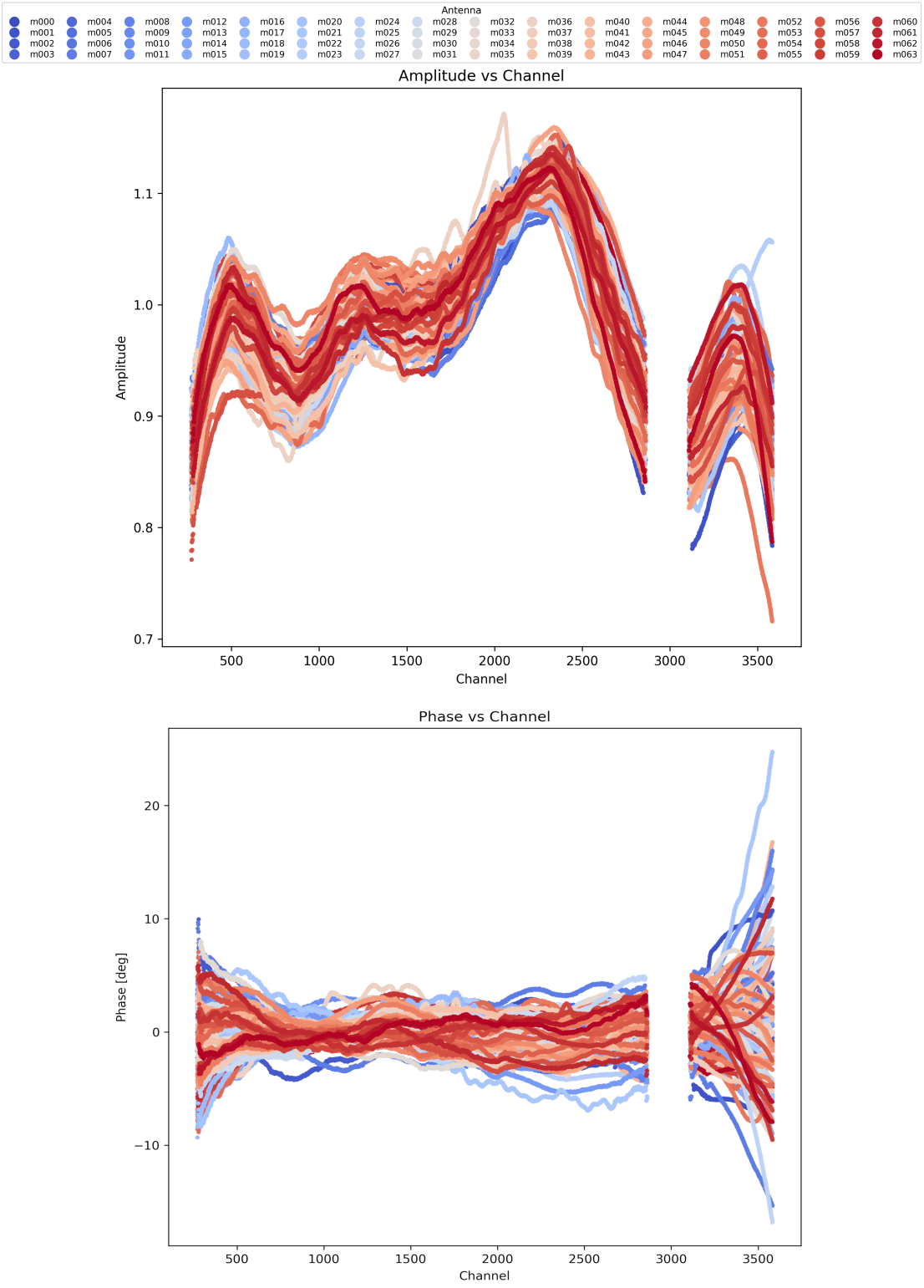

Figure 3.6: Final Bandpass Amplitude (top) and Phase (bottom) Solutions vs 4K channels for PKS J1939-6342 (U-band). The different colours show individual antennas. The amplitude varies around 1.0 ± 0.2, and the phase varies within $\pm 20^{\circ}$. The region around channel 3000 was flagged as explained in Section 1.

3.3 Imaging

As discussed in Section 1.1.2, a Fourier transform of the true sky brightness intensity is the visibility function $\mathrm{V}(u,v)$ that we measure. This is an ideal case. In practice, the $u-v$ plane is sampled unevenly and incompletely as a consequence of the finite number of antennas in an array and the earth-sky geometry. The sampling function represents the unique array configuration; $\mathrm{S}(u,v)$, a collection of points in the $u-v$ plane where the visibility measurements have been made.

$$\mathrm{S}(u,v) = \sum_{k=1}^{M} \Delta(u-u_k, v-v_k) \tag{3.2}$$

The sampled visibility can be represented as $(\mathrm{V}(u,v)\mathrm{S}(u,v))$. The Fourier transform $(\mathfrak{F})$ of this sampled visibility is the dirty image $\mathrm{I}^{\mathrm{D}}(l,m)$ as shown in Equation 3.3. The dirty image is the result of the convolution of the true sky brightness with the dirty beam (Equation 3.5). It is a distorted representation of the sky, not simply an incomplete one, because it includes artifacts and distortions caused by the incomplete sampling of the $u-v$ plane.

$$\mathfrak{F}(\mathrm{V}(u,v)\mathrm{S}(u,v)) \sim \mathrm{I}^{\mathrm{D}}(l,m) \tag{3.3}$$

The Fourier transform of the sampling pattern in the image domain is referred to as the dirty beam or point spread function (PSF) 3.4

$$\mathfrak{F}(\mathrm{S}(u,v)) \sim \mathrm{PSF}(l,m) \tag{3.4}$$

The dirty image is the result of the convolution of the true sky brightness with the dirty beam.

$$\mathrm{I}(l,m) * \mathrm{PSF}(l,m) \sim \mathrm{I}^{\mathrm{D}}(l,m) \tag{3.5}$$

The many zeros present in the typical sampling pattern show why the simple inversion approach to deconvolution cannot be used. Many approaches exist for the inversion of the convolution, most notably the CLEAN algorithm, as discussed in the next section.

3.3.1 CLEAN Algorithm

The CLEAN algorithm forms the basis for different deconvolution algorithms. It involves an iterative process of identifying the strength and location of the highest peak present in a dirty image, storing this information in a model, and then subtracting a scaled version of the PSF at this location to remove its effects until a previously set stopping criteria are met. This threshold is often three times the standard deviation of the expected noise. There are variations of this algorithm; the less complex CLEAN algorithm described by Högbom (1974) is discussed below.

Högbom CLEAN

This algorithm finds a solution to the convolution equation by representing the radio source as several point sources in an otherwise empty sky. The 'cleaning' process is then carried out as follows:

- The location with the highest peak flux is identified. The location and amplitude are recorded in a separate components list.
- A scaled version of the PSF is subtracted from this location to remove the effects of the PSF. The 'CLEAN' components list is updated and a residual image output is generated.
- The first two steps are repeated until the highest peak in the residual image is below the threshold set. The final output is a residual image cleaned down to noise and a 'CLEAN' components list that contains the location and amplitudes of the point sources.
- The final restored image is then created by making a model of the sky brightness from the components list, convolving this with a clean beam, and then adding the residual noise map.

3.3.2 WSClean

We used the imaging software WSClean (Offringa et al., 2014) to produce radio images throughout our data reduction process. The imaging parameters are input in a short script format that details the user's imaging preferences. We used the particular script below to create the first image after 1GC for PKS J1939-6342's U-band calibrator field.

```
wsclean -name pks1939img1 -data-column DATA -channels-out 6 -weight
briggs 0 - size 8000 8000 -scale 1.6asec -niter 150000 -nmiter 10
-auto-threshold 3.0 - mgain 0.8 -join-channels -fit-spectral-pol 4
-save-source-list use wgridder -temp-dir /home/waweru/J2140/temp
-log-time /home/waweru/J2140/Imaging
```

The input parameters chosen are detailed below:

- **data-column** - as the name implies, this is the column in the MS that will be imaged. By default, this is DATA, where the 1GC calibrated data is stored but can change with further analysis or user needs.
- **weight** - this indicates the image weighting scheme. The sampling function $S(u,v)$ can be modified by a weighting function $W(u,v)$ that gives different weights to the different baselines to achieve high resolution and/or high point source sensitivity. We use the Briggs weighting scheme that maximizes point source sensitivity while attaining a good resolution.
- **size** - this is the size of the image in pixels. An image too large would take a very long time to process while an image too small could leave out important information such as strong confusing sources in the field. The rule of thumb is to create an image that is $3\times$ HPBW (Thompson et al., 2017). Out to $\sim 3\times$HPBW, the primary beam response is still non-zero (down to a few percent), so bright sources outside the nominal field center can contribute sidelobes and artifacts in the deconvolution if not included in the image (Thompson et al., 2017). Imaging to this level allows us to minimize the impact

of bright sources in the sidelobes of the primary beam. For MeerKAT, the primary beam is around 1° hence we created a 3° image size.

- **scale** - This specifies the pixel size in the output image. We chose a value of $1.5''$, which is determined by how many pixels are needed to accurately characterize the synthesized beam. A minimum of three points is considered essential to coarsely define the shape of a smoothly varying feature like a Gaussian synthesized beam, allowing for a basic approximation of its peak and spread (Thompson et al., 2001). However, we used a finer sampling by dividing the expected synthesized beam's half-power beam width (HPBW) by a factor of 5 to ensure accurate imaging and deconvolution.

- **niter** - This is the maximum number of iterations the deconvolution algorithm will perform. This allows us to control how far the algorithm goes when subtracting model components from the dirty image. We set the maximum number of clean iterations to 150,000. This value is a *conservative upper bound* rather than the primary stopping criterion. The deconvolution is effectively halted by noise-based thresholds and gain settings, with the hard cap serving only to prevent over-cleaning of noise and excessive runtime in the presence of residual artefacts (Offringa and Smirnov, 2017).

- **nmiter** - This is the number of major iterations in the deconvolution process, i.e., the number of times the sky model is updated and subtracted from the visibilities before a new residual image is computed. We set the maximum number of major iterations to 10, which provides a balance between accuracy and computational efficiency.

- **join-channels** - This parameter joins the deconvolution for all channels into a single deconvolution to improve the signal-to-noise ratio.

- **auto-threshold** - This sets an automatic threshold when the cleaning process should stop. This is usually set as a multiple of the image noise level.

- **mgain** - This sets the major loop gain, which determines the fraction of the peak intensity that is subtracted at each major iteration. During the cleaning process, the major loops, controlled by mgain, focus on the brightest sources in the image. Each major loop iteration involves identifying the brightest remaining component in the

dirty image and subtracting a fraction of its flux. While major loops address the overall image structure by iteratively removing the brightest components, minor loops can be used within each major loop iteration to refine the model of an individual source, allowing for a more accurate representation of complex source structures.

- **channels-out** - This splits the 4k channels into (6) sub-bands for imaging.
- **fit-spectral-pol**- This fits a (4th order) polynomial to the spectrum of each clean component, modeling the spectral index across each sub-band.

1GC IMAGES

Once images are produced, it is a good practice to extract radio parameters to check whether they agree with what is previously known. If the calibrator parameters are not acceptable, the calibration results will be rejected. Absolute amplitude accuracy can be achieved by either an antenna-based reference (noise diode) or by using a celestial flux calibrator. One commonly used is PKS J1939-6342, an established, well-studied (see Section 2.1.1), absolute flux calibrator (Reynolds, 1994). Its flux model given by Reynolds (1994) is:

$$\log(\mathrm{S}) = -30.7667 + 26.4908 \times \log(\nu) - 7.0977 \times \log(\nu)^2 + 0.605334 \times \log(\nu)^3 \quad (3.6)$$

where S is the flux density in Jy and ν is the frequency in MHz. Using the equation above, the expected flux for the U-band (centered at 815.9 MHz) and L-band image (centered at 1283.9 MHz) is 13.96 Jy and 15.09 Jy respectively.

1GC image of PKS J1939-6342

The U-band image produced after 1GC of the flux calibrator PKS J1939-6342 is shown in Figure 3.7a. Figure 3.7b gives the residual image. We created an on-source region (centered on the calibrator) and performed a 2D Gaussian fit to extract the calibrator parameters. The analysis revealed a compact radio source at *RA* 19:39:25.03, *Dec* -63:42:45.62 with a peak intensity of 13.24 ± 0.03 Jy/beam and an integrated flux of 13.20 ± 0.05 Jy. The extracted angular size of the source was $13.67 \pm 0.03''$ along its major axis and $11.89 \pm 0.02''$ along its minor axis.

The measured fluxes were slightly lower than the predicted flux using Equation 3.6. Using the model that we derived in Section 2.2 and the values for PKS J1939-6342 presented in Table 2.2, we calculated the expected flux to be 13.24 Jy and 14.30 Jy in the U- and L-band, respectively. These values are in agreement with our measured fluxes.

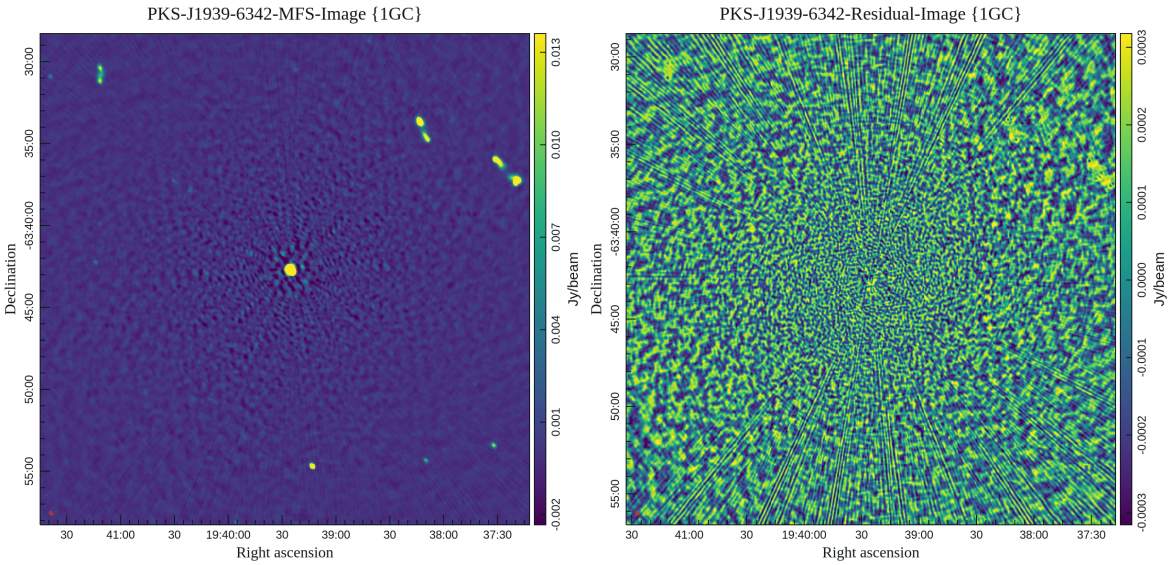

(a) PKS J1939-6342 **(b)** PKS J1939-6342 residual

Figure 3.7: Multi-frequency Synthesis (MFS) and Residual Images of the flux calibrator PKS J1939-6342 after 1GC in the U-band. From Figure 3.7a, we notice that the bright calibrator's PSF was not well-subtracted, thus faint radial lines are seen extending outward from the source to the rest of the field. The residual image in Figure 3.7b shows that no over-cleaning has occurred (no negative holes).

1GC image of PKS J2152-2828

The U-band image produced after 1GC of the phase calibrator PKS J2152-2828 is shown in Figure 3.8a. Figure 3.8b shows the residual image. Similar to the flux calibrator, we performed a 2D Gaussian fit on the on-source region to extract the calibrator parameters. The analysis revealed a compact radio source at *RA* 21:52:03.74, *Dec* -28:28:28.19 with a peak intensity of 4.24 Jy/beam and an integrated flux of 4.26 Jy. The extracted angular size of the source is 12.53″ along its major axis and 9.64″ along its minor axis.

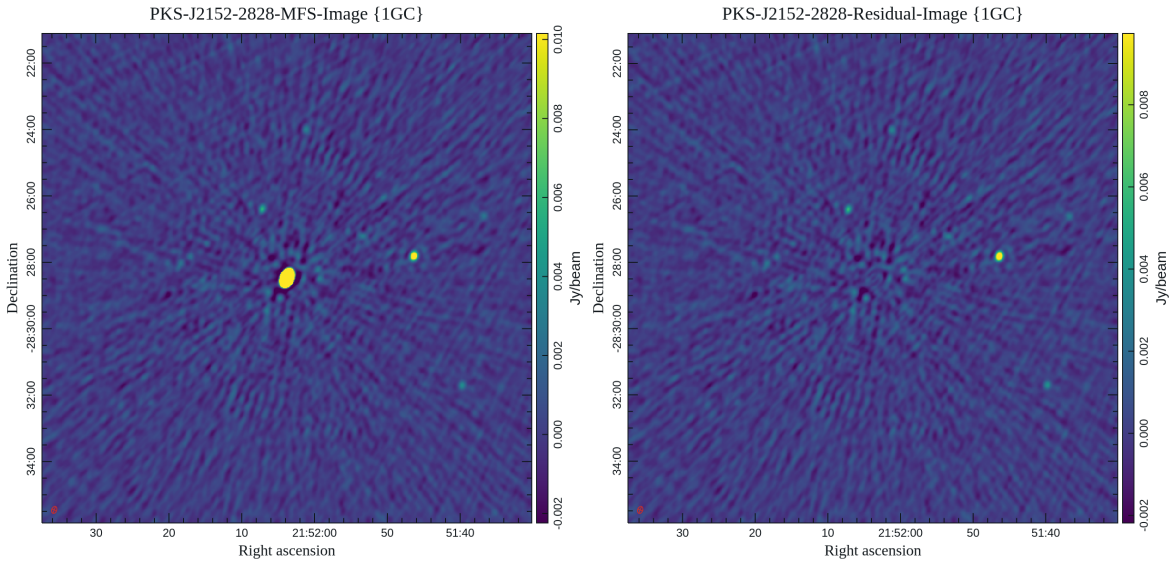

(a) U-band image PKS J2152-2828

(b) U-band PKS J2152-2828 residual

Figure 3.8: MFS and Residual Images of the phase calibrator PKS J2152-2828 after 1GC in the U-band. In Figure 3.8a, we notice that the PSF from the bright phase calibrator centered in the image is still bright in intensity and extends outward, overwhelming the faint sources close to the calibrator. The residual image in Figure 3.8b confirmed that no over-cleaning occurred (no negative holes).

3.4 Second-Generation Calibration (2GC) & Light Curve Extraction

The main goal of the second phase of our data reduction process was the extraction of radio light curves to investigate STV. Overall, this was achieved by creating the deepest possible (time-averaged) sky model for each calibrator field, subtracting the sky model from the observed visibilities, followed by plotting the residuals over the duration of the observation (light curve) to analyse the temporal variability for each source. It should be noted that even though our variability analysis was focused on calibrators, the need to discriminate between intrinsic variation, scintillation, and instrumental effects warranted the inclusion of other sources in the field in the analysis (see Step 3.4.12).

We used the Madroon[14] pipeline to carry out this process. The pipeline allows the use of different radio data reduction software in one environment, a consequence of the flexible workflow management framework expressed in human-readable format and easily modified YaML recipes - Stimela2 (Smirnov et al., 2024). The detailed steps and parameters used are summarised as follows:

3.4.1 Step 1: Initial Imaging - WSClean

As discussed in Section 3.3.2, we use WSClean (Offringa et al., 2014) to image our radio visibility data. This also applies within the pipeline. The specific parameters unique to the user's imaging needs can be modified as required in the YaML recipes. Imaging is done iteratively so that the user can probe the results of each data reduction step. They are delineated by numbered suffixes, the first being (img-1). We began with initial imaging after first-generation calibration. The resulting images were similar to those in Section 3.3.2.

3.4.2 Step 2: Masking - Breizorro

A mask is a binary map assigning non-zero values to every location containing a source and zero elsewhere. This was generated using the Breizorro[15] masking tool after every imaging step with a decreasing threshold value. The default initial threshold was set to 15σ. This was chosen as a conservative threshold to build a highly reliable sky model from the brightest sources while minimizing the risk of incorporating uncorrected calibration errors or artifacts into the foundation of the iterative self-calibration process. As the image quality improves as a result of self-calibration, we progressively masked and cleaned fainter sources. This mask was then used in subsequent imaging steps to constrain the cleaning process.

[14] https://github.com/ratt-ru/parrot-stew-recipes/tree/parrot1
[15] https://github.com/ratt-ru/breizorro

3.4.3 Step 3: Second-Generation Calibration(2GC)

While 1GC ensured initial accurate data calibration by addressing systematic errors, we performed 2GC to refine the calibration solutions and create a deep sky model through self-calibration (self-cal). Self-cal is the process of using the target data (in our case, the calibrators) itself to refine calibration solutions and reduce imaging artefacts. We performed 2GC in a series of iterative steps as follows:

1. Predict - WSClean

   During the deconvolution process, WSClean creates a model image that is stored in FITS format. The self-calibration process uses model visibilities. Therefore, we used the `predict` command in WSClean to convert the previously created model image into model visibilities. This step is repeated after each imaging step for successive 2GC rounds. The final deep sky model is then used to create the residuals in Step 3.4.9.

2. Self-calibration - Quartical

   We perform self-cal using QuartiCal (Kenyon et al., 2025), a fast radio interferometer calibration suite to account for any residual calibration errors. We solve for delay and phase gain solutions with a per-antenna phase offset and a solution interval equal to the integration time of each observation.

3. Imaging - WSClean

   The resulting corrected visibilities from step 2 after the first round of self-cal were then imaged with WSClean down to a threshold of 5σ using the Breizorro mask constructed from the initial imaging step. Imaging at this step was done to check image quality and if the Root Mean Square (RMS) noise level was stabilising.

4. Sky Model Smoothing (up-sampling - SMOPS)

   The 6-band sky model derived from step 3 was up-sampled into 256 channels using the SMOPS tool. This tool takes in a set of per-band model images as produced by WSClean and outputs a set of model images at a higher frequency resolution using

polynomial interpolation in frequency at each model pixel (Smirnov et al., 2024). The resulting models are then used by WSClean to predict model visibilities with increased spectral resolution. The value of 256 is a trade-off between smoothness, compute, and disk space cost as discussed by Smirnov et al. (2024).

These steps were then repeated for two more rounds of self-cal until the RMS reached convergence. The convergence criteria for ending self-cal is defined by the point at which the RMS noise level stabilizes (i.e., ceases to decrease significantly, typically less than $1-3\%$ change) between successive iterations (Thompson et al., 2017).

3.4.4 Step 4: Flagging

After completing the self-calibration rounds, we flagged the data for any low-level RFI using Tricolour.

3.4.5 Step 5: Final Imaging

We produced the final 2GC calibrated images of the calibrator fields. The U-band images are presented in Section 3.4.5. The L-band images are presented in Appendix A.

2GC IMAGES

We performed 2GC calibration to iteratively correct for residual errors (e.g., ionospheric, beam-related, or atmospheric effects) that remained after 1GC to achieve the highest possible image quality and, subsequently, the deepest sky model. This was an essential step in maximizing the image dynamic range, allowing us to accurately model and subtract all visible flux from the time-averaged visibility data and finally plot the resulting residuals over the duration of the observation (the light curves) to analyse the temporal variability of the calibrator field.

2GC image of PKS J1939-6342

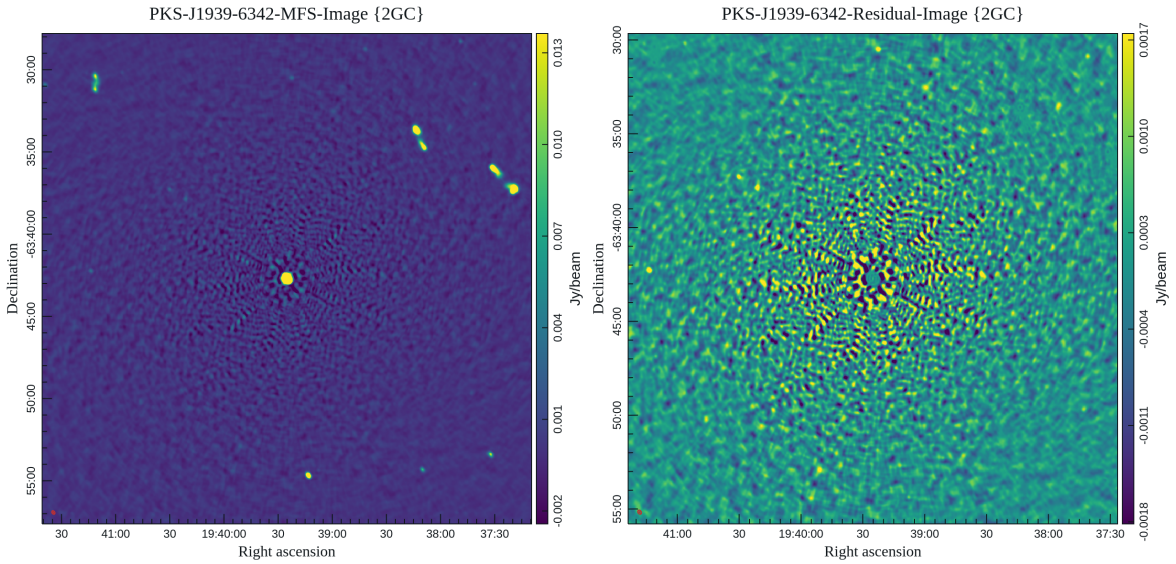

(a) PKS J1939-6342

(b) PKS J1939-6342 residual

Figure 3.9: U-band MFS and residual images of the flux calibrator PKS J1939-6342 after the 2GC. From the left figure, we note that PSF sidelobes associated with the calibrator are now well subtracted. The intensity of the radial spokes around the calibrator is reduced, and the calibrator source is seen clearly as a central unresolved point source. The residual image in Figure (3.7b) shows that no over-cleaning has occurred (no negative holes).

Figure 3.9 shows the U-band MFS and residual images of the flux calibrator PKS J1939-6342 after 2GC. From the MFS image, the integrated flux after 2GC is 13.23 ± 0.05 Jy, which showed an increase compared to that after 1GC (13.20 ± 0.05 Jy). This indicates a slightly stronger signal from the source after the additional calibration. Similar to the analysis in Section 3.3.2, we created off-source (containing no sources) regions to extract statistics to quantify the performance of 2GC. The off-source standard deviation (StdDev) and RMS values were lower by $\approx 38\%$, compared to 1GC, indicating lower noise levels around the calibrator and a higher signal-to-noise ratio (SNR).

2GC image of PKS J2152-2828

Figure 3.10 shows the U-band MFS and residual images of the phase calibrator PKS J2452-2828 after 2GC. We extracted statistics from the on-source and off-source regions to quantify the performance of 2GC. The integrated and peak flux densities show a slight

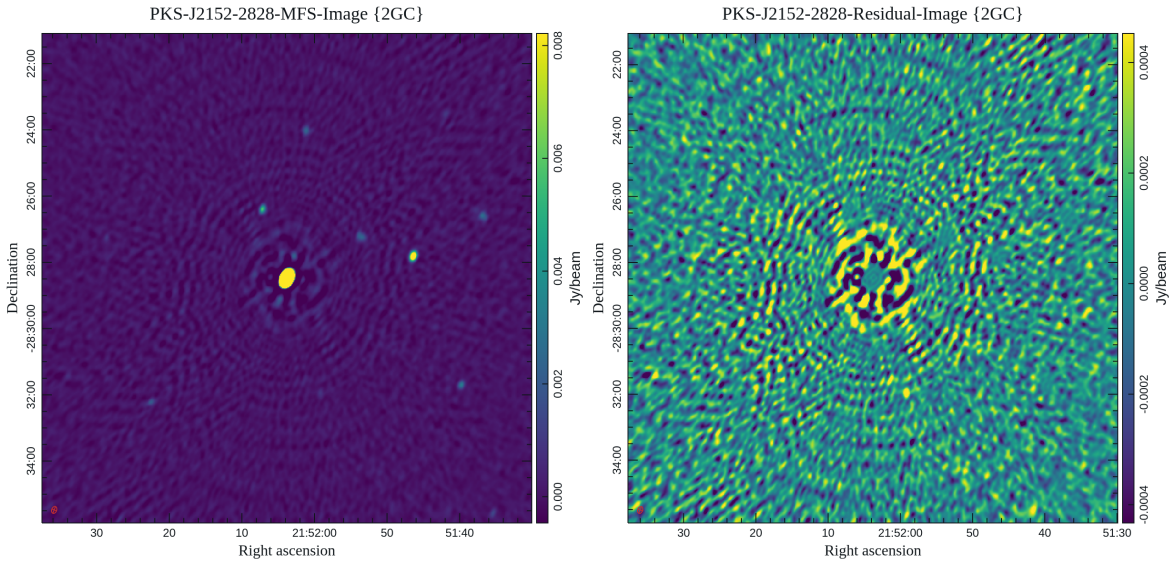

(a) PKS J2152-2828

(b) PKS J2152-2828 residual

Figure 3.10: MFS and residual images of the phase calibrator PKS J2152-2828 after 2GC. The bright PSF sidelobes around the calibrator have been reduced, and the faint sources close to the calibrator are now clearly visible. The residual image in Figure 3.10b shows that no over-cleaning has occurred (no negative holes).

increase ($\approx 2\%$) compared to 1GC. The RMS and StdDev in the off-source regions were also reduced, indicating lower noise levels around the calibrator and a higher signal-to-noise ratio (SNR).

3.4.6 Step 6: Source Catalog

Once the images produced met the convergence criteria, the next step was source extraction. Source extraction is the process of identifying and cataloging sources within an image. We used the Python Blob Detection and Source Finder (PyBDSF) package (Mohan and Rafferty, 2015) for this process. In PyBDSF, source extraction is the process of fitting Gaussians to identified islands of 'similar' emission and classifying sources as a group of Gaussians that fit the data within these islands. PyBDSF reads the image to be processed and computes basic image statistics such as background RMS. Using the default parameters, islands of contiguous emission are identified. Multiple Gaussians are fitted to each island, then the

Gaussians are flagged using the `thresh_isl` parameter (`thresh_isl` = 3 and `thresh_pix` = 5) values to produce an acceptable list of Gaussians.

Finally, the Gaussians within an island are then grouped into a discrete source. These sources and their respective properties, such as flux values and positions in *RA* and *Dec*, are then listed in a catalog. The outputs of this step are two files – a source list (.srl) and a Gaussian list (.gaul) that are used in the next step to create a master catalog.

3.4.7 Step 7: Master Catalog

Once the source extraction was complete, the two output files were used to run a cross-match, following parameters set to create a master catalog that would serve as a source library in the subsequent steps. The parameters set are:

- Name of the master catalog to be output.
- Right Ascension (*RA*) and Declination (*Dec*) of the center of the image.
- Radius - the radius of a circle centered on the *RA* and *Dec* above, within which the cross-matching of sources is run (1.7°).
- Catalogs - We cross-matched the two source catalogs from step 6.

3.4.8 Step 8: CORRECTED_DATA Column

We created a new column in the MS, the CORRECTED_DATA column, where the residuals created after subtracting the deep sky model from the calibrated visibilities would be stored.

3.4.9 Step 9: Subtract model

The 2GC calibrated visibilities are stored in the DATA column of the MS. The CORRECTED_DATA column created in step 3.4.8 is populated by subtracting the deep sky model (step 3.4.3) from the DATA column. The resulting residuals (DATA - MODEL) represent the temporal and

spectral variations in the data, isolated from the static sky brightness. Creating these residuals allowed us to focus on the dynamic changes over time, which are then used for light curve extraction and variability analysis.

3.4.10 Step 10: High Time Cadence (HTC) Images

Within this step, we created images at short time intervals. The shortest time interval that one can produce an image is the integration time (4 s for PKS J1939-6342, PKS J2152-2828 U-band observations, and 8 s for L-band observations). These per-integration images (High Time Cadence (HTC) images) of the calibrator field were created to analyse the temporal variability of each source by plotting the residual fluxes at the sources' (including the calibrator) position in every single snapshot image (timestamp), over the entire observation period – thus, creating individual per-source light curves.

3.4.11 Step 11: Image Cube

We then created an image cube by stacking the snapshot images produced in step 3.4.10 over the time axis. The image cube was viewed using the visualization tool CARTA (Ott et al., 2022). Within CARTA, we overlaid the image cube with the individual source regions to visually inspect and identify unique/interesting sources (such as extremely variable sources) as you flip through the cube.

3.4.12 Step 12: Extract Light Curves

The last step was the extraction of light curves from the cube created in the previous step. As highlighted at the beginning of the section, the need to discriminate between intrinsic variation, scintillation, and instrumental effects motivated the need to analyse the variability of additional sources in the calibrator field. This step used the master catalog created at step 3.4.7 as a source library. A source's *RA* and *Dec* were identified, a region (consistent in size) was created around the source, and the peak residual flux was extracted at that pixel position. These residual fluxes were then plotted for each timestamp in the cube for the

entire observation period. This was the process undertaken for each source. The results were light curves (LC) - plots of the residual flux as a function of the entire observation period. The mean-subtracted light curves derived from the residuals created in step 3.4.9 highlight fluctuations around a baseline of zero, making it easier to detect and analyse subtle variability in the sources. The user can also specify the number of sources whose light curves are to be extracted.

We extracted 30 light curves for the phase calibrator PKS J2152-2828 from the U-band observation. This number was chosen based on the pipeline's output and our analytical objectives. The pipeline inherently sorts the extracted light curves based on their flux in descending order, with the brightest source being assigned Source ID 0 (which is PKS J2152-2828 itself). Therefore, selecting the top 30 brightest sources ensured we included the most prominent and reliably detected sources within the calibrator field. The phase calibrator PKS J2152-2828 light curve (Source 0) is presented in Figure 3.11.

As highlighted previously, calibrators are observed intermittently during the observation of a science target; the calibrator field light curves therefore have gaps indicating when the science target was being observed, as seen in Figure 3.11. We extracted the residual fluxes, their corresponding uncertainties, and calculated statistical parameters for each ON-calibrator field observation (11 scans in U-band) as presented in the inset in Figure 3.11. The statistical analysis of the variability parameters for each scan was conducted to quantitatively analyse the STV of PKS J2152-2828 as well as sources within its field in the U-band as detailed in Chapter 4.

3.5 MeerKAT Science Data Processing (SDP)

The MeerKAT Science Data Processing (SDP) system executes an automatic continuum imaging pipeline, `katsdpcontim`[16], at the conclusion of each science target observation. We sourced the data used for our LTV analysis from the end-products of this pipeline. The pipeline is based on the Obit package (Cotton, 2008), which provides a uniform, reproducible workflow for producing calibrated continuum images with minimal human intervention. It

[16] https://github.com/ska-sa/katsdpcontim

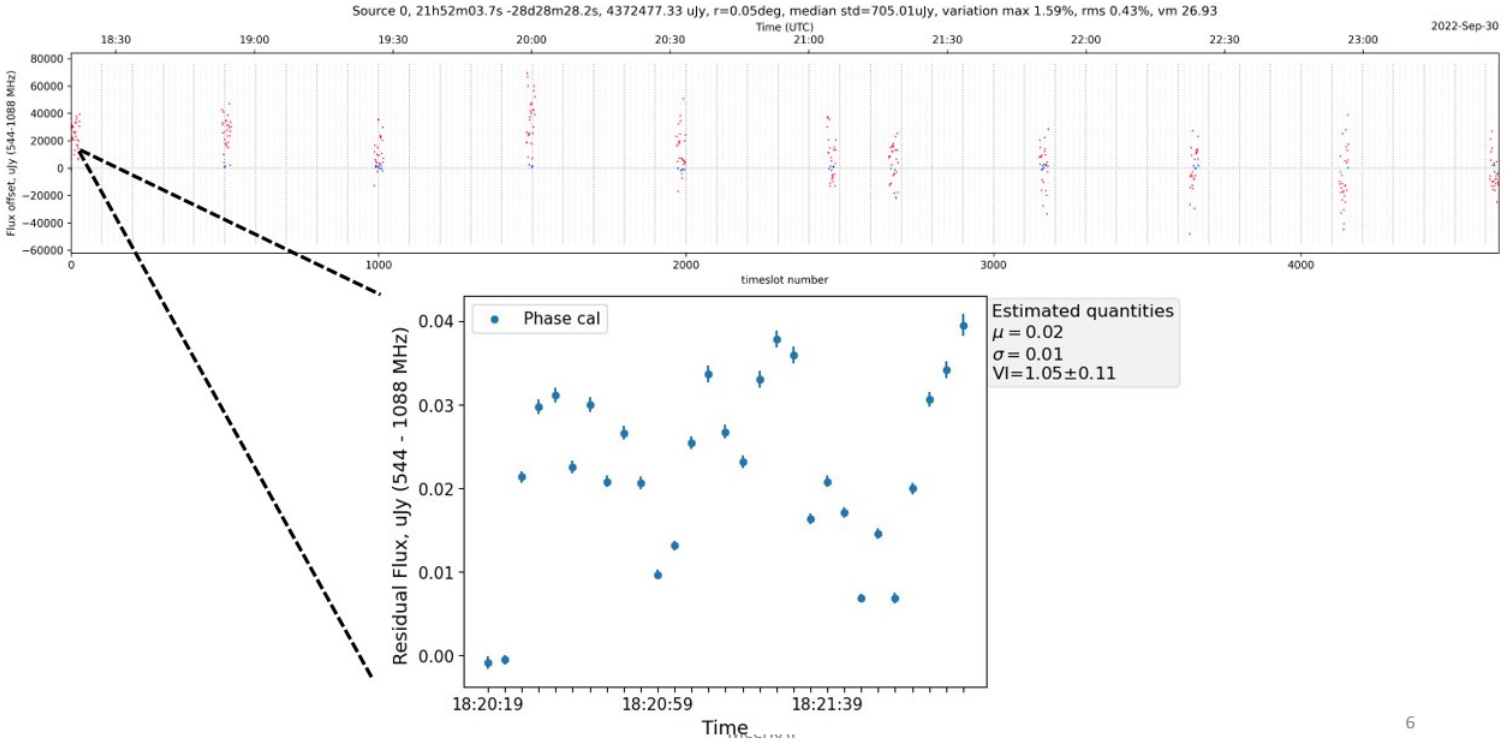

Figure 3.11: The main diagram displays the residual flux (calibrated data minus sky model data) for the phase calibrator PKS J2152-2828 in the U-band, as a function of time. Each data point represents the residual flux from a 4 s snapshot image, taken during one of the eleven 2 minute long ON-calibrator field observations (scans) over an $\approx$ 8 hour period. The gaps visible in the light curve occur when the array was focused on the primary science target. The rapid timeslot-to-timeslot variations are presumably due to extrinsic variability, such as Interplanetary Scintillation (IPS) (see Section 1.4.1 for discussion). The inset provides a closer look at the residual fluxes, their corresponding uncertainties, and summary statistical parameters for one of the individual ON-calibrator field observations (scans).

integrates all major steps of the data reduction chain: data averaging, calibration, wide-field imaging, self-calibration, and quality assessment, to ensure that science-ready data products are archived and readily accessible. In this section, we provide a summary of the pipeline:

1. **Data Averaging and Preprocessing**

   To reduce the raw data volume, the pipeline performs baseline-dependent averaging. The averaging is chosen such that the amplitude loss at 1° from the phase center remains at $\leq 1\%$ (SARAO). This yields a compression factor of approximately four while preserving image fidelity within the primary beam. The averaged data are then exported into a format compatible with the Obit-based calibration and imaging framework.

2. **Wide-field and Wide-band Imaging**

   Wide-field imaging challenges are addressed by a faceting strategy. For L-band observations, the inner 1° of the primary beam is divided into ~ 140 facets. This number balances the need to minimise non-coplanar w-term effects against the computational cost of gridding and deconvolution. At U-band, a similar number of facets is employed, though across a wider effective field of view due to the larger beam size. In addition, the wide instantaneous MeerKAT bandwidth is subdivided into ~ 10 sub-bands and imaged independently. This approach mitigates spectral smearing and allows the frequency dependence of source structures and instrumental effects to be tracked. Bright outlier sources outside the primary beam are also modelled through additional facets seeded from external catalogues such as SUMSS, ensuring that sidelobes from distant sources do not corrupt the central field.

3. **Self-Calibration and Model Refinement**

   Calibration occurs in two rounds. The first is a shallow cycle, cleaning the image down to $\sim 1\,\mathrm{mJy}$, sufficient enough to correct the bulk of residual phase errors. The second cycle reaches a depth of $\sim 100\,\mu\mathrm{Jy}$, corresponding approximately to the theoretical thermal noise of a single channel in a 32k-channel observation. These thresholds are empirically chosen to ensure stable convergence while avoiding fitting to noise peaks or spurious residuals. The imaging process follows a major/minor cycle structure, in

which the sky model is periodically updated and subtracted from the visibilities before the residual image is recomputed. This loop is iterated until convergence, typically within fewer than ten major cycles, with the maximum number capped to limit computational cost (Offringa et al., 2014).

4. **Final Products and Quality Assessment**

   At the conclusion of the deconvolution, the pipeline combines the facets within each sub-band to yield the final full-resolution images. The data products include FITS files suitable for science analysis as well as PNG thumbnails for quick inspection. In addition, the pipeline generates a Continuum Image Quality Report, introduced in April 2021, which cross-matches detected sources against SUMSS and NVSS. The report provides statistics on positional offsets, flux density ratios, completeness, and reliability, together with diagnostic information on calibration such as antenna participation, RFI, and flagging summaries, SNR ratio distributions, flux calibrator solutions, and gain stability. An example calibration report for our U-band observation is available here [17].

In summary, `katsdpcontim` provides an automated, standardised pipeline for MeerKAT continuum observations. By integrating baseline-dependent averaging, wide-field multi-facet imaging, multi-frequency sub-band handling, iterative self-calibration, and comprehensive quality reporting, it ensures both data compression efficiency and high-fidelity science-ready products. For the LTV analysis, we specifically used the continuum imaging reports produced by the pipeline to extract the measured flux in the U-, L-, and S-band for our sample of calibrators over the years:

- The U-band data used was from Aug/30/2021 - Oct/17/2023.
- The L-band data used was from Nov/10/2020 - Nov/25/2022
- The S-band data used was from Jun/16/2022 - Jun/11/2023.

[17] https://archive.sarao.ac.za/s3/1664561173-meerkatreductionproduct/Calibration+Report-1/calreport1.html

3.6 Summary

This chapter detailed the comprehensive data reduction process undertaken for the MeerKAT observations summarised in Table 3.1, from raw visibilities through calibration, flagging, imaging, and ultimately, the extraction of light curves. The process began with First-Generation Calibration (1GC) using the CARACal pipeline, which effectively mitigated major instrumental and atmospheric effects (see Section 3.2). Key quantitative results from this stage demonstrated its success: delay solutions for the calibrators were both well within acceptable thresholds. Furthermore, amplitude variations of the antenna responses clustered around 1.0 ± 0.2, and phase variations were confined to within $\pm 20^{\circ}$, indicating robust corrections of frequency-dependent effects. The U-band images of PKS J1939-6342 and PKS J2152-2828 after 1GC yielded integrated flux densities of 13.20 Jy and 4.26 Jy, similar to the published U-band MeerKAT Knowledge Base[18] fluxes.

Building upon this foundation, Second-Generation Calibration (2GC), performed with the Madroon pipeline, aimed to further refine the data by addressing residual calibration errors from 1GC (see Section 3.4.3). The primary improvement metrics for 2GC focused on noise reduction and signal enhancement. For PKS J1939-6342, the off-source StdDev and RMS values were reduced by $\approx 38\%$, signifying a substantial decrease in noise levels. Similarly, for PKS J2152-2828, the integrated and peak flux densities showed a slight increase of about 2%, coupled with reduced off-source RMS and StdDev, which collectively indicated an improved SNR and image quality.

However, the demanding nature of processing MeerKAT data, particularly for bright calibrator fields, introduced several methodological challenges. The pipeline had to manage complex wide-field effects, direction-dependent gains, and primary beam variations. A significant challenge was the presence of deconvolution artifacts arising from the cleaning of very bright calibrator sources, which left residual patterns in the images and affected fainter sources, especially those within 0.5° of the phase center. Additionally, the STV analysis, which relies on residual fluxes derived from subtracting a deep sky model, operates under the fundamental assumption of the deep sky model's accuracy.

[18] https://skaafrica.atlassian.net/wiki/spaces/ESDKB/pages/1479802903/UHF+gain+calibrators

Although initial 1GC and 2GC were also performed for the calibrators PKS J1939-6342 and PKS J1008+0730 in the U-band and L-band (see Appendix A), light curve extraction and the subsequent STV analysis are limited to the U-band observation of PKS J2152-2828 and the 30 brightest sources within its field. Consequently, while the STV analysis for PKS J2152-2828 that follows is robust for this specific dataset, it may not be fully representative of the entire population of MeerKAT calibrators or reflect variability characteristics across all MeerKAT observing bands. This focused approach was necessary to achieve the specific goals of this thesis, laying the groundwork for the detailed analysis presented in Chapter 4.

Chapter 4

Flux Stability Analysis: Long-Term and Short-Term Variability

In this chapter, we undertake our second objective as outlined in Section 1.6 to: Conduct a comprehensive flux stability analysis of a sample of southern sky calibrators observed by MeerKAT. Section 4.1.1 presents the implementation of the variability metrics discussed in detail in Section 1.5.1 and applied in our Long-Term Variability (LTV) and Short-Term Variability (STV) analyses. In Section 4.1, we present the LTV analysis performed over a period of $\approx$ 2 years; specifically from 2021-2023 in the U-band, 2020-2022 in the L-band, and 2022-2023 in the S-band. Additionally, the LTV light curves are presented in appendix B. In Section 4.2, we conduct STV analysis on the 30 light curves from PKS J2152-2828's field extracted in Chapter 3.

The analyses presented in this chapter utilize data processed through two distinct pipelines: the MeerKAT Science Data Processing (SDP) pipeline and the Madroon pipeline, as detailed in Chapter 3. For the LTV analysis, we used data processed through the SDP pipeline as detailed in Section 3.5. Given the extensive duration of the data reduction process required for long-term variability studies, utilizing these pre-processed data products was the most efficient approach. However, the STV analysis required a more tailored data reduction approach due to the specific focus on short timescales and was performed using the Madroon pipeline as detailed in Section 3.4.

4.1 Long-Term Variability Analysis

4.1.1 LTV Metrics

As outlined in detail in Section 1.5.1, we use multiple variability metrics (also referred to as VI henceforth) that provide complementary perspectives on flux density variations in our analysis. We implemented these variability metrics, together with their uncertainty calculations, in Python to analyse our data. All calculated uncertainties (Δ) for the variability metrics were derived using the method of propagation of errors (also known as propagation of uncertainty) (Taylor, 1997).

1. **VI_{Aller} and VI_{Fan}**

   VI_{Aller} and VI_{Fan} in Equations 1.22 and 1.24 respectively, are straightforward measures but are sensitive to outliers. We include them as they are reliable in identifying cases of strong flaring or burst-like activity. While VI_{Aller} is the most direct peak-to-peak ratio, VI_{Fan} attempts to make this measure more conservative by subtracting the error from S_{max} and adding the error to S_{min}, giving a "corrected" maximum range of variability. Tables 4.1 and 4.2 contain the VI_{Aller} and VI_{Fan} source VI, respectively, over the analysed period, along with their uncertainties, expressed as percentages. The maximum value in each column (U-, L-, and S-band) is highlighted in bold. **PKS J0730-1141** in the U-band and **PKS J0854+2006** in the L- and S- bands show the largest flux excursion in the two-year monitoring period.

2. **NVA** and **RMSD**

   The NVA (Equation 1.26) indicates how much the flux varies relative to its mean, independent of instrumental effects, while the RMSD (Equation 1.29) gives the spread of the flux measurements around the mean flux, relative to the mean flux, indicating the relative variability. Tables 4.3 and 4.4 contain the NVA and RMSD source VI values, respectively, over the analysed period, along with their uncertainties, expressed as percentages. The maximum values in each band are highlighted in bold. **PKS J0730-1141** in the U-band and **PKS J0854+2006** in the L- and S- bands show the largest relative variability in the two-year monitoring period.

3. **VI_{debias}**

   The debiased variability index (VI_{debias}) (Equation 1.34) offers the most conservative estimate of intrinsic variability as it removes the noise variance, correcting for measurement errors. Critically, if the numerator in Equation 1.34 that represents the intrinsic variance (observed variance minus measurement error variance) is negative, it would indicate that the source is not variable relative to the noise. Therefore, based on this observation, we filtered out all sources flagged by a negative intrinsic variance, ensuring that only positive intrinsic variability cases were passed to the final analysis stage. Additionally, if VI_{debias} is comparable to or smaller than its uncertainty (ΔVI_{debias}), it might indicate that the observed variability is consistent with the uncertainties of the measurement, and the source may not be significantly variable. Table 4.5 contains the VI_{debias} source VI over the analysed period, along with their uncertainties, expressed as percentages. The maximum values in each band are highlighted in bold. **PKS J0730-1141** in the U-band, **PKS J0828-3731** in the L-band, and **PKS J0854+2006** in the S-band show the largest sustained, intrinsic fluctuations after noise removal in the two-year monitoring period.

Taken all together, these indices allow us to verify our results and mitigate the limitations of any single metric, thereby improving the reliability of our variability assessment in this study. The results of the various variability metrics for each frequency band are given in Tables 4.1-4.5. The calibrators **PKS J0730-1141** in the U-band, and **PKS J0854+2006** in the L- and S-band show the largest sustained fluctuations over the two-year monitoring period. The LTV light curves over the analysed epoch are presented in Appendix B.

NAME	$VI_{Aller}U$	$\Delta VI_{Aller}U$	$VI_{Aller}L$	$\Delta VI_{Aller}L$	$VI_{Aller}S$	$\Delta VI_{Aller}S$
PKS J0022+0014	2.10	0.58	1.56	0.21	1.44	0.43
PKS J0210-5101	3.82	0.84	5.14	1.55	7.45	0.97
PKS J0303-6211	11.18	0.56	12.75	0.79	7.21	0.72
PKS J0323+0534	1.69	0.63	0.88	0.21	2.70	0.64
PKS J0420-6223	1.71	0.68	1.34	0.25	1.53	0.35
PKS J0423-0120	7.96	0.83	12.56	0.67	5.94	0.40
PKS J0440-4333	2.40	0.75	1.84	0.67	6.68	0.71
PKS J0447-2203	1.89	0.64	1.33	0.27	1.26	0.38
PKS J0453-2807	7.77	0.70	5.26	0.38	7.01	0.68
PKS J0538-4405	5.99	0.70	10.98	0.99	14.26	1.01
PKS J0609-1542	5.78	0.62	15.87	0.54	13.90	0.65
PKS J0616-3456	3.55	0.74	1.44	0.24	1.73	0.51
PKS J0632+1022	3.67	0.83	2.75	0.31	2.93	0.84
PKS J0730-1141	**20.71**	0.69	15.89	0.45	9.03	0.67
PKS J0735-1735	15.46	0.63	1.83	0.38	3.07	0.27
PKS J0828-3731	10.67	0.53	20.17	0.25	1.01	0.37
PKS J0854+2006	16.17	0.61	**22.38**	0.56	**15.01**	0.89
PKS J0906-6829	4.44	0.72	2.04	0.38	2.43	0.43

Table 4.1: VI_{Aller} variability metric along with its uncertainties, expressed as a percentage for the sample sources, rounded to two decimal places. The maximum value in each column (U-, L-, and S-band) is highlighted in bold. PKS J0730-1141 in the U-band and PKS J0854+2006 in the L- and S- bands show the largest flux excursion in the two-year monitoring period.

SRC_NAME	$VI_{Fan}U$	$\Delta VI_{Fan}U$	$VI_{Fan}L$	$\Delta VI_{Fan}L$	$VI_{Fan}S$	$\Delta VI_{Fan}S$
PKS J0022+0014	1.53	0.82	1.35	0.29	1.02	0.62
PKS J0210-5101	3.01	1.15	3.67	2.08	6.56	1.27
PKS J0303-6211	10.68	0.70	12.10	1.03	6.54	0.94
PKS J0323+0534	1.07	0.88	0.67	0.30	2.07	1.14
PKS J0420-6223	1.04	0.95	1.09	0.35	1.18	0.51
PKS J0423-0120	7.19	1.09	11.96	0.85	5.56	0.54
PKS J0440-4333	1.68	1.05	1.18	0.94	6.01	0.97
PKS J0447-2203	1.27	0.89	1.06	0.42	0.88	0.59
PKS J0453-2807	7.12	0.91	4.90	0.51	6.37	0.90
PKS J0538-4405	5.34	0.93	10.10	1.25	13.35	1.39
PKS J0609-1542	5.20	0.82	15.40	0.67	13.36	0.80
PKS J0616-3456	2.83	1.04	1.20	0.34	1.22	0.83
PKS J0632+1022	2.87	1.15	2.45	0.43	2.10	1.38
PKS J0730-1141	**20.15**	0.80	15.51	0.54	8.43	0.86
PKS J0735-1735	14.91	0.82	1.45	0.62	2.80	0.40
PKS J0828-3731	10.21	0.67	19.98	0.28	0.65	0.52
PKS J0854+2006	15.67	0.72	**21.95**	0.62	**14.24**	1.10
PKS J0906-6829	3.75	0.99	1.67	0.53	2.01	0.60

Table 4.2: VI_{Fan} variability metric along with its uncertainties, expressed as a percentage for the sample sources, rounded to two decimal places. The maximum value in each column (U-, L-, and S-band) is highlighted in bold. **PKS J0730-1141** in the U-band and **PKS J0854+2006** in the L- and S- bands show the largest flux excursion in the two-year monitoring period.

SRC_NAME	NVA U	ΔNVA U	NVA L	ΔNVA L	NVA S	ΔNVA S
PKS J0022+0014	2.57	0.87	2.17	0.64	1.47	0.51
PKS J0210-5101	4.51	1.45	4.90	1.32	11.65	3.77
PKS J0303-6211	11.65	3.39	15.58	3.50	9.79	3.13
PKS J0323+0534	2.06	0.82	1.05	0.34	2.52	0.83
PKS J0420-6223	2.15	0.95	1.12	0.30	1.39	0.48
PKS J0423-0120	5.51	1.63	8.47	2.14	7.18	2.29
PKS J0440-4333	2.99	1.07	1.91	0.59	8.74	3.08
PKS J0447-2203	1.96	0.74	1.27	0.30	0.94	0.33
PKS J0453-2807	7.50	2.20	4.95	1.12	7.54	2.42
PKS J0538-4405	5.69	1.68	12.15	2.75	24.47	7.79
PKS J0609-1542	5.53	1.63	15.30	3.44	25.33	8.06
PKS J0616-3456	4.24	1.19	1.46	0.35	1.84	0.61
PKS J0632+1022	3.95	1.13	3.17	0.93	3.13	1.35
PKS J0730-1141	**20.63**	5.55	22.80	6.62	16.56	6.79
PKS J0735-1735	16.53	4.44	2.06	0.62	3.98	1.66
PKS J0828-3731	8.50	2.29	23.88	6.94	1.36	0.65
PKS J0854+2006	14.53	3.90	**28.51**	7.68	**32.60**	13.44
PKS J0906-6829	5.15	1.43	1.73	0.48	1.91	0.81

Table 4.3: NVA variability metric along with its uncertainties, expressed as a percentage for the sample sources, rounded to two decimal places. The maximum value in each column (U-, L-, and S-band) is highlighted in bold. **PKS J0730-1141** in the U-band and **PKS J0854+2006** in the L- and S- bands show the largest flux variation relative to the mean in the two-year monitoring period.

SRC_NAME	RMSD U	ΔRMSD U	RMSD L	ΔRMSD L	RMSD S	ΔRMSD S
PKS J0022+0014	1.56	0.24	1.29	0.09	1.09	0.21
PKS J0210-5101	2.78	0.36	3.02	0.44	6.68	0.45
PKS J0303-6211	7.62	0.21	9.43	0.20	6.28	0.31
PKS J0323+0534	1.26	0.28	0.66	0.09	2.01	0.45
PKS J0420-6223	1.21	0.29	0.66	0.08	1.06	0.18
PKS J0423-0120	5.16	0.31	7.37	0.21	4.10	0.19
PKS J0440-4333	1.57	0.28	1.17	0.20	5.28	0.60
PKS J0447-2203	1.34	0.26	0.92	0.08	0.95	0.22
PKS J0453-2807	5.17	0.27	3.44	0.12	5.48	0.29
PKS J0538-4405	4.00	0.26	7.99	0.30	13.74	0.34
PKS J0609-1542	4.29	0.25	11.48	0.14	11.81	0.35
PKS J0616-3456	2.39	0.26	0.88	0.07	1.25	0.31
PKS J0632+1022	2.59	0.29	2.04	0.12	2.49	0.62
PKS J0730-1141	**14.79**	0.24	15.42	0.16	8.67	0.38
PKS J0735-1735	10.52	0.20	1.32	0.17	2.65	0.19
PKS J0828-3731	6.74	0.18	17.33	0.09	0.96	0.23
PKS J0854+2006	10.84	0.22	**17.87**	0.24	**15.44**	0.68
PKS J0906-6829	3.23	0.26	1.29	0.13	1.99	0.24

Table 4.4: RMSD variability metric along with its uncertainties, expressed as a percentage for the sample sources, rounded to two decimal places. The maximum value in each column (U-, L-, and S-band) is highlighted in bold. **PKS J0730-1141** in the U-band and **PKS J0854+2006** in the L- and S- bands show the largest relative variability in the two-year monitoring period.

SRC_NAME	**VI_{debias}U**	**ΔVI_{debias}U**	**VI_{debias}L**	**ΔVI_{debias}L**	**VI_{debias}S**	**ΔVI_{debias}S**
PKS J0022+0014	0.49	0.09	0.44	0.03	0.38	0.08
PKS J0210-5101	0.91	0.14	0.78	0.14	2.46	0.23
PKS J0303-6211	2.66	0.20	2.70	0.25	2.33	0.18
PKS J0323+0534	0.36	0.12	0.22	0.03	0.72	0.17
PKS J0420-6223	0.32	0.13	0.17	0.03	0.37	0.07
PKS J0423-0120	1.78	0.14	2.31	0.17	1.52	0.09
PKS J0440-4333	0.48	0.11	0.28	0.07	1.66	0.28
PKS J0447-2203	0.40	0.11	0.25	0.02	0.33	0.09
PKS J0453-2807	1.79	0.13	0.98	0.05	2.03	0.15
PKS J0538-4405	1.38	0.10	2.28	0.19	5.11	0.65
PKS J0609-1542	1.48	0.11	3.30	0.36	4.39	0.49
PKS J0616-3456	0.77	0.09	0.24	0.02	0.44	0.12
PKS J0632+1022	0.82	0.10	0.70	0.05	1.01	0.29
PKS J0730-1141	**4.89**	0.68	5.40	0.77	3.74	0.33
PKS J0735-1735	3.47	0.35	0.45	0.06	1.13	0.09
PKS J0828-3731	2.22	0.15	**6.06**	0.97	0.37	0.11
PKS J0854+2006	3.58	0.37	5.90	0.99	**6.66**	0.94
PKS J0906-6829	1.05	0.09	0.42	0.04	0.84	0.11

Table 4.5: VI_{debias} variability metric along with its uncertainties, expressed as a percentage for the sample sources, rounded to two decimal places. The maximum value in each column (U-, L-, and S-band) is highlighted in bold. **PKS J0730-1141** in the U-band, **PKS J0828-3731** in the L-band, and **PKS J0854+2006** in the S-band show the largest sustained, intrinsic fluctuations after noise removal in the two-year monitoring period.

4.1.2 LTV Pairwise Analysis

In the previous section, we calculated the individual LTV VI and noted that the calibrators **PKS J0730-1141** in the U-band, and **PKS J0854+2006** in the L- and S-band show the largest sustained fluctuations over the two-year monitoring period. We went on to perform a pairwise analysis between frequency bands. In these plots, the statistical confidence threshold indicating pairwise variability was set at VI values $\geq 3\sigma$, where σ is the standard deviation in the VI. This is a well-established criterion in statistics, as it corresponds to a 99.7% confidence interval, signifying that any data point outside this range is rare and statistically significant (Wall and Jenkins, 2003).

In Figures 4.1 - 4.5, we present the results of the LTV pairwise analysis of our calibrator sample. The figures (4.1 - 4.5) are pairwise scatter plots comparing the different VI – VI_{Aller}, VI_{Fan}, NVA, RMSD, and VI_{debias} across the three MeerKAT bands. Each point in these plots represents an individual calibrator source, with its position indicating its VI value in two different frequency bands. Radio Galaxies (RGs) are depicted in blue, and Quasars (QSOs) in orange.

A source that falls above the 3σ threshold (dotted lines) on both axes is confirmed to be significantly variable in both bands. Its position also suggests whether the degree of variability is similar in both bands or whether one band exhibits significantly greater variation. It is important to note that while all sources are broadly classified as either RGs or QSOs for this analysis, the QSO class encompasses subclasses (e.g., flat-spectrum radio quasars, steep-spectrum quasars, blazars, and high optical polarization quasars) that are known to exhibit diverse variability characteristics, as detailed in Section 2.1.1.

1. **VI_{Aller}**

   The results for VI_{Aller} are shown in Figure 4.1. As shown in Figure 4.1a, the sources above 3σ in L-band are PKS J0828-3731 and PKS J0854+2006 while in the U-band it is the source PKS J1058+0133. No common sources are showing considerable variability at frequencies less than 1.283 GHz. Sources above 3σ in the S-band are PKS J0538-4405, PKS J0609-1542, and PKS J0854 + 2006. However, PKS J0854+2006 is a common outlier in the L and S bands 4.1b. Therefore, this source appears to show

variability at frequencies greater than 1.283 GHz for the variability parameter VI_{Aller}.

2. **VI_{Fan}**

   Similarly, the pair-wise band analysis for VI_{Fan} is shown in Figure 4.2. As depicted in Figure 4.2a, the source exhibiting variability above 3σ in the L-band is PKS J0854+2006, while in the U-band it is PKS J1008+0730. There are no common sources showing significant variability across both bands at frequencies less than 1.283 GHz. The source PKS J0854+2006 is an outlier with variability above 3σ in both the L- and S- bands, as illustrated in Figure 4.2c. Therefore, PKS J0854+2006 shows variability at frequencies greater than 1.283 GHz for the variability parameter VI_{Fan} similar to VI_{Aller}.

3. **NVA**

   The pair-wise band analysis for the NVA parameter is shown in Figure 4.3. As depicted in Figure 4.3a, PKS J0854+2006 shows variability above 3σ in the L-band, while PKS J0318+1628 exhibits variability above 3σ in the U-band. There are no common sources demonstrating significant variability across both bands at frequencies less than 1.283 GHz. However, PKS J0854+2006 appears as an outlier with variability exceeding 3σ in both the L and S bands, as illustrated in Figure 4.3c. Therefore, PKS J0854+2006 exhibits variability at frequencies greater than 1.283 GHz for the NVA parameter, similar to both VI_{Aller} and VI_{Fan}.

4. **RMSD**

   The results for RMSD are presented in Figure 4.4. As shown in Figure 4.4a, PKS J0828-3731 and PKS J0854+2006 exhibit variability above 3σ in the L-band, while in the U-band, it is PKS J1058+0133. There are no common sources demonstrating significant variability across both bands at frequencies less than 1.283 GHz. However, PKS J0854+2006 appears as an outlier with a variability exceeding 3σ in both the L- and S- bands, as illustrated in Figure 4.4c. Therefore, similar to the previous variability parameters, PKS J0854+2006 shows variability at frequencies greater than 1.283 GHz for the RMSD parameter.

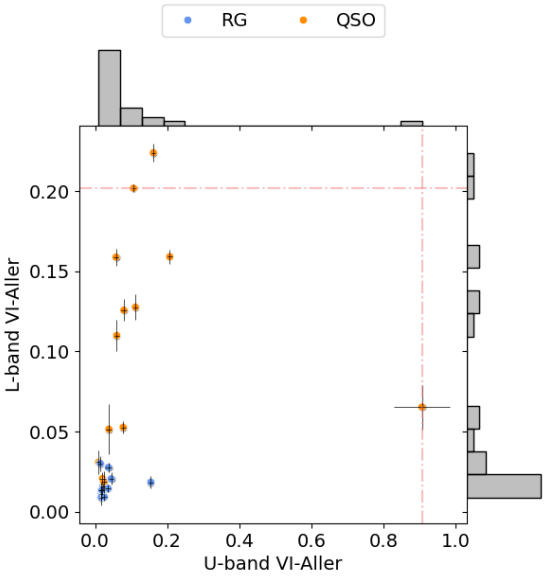

(a) Source in U-band VI_{Aller} above 3σ:PKS J1058+0133. Source in L-band VI_{Aller} above 3σ:PKS J0828-3731, PKS J0854+2006.

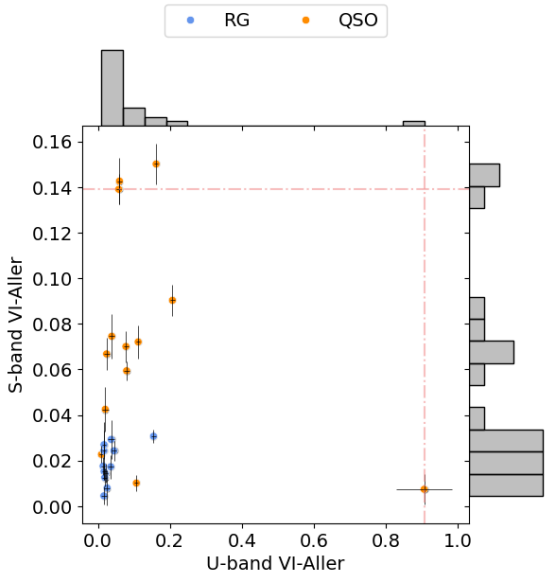

(b) Source in U-band VI_{Aller} above 3σ: PKS J1058+0133. Source in S-band VI_{Aller} above 3σ: PKS J0538-4405, PKS J0609-1542, PKS J0854+2006.

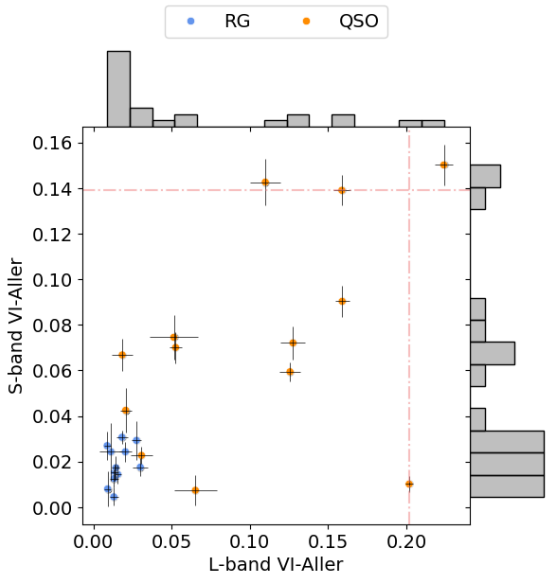

(c) Source in L-band VI_{Aller} above 3σ: PKS J0828-3731, PKS J0854+2006. Source in S-band VI_{Aller} above 3σ: PKS J0538-4405, PKS J0609-1542, PKS J0854+2006. Common sources exceeding 3σ: PKS J0854+2006.

Figure 4.1: Scatter plots of VI_{Aller} values for individual calibrator sources in our sample (RGs are plotted in blue, and QSOs are plotted in orange) in a L- vs U-band, S- vs U-band, and S vs L band pairwise analysis.

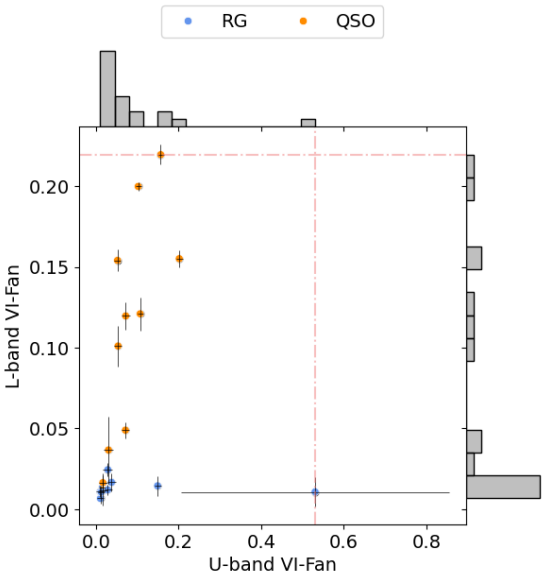

(a) Source in U-band VI_{Fan} above 3σ: PKS J1008+0730. Source in L-band VI_{Fan} above 3σ: PKS J0854+2006.

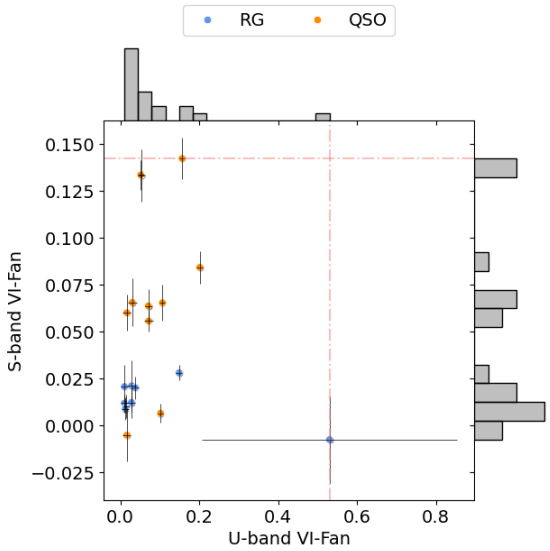

(b) Source in U-band VI_{Fan} above 3σ: PKS J1008+0730. Source in S-band VI_{Fan} above 3σ: PKS J0854+2006. Common source above 3σ: None.

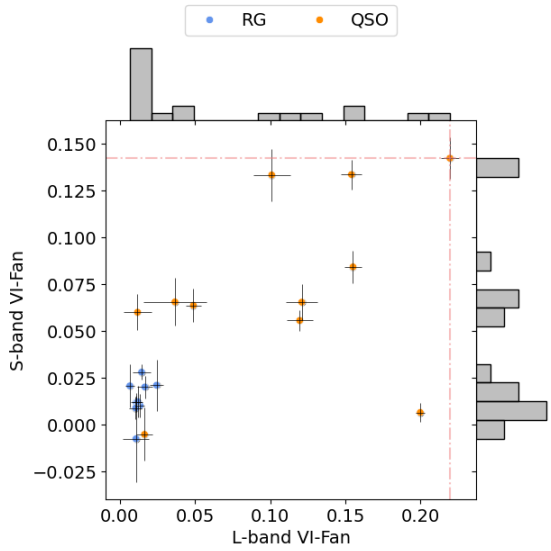

(c) Source in L-band VI_{Fan} above 3σ: PKS J0854+2006. Source in S-band VI_{Fan} above 3σ: PKS J0854+2006. Common sources exceeding 3σ: PKS J0854+2006.

Figure 4.2: Scatter plots of VI_{Fan} values for individual calibrator sources in our sample (RGs are plotted in blue, and QSOs are plotted in orange) in a L- vs U-band, S- vs U-band, and S vs L band pairwise analysis.

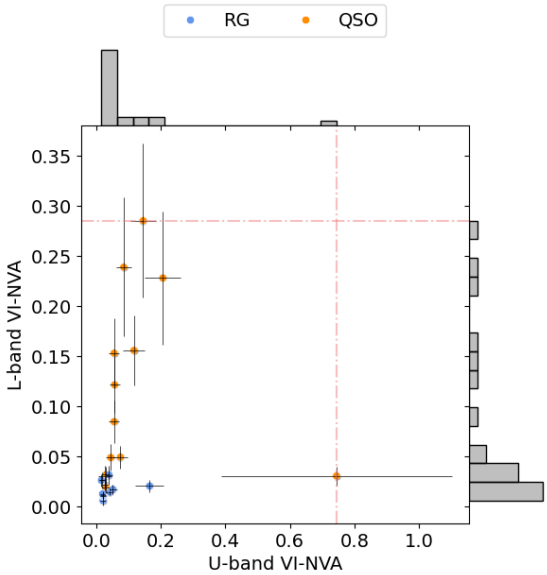

(a) Source in U-band NVA above 3σ: PKS J0318+1628. Source in L-band NVA above 3σ: PKS J0854+2006.

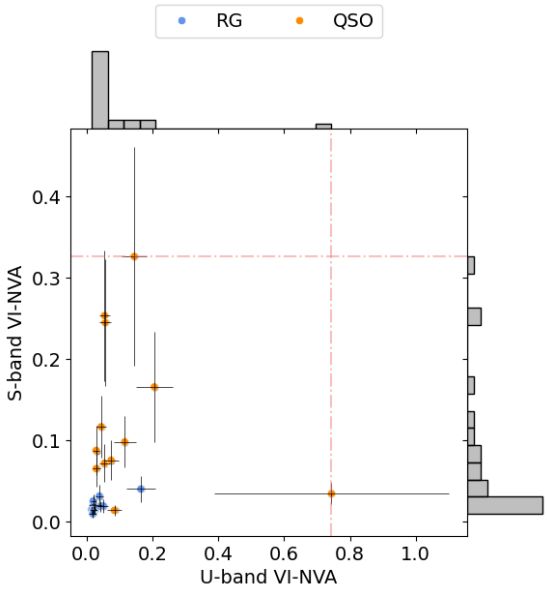

(b) Source in U-band NVA above 3σ: PKS J0318+1628. Source in S-band NVA above 3σ: PKS J0854+2006. Common source above 3σ: None.

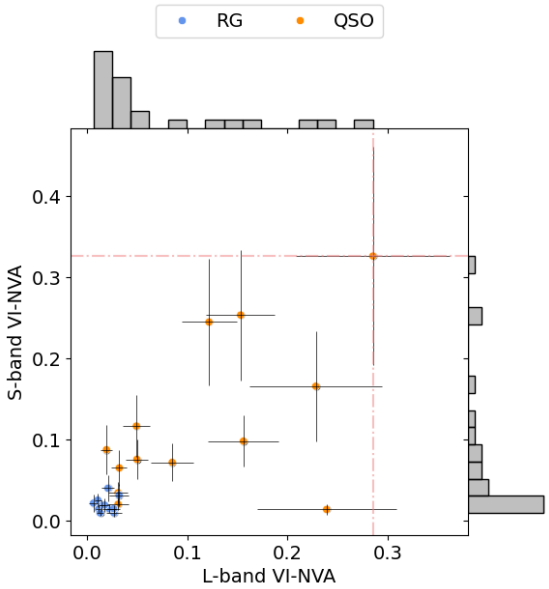

(c) Source in L-band NVA above 3σ: PKS J0854+2006. Source in S-band NVA above 3σ: PKS J0854+2006. Common sources exceeding 3σ: PKS J0854+2006.

Figure 4.3: Scatter plots of NVA values for individual calibrator sources in our sample (RGs are plotted in blue, and QSOs are plotted in orange) in a L vs U band, S vs U band, and S vs L band pairwise analysis.

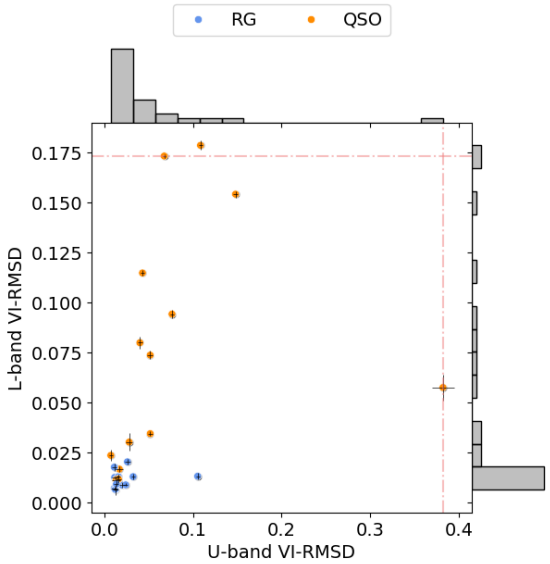

(a) Source in U-band Source in U-band RMSD above 3σ: PKS J1058+0133'. Source in L-band RMSD above 3σ: PKS J0828-3731, PKS J0854+2006.

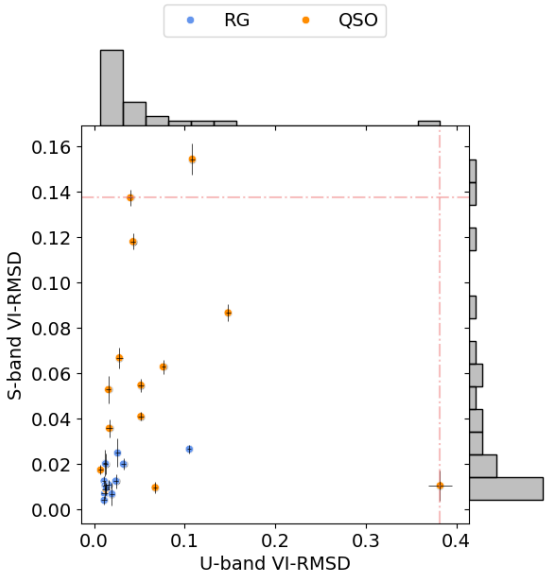

(b) Source in U-band RMSD above 3σ: PKS J1058+0133'. Source in S-band RMSD above 3σ: PKS J0538-4405, PKS J0854+2006. Common source above 3σ: None.

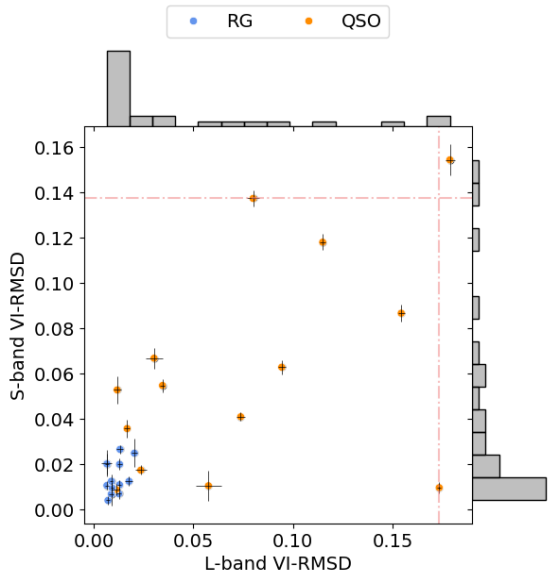

(c) Source in L-band RMSD above 3σ: PKS J0828-3731, PKS J0854+2006. Source in S-band RMSD above 3σ: PKS J0538-4405, PKS J0854+2006. Common sources exceeding 3σ: PKS J0854+2006.

Figure 4.4: Scatter plots of RMSD values for individual calibrator sources in our sample (RGs are plotted in blue, and QSOs are plotted in orange) in a L vs U band, S vs U band, and S vs L band pairwise analysis.

5. **VI_{debias}**

   The results for the VI_{debias} are displayed in Figure 4.5 shows that the sources PKS J0828-3731 and PKS J0854+2006 exhibit variability above 3σ in the L-band, while in the U-band, it is PKS J0730-1141. There are no common sources demonstrating significant variability across both bands at frequencies less than 1.283 GHz. However, PKS J0854+2006 appears as an outlier with variability exceeding 3σ in both the L and S bands, as illustrated in Figure 4.5c. PKS J0854+2006 exhibited variability at frequencies greater than 1.283 GHz for the debiased VI parameter.

Our results showed that no significant variability was found below 1.283 GHz, except for **PKS J0854+2006**, that exhibited LTV at frequencies $>$ 1.283 GHz. It is worth noting that this analysis holds the potential to distinguish sources that are genuinely broadband variable from those whose variation is confined to a single frequency range, which could help constrain physical mechanisms (e.g., synchrotron self-absorption).

4.1.3 LTV VI Mutual Correlations

In Table 4.6, we present the average values for the LTV variability metrics. As the NVA (Equation 1.26) inherently accounts for the standard deviation and the mean error level in the flux measurements, we investigated its correlation to each of the other variability metrics in all three MeerKAT bands, in a similar analysis to Fan et al. (2007). The results of the mutual correlation between different variability metrics are presented in Table 4.7 and Figure 4.6. Table 4.7 quantifies these correlations by presenting the linear fit parameters; m$\pm\Delta m$ for slope, c$\pm\Delta c$ for the intercept, and the reduced chi-squared (χ^2_r) for each pairwise comparison with NVA across the U-band, L-band, and S-band.

We observed that the NVA correlation to each variability parameter is $\approx$ a 1:1 linear relationship except for the debiased index (VI_{debias}). This strong correlation suggests that these indices largely capture similar aspects of variability. However, the debiased index showed a significantly weaker 1:1 correlation with the NVA (slopes of $3.7, 4.5,$ and 4.3 in U, L, and S bands, respectively). This distinction appears to signify that VI_{debias} is a more reliable metric for assessing intrinsic variability as it rigorously accounts for measurement

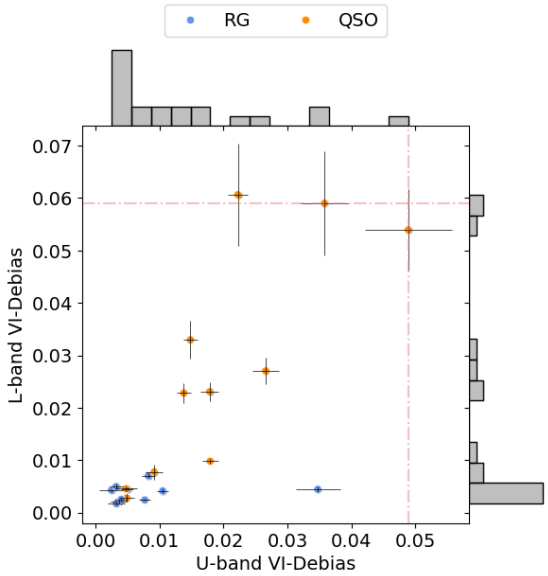

(a) Source in U-band Debiased VI above 3σ: PKS J0730-1141. Source in L-band Debiased VI above 3σ: PKS J0828-3731, PKS J0854+2006.

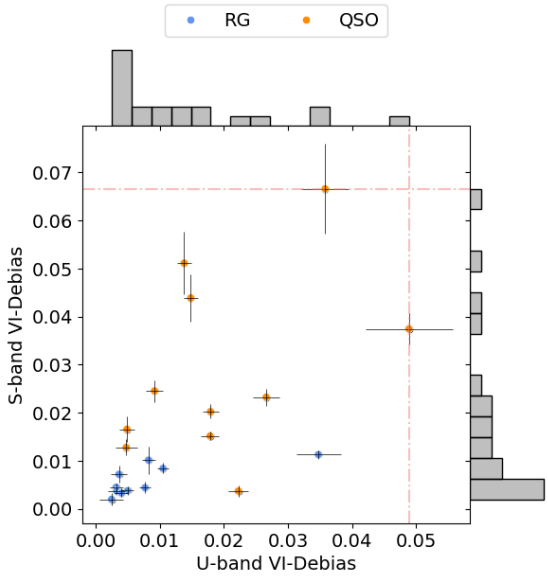

(b) Source in U-band Debiased VI above 3σ: PKS J0730-1141. Source in S-band Debiased VI above 3σ: PKS J0854+2006. Common source above 3σ: None.

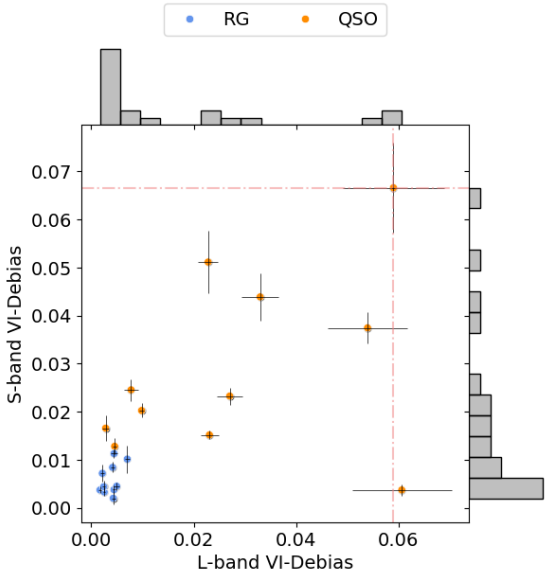

(c) Source in L-band Debiased VI above 3σ: PKS J0828-3731, PKS J0854+2006. Source in S-band Debiased VI above 3σ: PKS J0854+2006. Common sources exceeding 3σ: PKS J0854+2006.

Figure 4.5: Scatter plots of VI_{debias} values for individual calibrator sources in our sample (RGs are plotted in blue, and QSOs are plotted in orange) in a L vs U band, S vs U band, and S vs L band pairwise analysis.

	U-band	L-band	S-band
VI_{Aller}	0.091±0.010	0.061±0.005	0.047±0.006
VI_{Fan}	0.085±0.025	0.065±0.007	0.047±0.009
RMSD	0.050±0.003	0.044±0.002	0.039±0.004
NVA	0.088±0.032	0.069±0.019	0.074±0.027
VI_{debias}	0.014±0.002	0.016±0.002	0.018±0.002

Table 4.6: The average of the VI metrics for each of the three MeerKAT bands from the LTV analysis for our sample of calibrators

uncertainties and is normalized by the mean flux. Consequently, VI_{debias} was selected for a pairwise analysis with VI_{Aller} in the STV analysis in the next section.

Figure 4.6 represents the correlations detailed in Table 4.7, showing correlation plots of the other VI with the NVA variability metric. Each point represents a calibrator source, with RGs typically clustering at the bottom-left of the plots (indicated in blue), while known QSOs generally cluster further up the plots (indicated in orange), exhibiting higher values for all variability metrics. This observed spatial separation of source types in the parameter space provides a compelling visual interpretation that this type of correlation analysis, particularly the distribution of sources within these plots, may be valuable in separating classes of unknown objects, which can then be further classified with additional optical spectroscopy analysis.

4.2 Short-Term Variability Analysis: Phase Calibrator PKS J2152-2828 (MeerKAT UHF)

The light curves used for the STV analysis of the phase calibrator field were created using a tailored data reduction approach with the Madroon pipeline (see Section 3.4). As mentioned in Chapter 3, calibrators are observed intermittently, and we refer to these short, ON-calibrator observation periods as “scans." PKS J2152-2828 had 11 scans over the duration of

	U-band		
X-Y	m$\pm\Delta m$	c$\pm\Delta c$	Red χ^2
NVA-VI_{Aller}	0.798±0.062	0.008±0.002	0.210
NVA-VI_{Fan}	0.850±0.054	0.013±0.002	0.220
NVA-RMSD	1.292±0.070	0.005±0.002	0.161
NVA-VI_{debias}	3.697±0.218	0.008±0.002	0.191

	L-band		
X-Y	m$\pm\Delta m$	c$\pm\Delta c$	Red χ^2
NVA-VI_{Aller}	0.937±0.085	0.001±0.001	0.613
NVA-VI_{Fan}	1.026±0.078	0.003±0.002	0.610
NVA-RMSD	1.409±0.053	0.001±0.000	0.163
NVA-VI_{debias}	4.447±0.243	0.002±0.001	0.329

	S-band		
X-Y	m$\pm\Delta m$	c$\pm\Delta c$	Red χ^2
NVA-VI_{Aller}	1.321±0.115	-0.003±0.002	0.323
NVA-VI_{Fan}	1.505±0.115	-0.003±0.002	0.361
NVA-RMSD	1.708±0.104	-0.006±0.002	0.235
NVA-VI_{debias}	4.312±0.331	-0.004±0.002	0.365

Table 4.7: Correlation between variability metrics, $Y = mX + c$ with reduced χ^2.

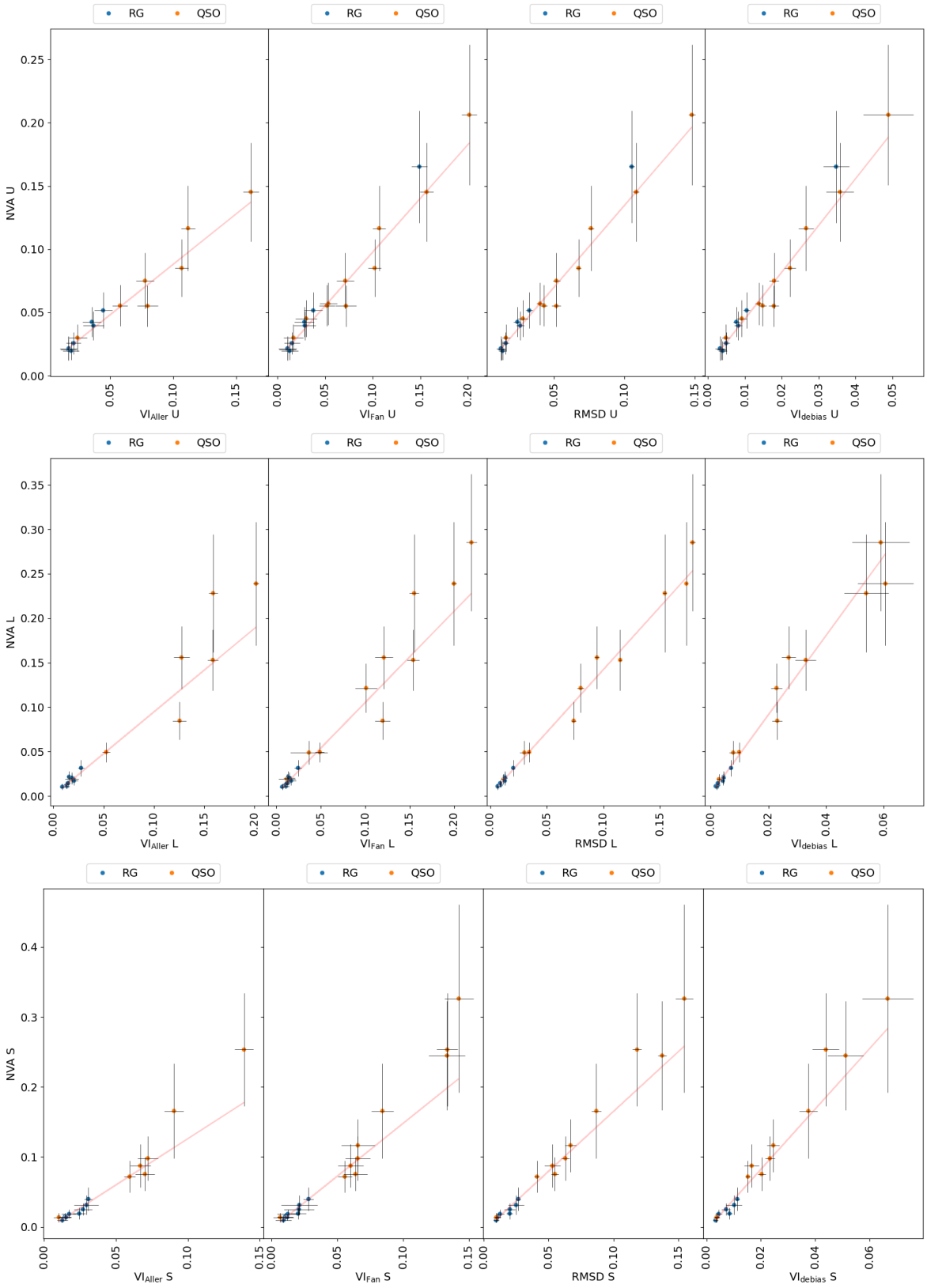

Figure 4.6: Mutual correlation plots of the NVA plotted against the other VI: VI_{Aller}, VI_{Fan}, RMSD, and VI_{debias} for our calibrator sample in the U, L, and S bands. Radio Galaxies (RGs) are plotted in blue, and Quasars (QSOs) are plotted in orange.

the science target observation in the U-band (see Table 3.1). From the 2GC calibrated data, we extracted residual fluxes (see Step 3.4.9) and their corresponding uncertainties for each scan, allowing us to focus on the dynamic changes over time, and plot light curves. Finally, for each scan, statistics were computed for the STV analysis.

We calculated the variability metrics: VI_{Aller} and VI_{debias} (defined in Section 1.5.1) for each scan. VI_{Aller} was chosen as a straightforward measure, reliable for cases of strong flaring or burst-like activity, though sensitive to outliers. VI_{debias}, on the other hand, was chosen for its lack of strong correlation to the NVA (from the LTV VI mutual correlations), and its conservative estimate of intrinsic variability as it corrects for measurement errors. This pairwise statistical analysis of VI for each scan was used to quantitatively analyse the STV of the calibrator.

Furthermore, we grouped the extracted light curves into two radial bins ($r < 0.5^\circ$) and ($0.5^\circ < r < 1.2^\circ$). It should be noted that although the main subject of the variability analysis is the calibrator, the need to discriminate between source intrinsic vs extrinsic variability led us to include other sources in the field. By analysing the variability of sources based on their proximity to the phase centre, we could isolate extrinsic variability contributors such as scintillation, instrumental effects (e.g, primary beam rotation effects that are known to cause amplitude variations), or Direction-Dependent effects. The HPBW of the main lobe is $\approx 1.5^\circ$ at U-band. The radial bins are summarised in Table 4.8. The detection limit for our analysis was 1.33×10^{-4} Jy/beam, based on a 3σ threshold of the image's RMS noise.

4.2.1 Sources within $r < 0.5^\circ$ of the phase centre

Initial examination of the 4 s cadence light curves (e.g, see Figure 3.11) showed rapid fluctuations that were consistent with the characteristics of Interplanetary Scintillation (IPS). As discussed in Section 1.4.1, IPS is an extrinsic variability phenomenon that typically manifests on very short timescales (a few seconds) (Morgan et al., 2017; Thompson et al., 2001). The high sensitivity and wide field-of-view of MeerKAT mean that IPS signatures are expected to be observed. Smirnov et al. (2024) reported that some sources showed rapid twinkling (up to $25-30\%$ variation) on timescales of 8 s in the MeerKAT U-band. Our methodology, which

Radial Bin	Integration Time [s]	Source Count	Flux Density Range [Jy]
$r < 0.5^\circ$	4	8	4.3725 - 0.0377
	16	11	4.3725 - 0.0238
$0.5^\circ < r < 1.2^\circ$	4	15	0.3186 - 0.0371
	16	19	0.3186 - 0.0246

Table 4.8: Summary of source counts and flux ranges for the STV analysis, grouped by radial distance from the phase centre. The table provides the total number of sources, as well as the maximum and minimum fluxes in Janskys (Jy) within each radial bin. Fainter sources are picked up due to the increased integration time.

includes generating High Time Cadence (HTC) images at both 4 s and 16 s, was specifically designed to investigate such rapid variations.

4 s HTC Analysis

1) 4 s Variability Indices vs Median Scan Time

We began by computing VI_{Aller} as given by Equation 1.22 for each scan. We set our threshold of variability as any VI values above 3σ[1]. Figure 4.7a shows VI_{Aller} vs Median Scan Time for the 4 s cadence images, $r < 0.5^\circ$. The dark blue region indicates 1σ, and the lighter blue shows the 3σ (σ is the standard deviation of VI_{Aller}). In Figure 4.7a, there appears to be no variability as all scans fall within 3σ. However, it is noteworthy that the latter scans (at timestamps **21:18, 21:50, 22:23, 22:55**, and **23:28**) tend to deviate more from the mean than previous scans, warranting further investigation. It was also clear that the deviating scans appeared to have large measurement uncertainties except at **22:23**. To explore this, we calculated the debiased VI (VI_{debias}).

As shown in Equation 1.34, and discussed previously, VI_{debias} corrects for measurement errors. Therefore, if the calculated VI_{debias} is much larger than its uncertainty (ΔVI_{debias}), this indicates a well-constrained measurement, implying that any observed variability is

[1] In a normal distribution, $\approx 99.7\%$ of data points lie within 3σ of the mean, making points outside this range rare and significant.

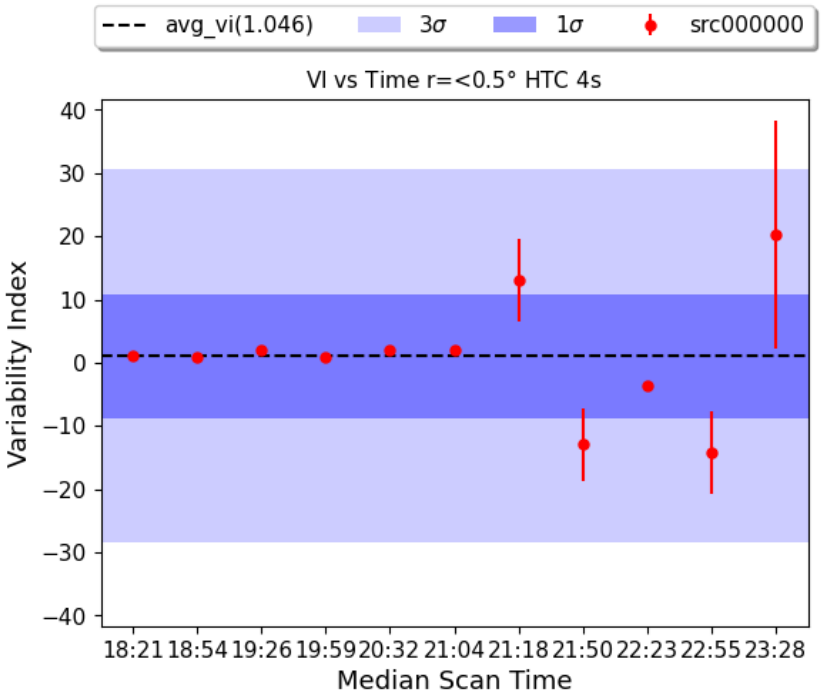

(a) VI_{Aller} vs Time

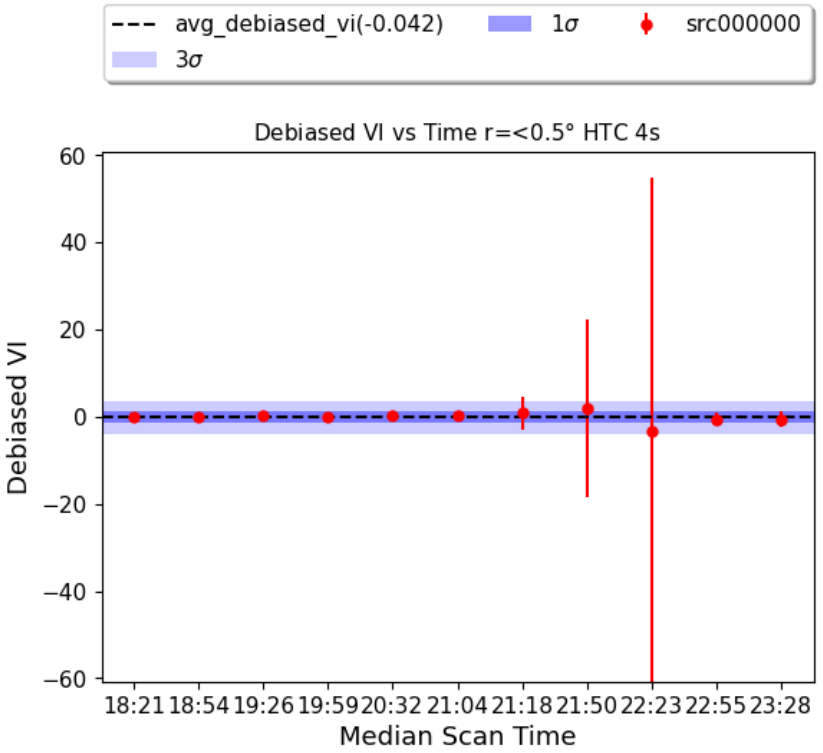

(b) VI_{debias} vs Time

Figure 4.7: The figure shows VI_{Aller} (top) and VI_{debias} (bottom) vs Median Scan Time for PKS J2152-2828 for the 4 s cadence images, $r < 0.5°$. The dark blue region shows 1σ and the lighter blue shows the 3σ (σ is the standard deviation of VI).

likely intrinsic and not just due to measurement errors. On the other hand, if VI_{debias} is comparable to or smaller than ΔVI_{debias}, it might indicate that the observed variability is consistent with measurement uncertainties, and the source may not be significantly variable. Figure 4.7b shows VI_{debias} vs Median Scan Time for the 4 s cadence images, $r < 0.5°$. The dark blue region indicates 1σ, and the lighter blue shows the 3σ (σ is the standard deviation of VI_{debias}). From the figure, we concluded that the latter scans only appeared to deviate from the mean because of their measurement errors (which are comparable/larger than their VI values) and not intrinsic variability.

2) 4 s **Average of Averages and Weighted Average Statistics**

To further substantiate our STV analysis, we computed two additional statistics for the sources within 0.5° of the phase centre. The aim was to understand the phase calibrator's behaviour compared to the other sources. We began by filtering out any scans that are significantly biased. We did this by using the relative error, defined as the ratio of the propagated error on VI to the calculated VI value. This serves as a crucial indicator of uncertainty associated with each variability measurement. By excluding data points with a high relative error (≥ 1), we mitigated the potential impact of uncertain measurements influenced by noise or systematic errors.

The additional statistics we calculated were the **Average of Averages (avg of avg)** and the **Per-Scan Average**, under the hypothesis; if instrumental or systematic errors were influencing the variability parameters calculated, we would then expect all sources within the same radius, including the phase calibrator, to be similarly affected. Therefore, any observed variability in the phase calibrator that is not reflected in the other sources suggests that the variability is intrinsic (real variability in the source) rather than extrinsic (systematic due to measurement errors).

- **Average-of-Averages (avg-of-avg)**

  In Equation 4.1, we calculate the average VI for each source *i*, over the total observation time ($\overline{VI}_i$). We then calculate the average of these individual averages ($VI_{avg\text{-}of\text{-}avg}$), excluding that of the phase calibrator where N is the total number of average VI. By comparing this overall average to the phase calibrator's VI, we could

gauge the general variability behaviour of all sources relative to the calibrator.

$$\mathrm{VI}_{\mathrm{avg\_of\_avg}} = \frac{1}{N}\sum_{i=1}^{N}\overline{\mathrm{VI}}_i \tag{4.1}$$

Figure 4.8 shows the Average-of-Averages (the dotted black line) $\mathrm{VI}_{\mathrm{Aller}}$ (top) and $\mathrm{VI}_{\mathrm{debias}}$ (bottom) vs Median Scan Time. The missing scans from sources within $r < 0.5^\circ$ and the phase calibrator are due to filtering based on the relative error (≥ 1) discussed previously.

Figure 4.8a shows that most sources appear to behave similarly, with their $\mathrm{VI}_{\mathrm{Aller}}$ values falling within 3σ of the avg of avg (dotted line), except for a few outlier scans. The outlier scans and the latter phase calibrator scans noted in the previous section, though deviating from the average behaviour of the other sources (falling outside of 3σ), do not do so uniformly, seemingly indicating that the variability was intrinsic to these sources at these scans. However, as discussed previously, for scans with $\mathrm{VI}_{\mathrm{debias}}$ uncertainties comparable/larger than their values do not indicate true variability but rather measurement errors. Figure 4.8b therefore indicates that the apparent variability of all the scans deviating from the avg of avg can be attributed to measurement errors.

- **Per-Scan Average**

  The second metric is the per-scan average, which represents the average VI per-scan for all sources within the 0.5° radius, excluding the phase calibrator. For the per-scan average, each scan average, $\overline{\mathrm{VI}}_j$ is influenced by the number of valid VI (a weighted average) it contains after filtering out scans with a high relative error (≥ 1). In Equation 4.2, N_j is the number of valid VI measurements in each scan j.

$$\overline{\mathrm{VI}}_j = \frac{1}{N_j}\sum_{i=1}^{N_j}\mathrm{VI}_{i,j} \tag{4.2}$$

  Essentially, this shows how the sources behave in each scan. By comparing the per-scan averages of the sources within this radius to those of the calibrator, we can better understand if any observed variability is consistent across each scan or if it is specific to that calibrator scan. Figure 4.9 shows the Per-Scan $\mathrm{VI}_{\mathrm{Aller}}$ (top) and

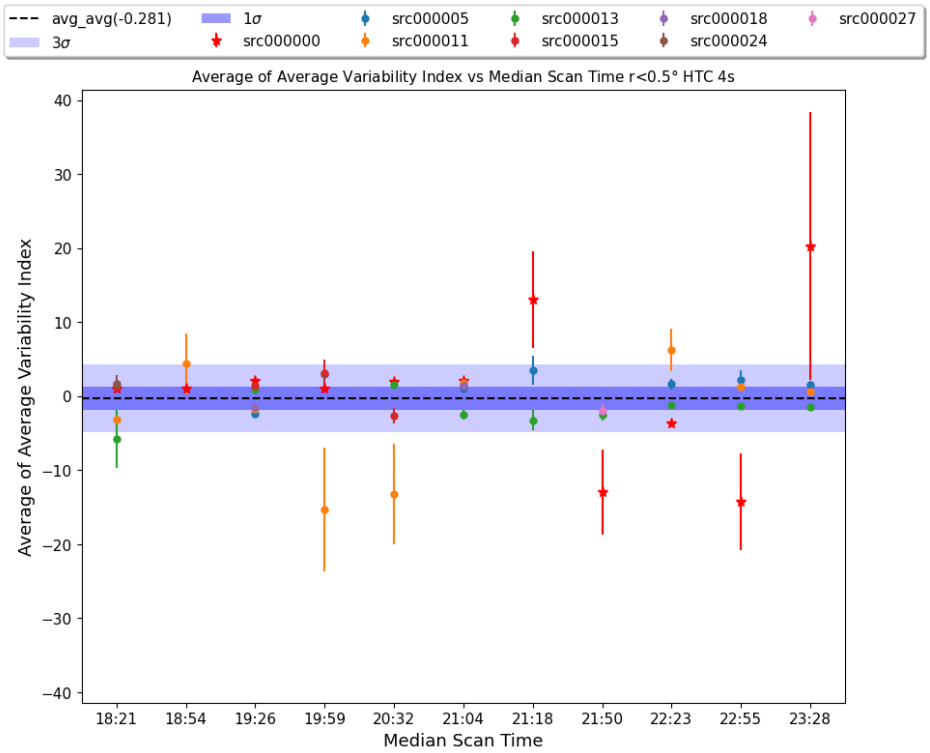

(a) Average-of-Average VI_{Aller}

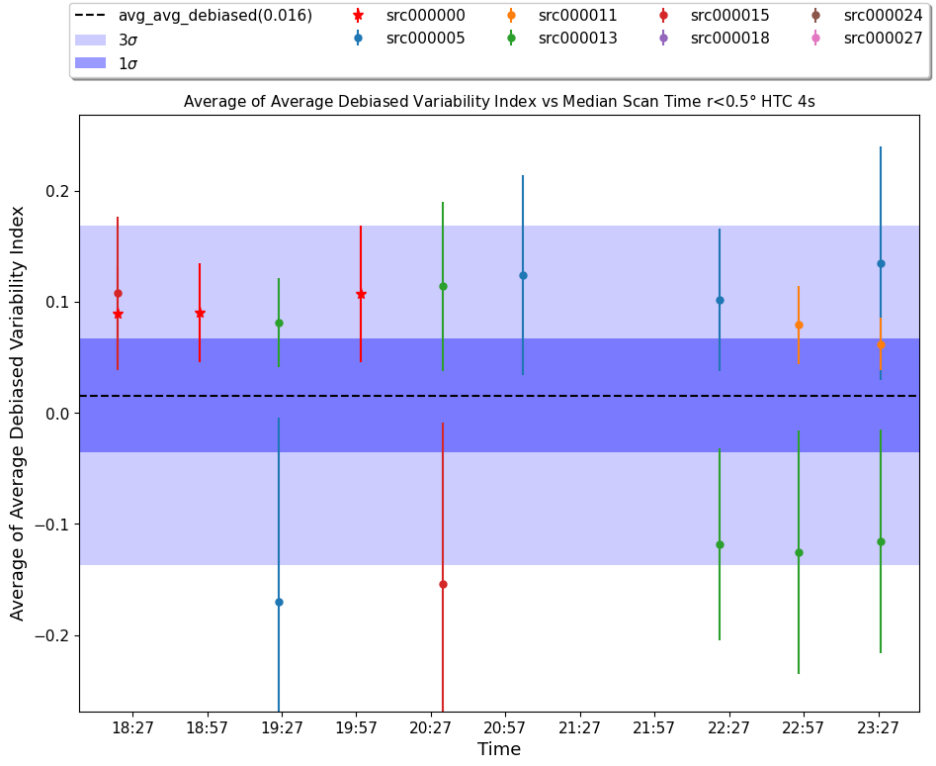

(b) Average-of-Average VI_{debias}

Figure 4.8: The figure shows the Average-of-Averages (the dotted black line) VI_{Aller} (top) and VI_{debias} (bottom) vs Median Scan Time for the 4 s cadence image data, $r < 0.5°$. The dark blue region shows 1σ and the lighter blue shows the 3σ of the avg of avg.

VI_{debias} (bottom) averages of sources within r $< 0.5^{\circ}$ compared to PKS J2152-2828 VI for the 4 s cadence images. Figure 4.9a provides the same information as the other VI_{Aller} plots, where the latter scans of the phase calibrator appear to indicate intrinsic STV. This is not supported by the VI_{debias} (4.9b) plot since those specific scans are all filtered out as scans with high relative errors and thus not exhibiting any intrinsic variability.

These additional statistics are important because they provide a more comprehensive view of the data. The avg of avg helps us understand the collective behaviour of all sources, while the per-scan average gives a more detailed picture of how variability might change over time in each scan, accounting for the contribution of each source. Together, these metrics reinforce our analysis and help ensure that our conclusions of no short-term variability present in the phase calibrator PKS J2152-2828 are robust and well-supported by the data.

16 s **HTC Analysis**

1) 16 s **Variability Indices vs Median Scan Time**

A comparison of the similar plots in Figures 4.7 and 4.10 revealed insights into the variability of the phase calibrator. The latter scans of the phase calibrator that initially appeared to show some variability in the 4 s HTC images exhibited a reduced deviation from the mean of the VI in the 16 s HTC images. This reduction confirmed that the variability observed could be attributed to scintillation effects, which are typically mitigated in longer integration times. In Figure 4.10, all the scans of the phase calibrator fall within 3σ, with one scan at timestamp 22:23 standing out for both VI. However, the presence of the relatively large uncertainty suggested that this variability was not intrinsic to the calibrator but rather influenced by measurement uncertainties.

2) 16 s **Average of Averages and Weighted Average Statistics**

Similar to the 4 s HTC images, we calculated the avg of avg and per-scan average (weighted average) of the sources within the 0.5° radius and compared these to the phase calibrator.

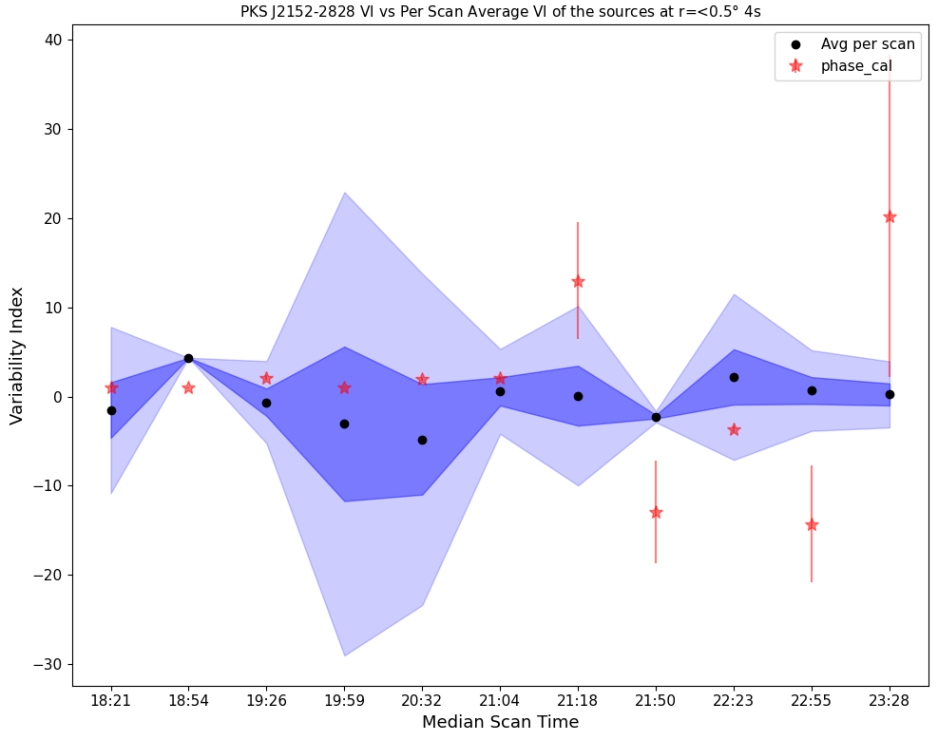

(a) Per Scan Average VI_{Aller}

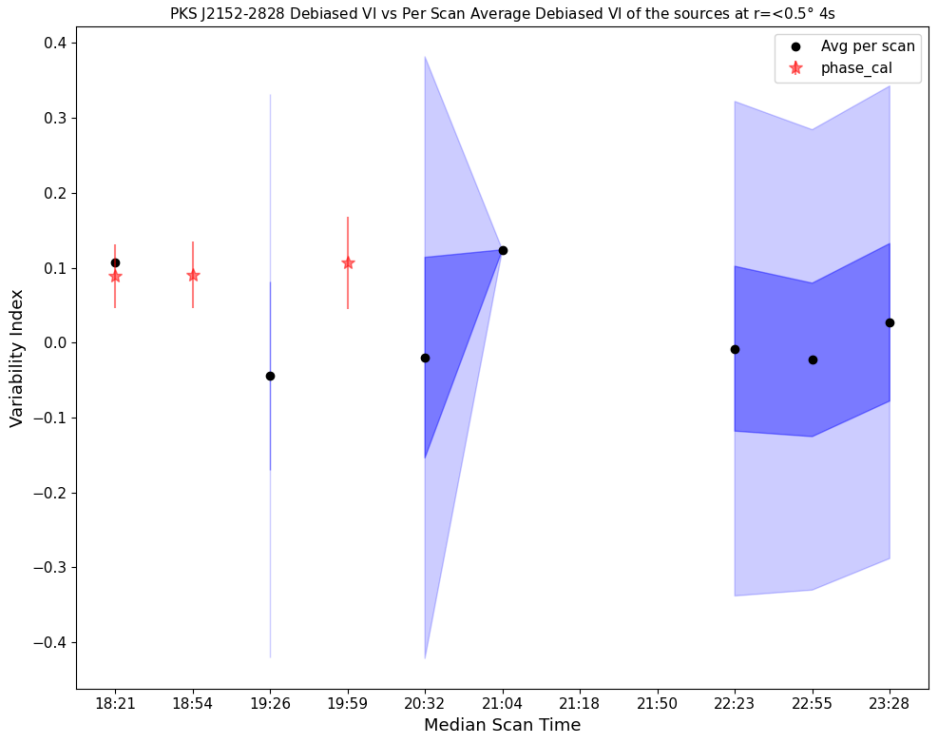

(b) Per Scan Average VI_{debias}

Figure 4.9: The figure shows the Per-Scan VI_{Aller} (top) and VI_{debias} (bottom) averages of sources within $r < 0.5^{\circ}$ compared to PKS J2152-2828 VI for the 4 s cadence images. The dark blue region shows 1σ and the lighter blue shows the 3σ (standard deviation of per-scan average VI).

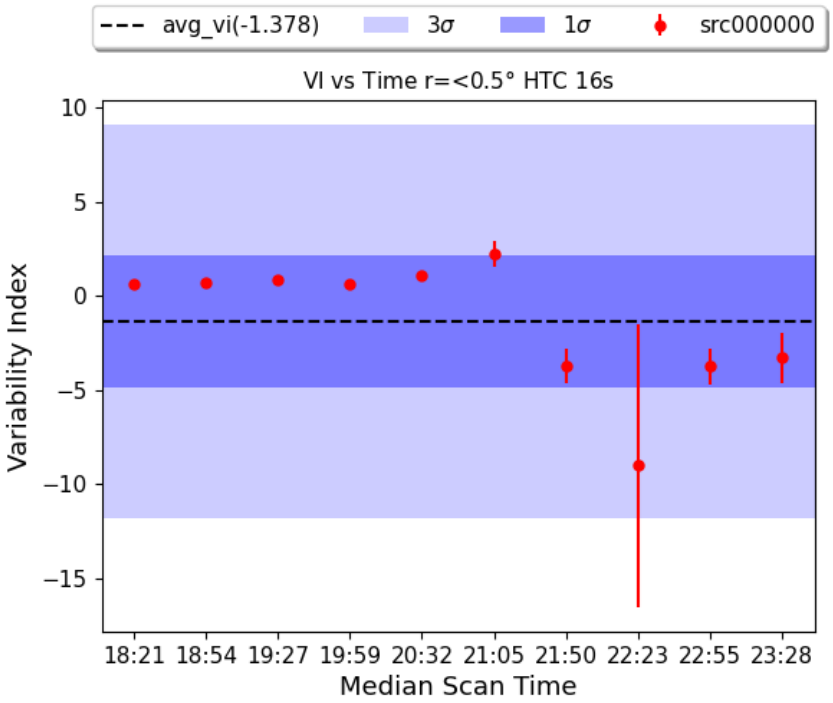

(a) VI_{Aller} vs Time

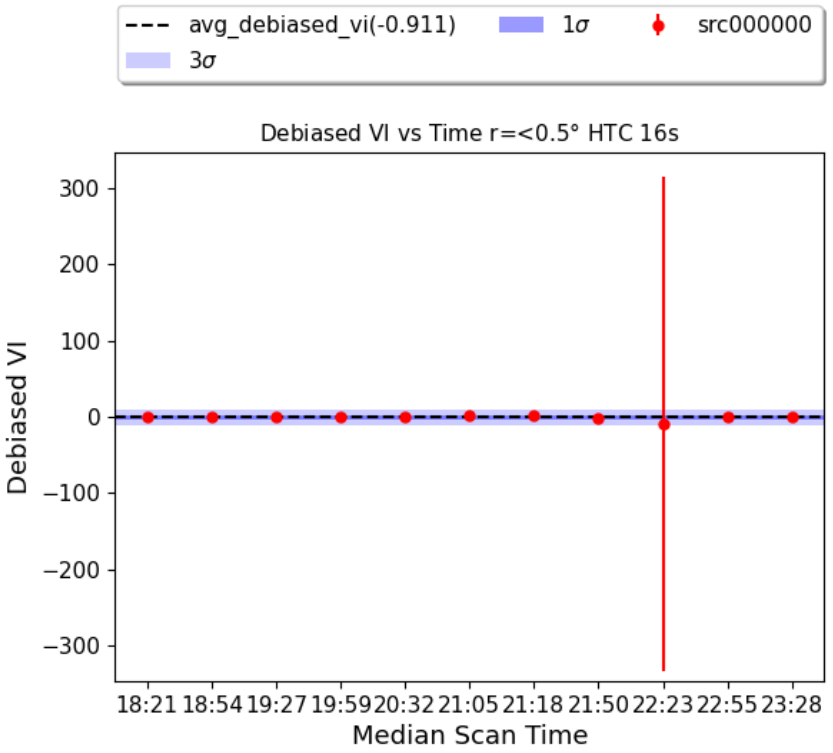

(b) VI_{debias} vs Time

Figure 4.10: The figure shows VI_{Aller} (top) and VI_{debias} (bottom) vs Median Scan Time for PKS J2152-2828 for the 16 s cadence images, $r < 0.5°$. The dark blue region shows 1σ and the lighter blue shows the 3σ (standard deviation of VI).

- **Average-of-Averages**

  The missing scans of sources within $r < 0.5^\circ$ and the phase calibrator in Figure 4.11 are due to filtering based on the relative error (≥ 1) discussed previously. In figure 4.11a, most sources appear to behave similarly, with their VI_{Aller} falling within 3σ of the average of averages, except for a few outlier scans. We calculated the same avg of avg statistic for VI_{debias} to rule out variability caused by measurement errors of the scans falling outside of 3σ. Figure 4.11b shows that the phase calibrator scans fall within our threshold. Two scans deviating from the avg of avg have VI_{debias} values comparable to their uncertainties. indicating that the apparent variability was due to measurement errors.

- **Per-Scan Average**

  We calculated the per-scan average and compared it to the VI per scan of the calibrator to understand if any observed variability is consistent across the field or if it is specific to the calibrator. As can be seen in figure 4.12, many per-scan average values are missing because of the filtering done based on the relative error (≥ 1). In Figure 4.12a, the phase calibrator seems to have consistent behaviour with that of the other sources (VI_{Aller} falls within 3σ). For the per-scan average of VI_{debias} (Figure 4.12b), no conclusions were drawn as the standard deviation could not be computed for most of the scans.

4.2.2 Sources within $0.5^\circ < r < 1.2^\circ$ of the phase centre

We conducted a similar analysis on the sources within the radius between $0.5^\circ < r < 1.2^\circ$. This range was chosen to stay with the primary beam ($\approx 1.5^\circ$ at U-band) and also ensure that the sources analysed were not affected by the potential artifacts and distortions present in the outer regions of the field. Having established that VI_{debias} is a more reliable variability index due to its consideration of measurement errors, we used it exclusively for this analysis. Even though instrumental effects can worsen further away from the phase centre, this analysis is crucial for several reasons:

i) **Verifying Apparent Variability**

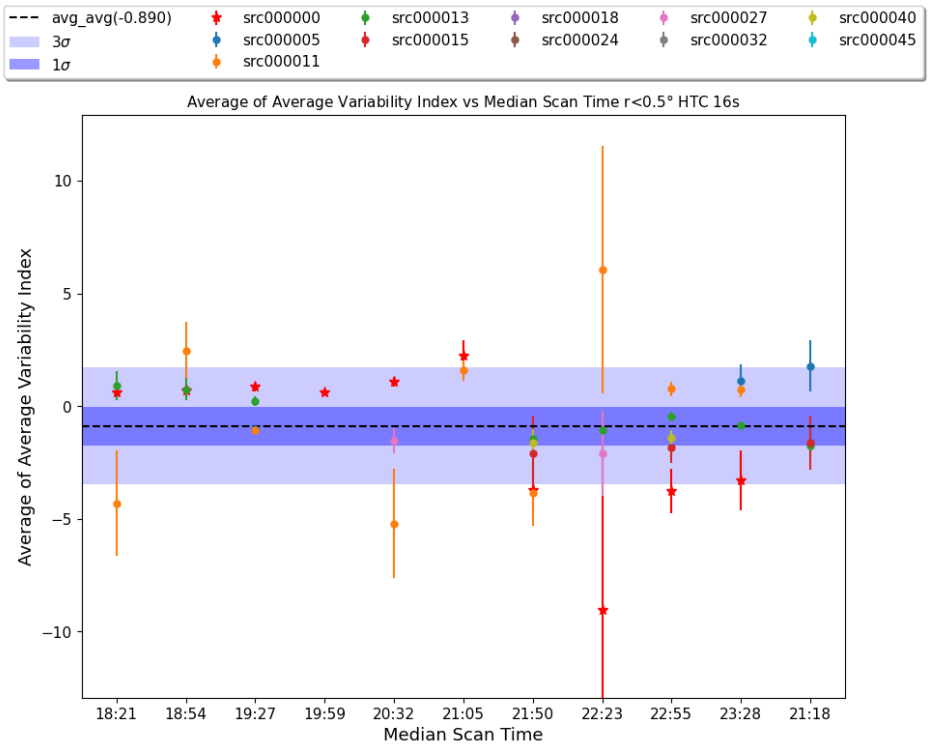

(a) Avg of Avg VI_{Aller}

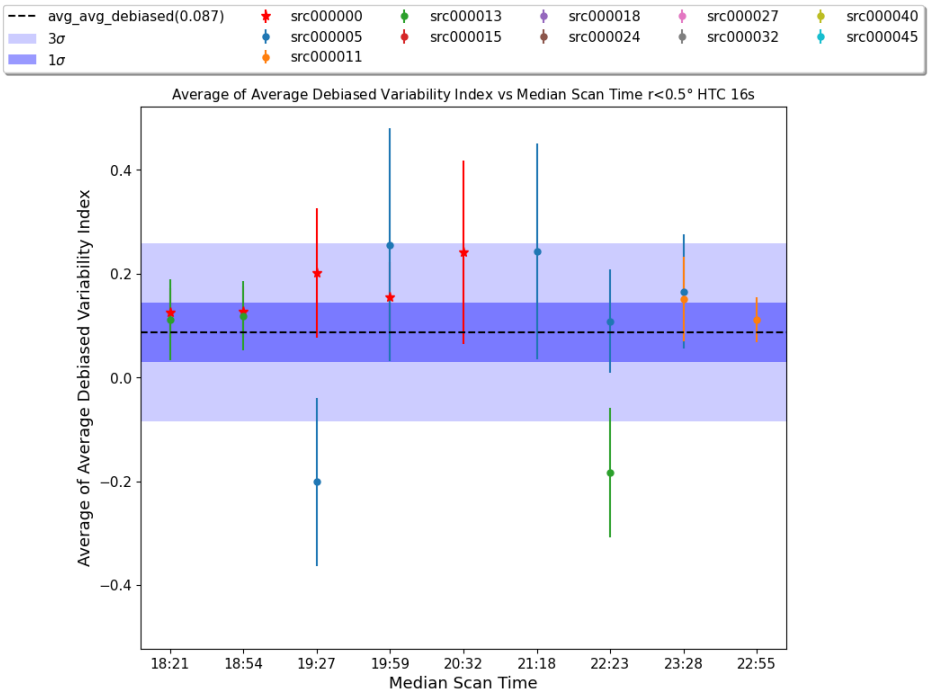

(b) Avg of Avg VI_{debias}

Figure 4.11: The figure shows the Average-of-Averages (the dotted black line) VI_{Aller} (top) and VI_{debias} (bottom) vs Median Scan Time for the 16 s cadence image data, $r < 0.5°$. The dark blue region shows 1σ and the lighter blue shows the 3σ of the avg of avg.

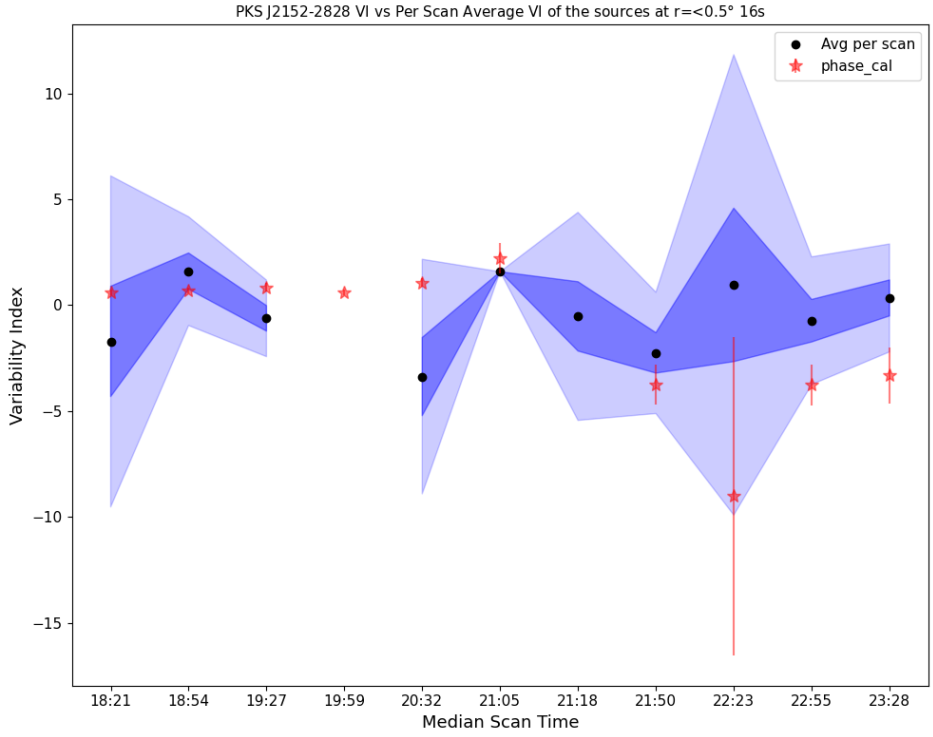

(a) Per-Scan Average VI_{Aller}

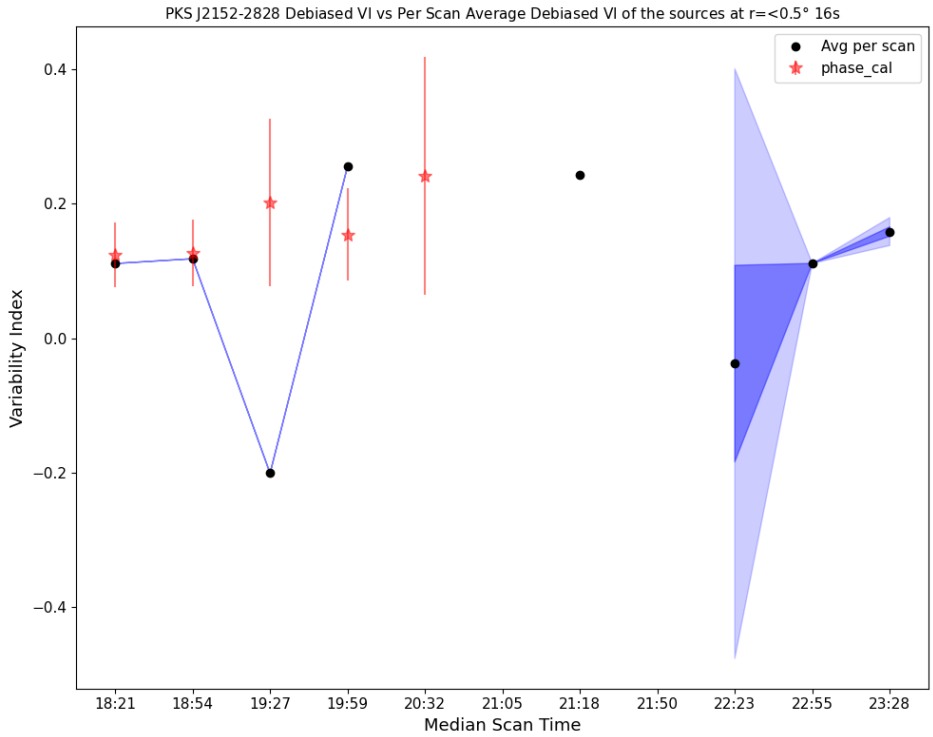

(b) Per-Scan Average VI_{debias}

Figure 4.12: The figure shows the per-scan VI_{Aller} (top) and VI_{debias} (bottom) averages of sources within $r < 0.5^{\circ}$ compared to PKS J2152-2828 VI for the 16 s cadence images. The dark blue region shows 1σ and the lighter blue shows the 3σ (standard deviation of per-scan average VI).

If apparent variability was detected in the phase calibrator within the initial r$< 0.5^\circ$ radius, this extended analysis would help determine whether the variability was intrinsic. If similar variability was observed in sources further from the phase centre, it could indicate that instrumental or calibration errors were causing the variability rather than intrinsic factors. In our case, the calibrator scans that seemed variable exhibit corresponding similar behaviour in the sources within the 0.5° to 1.2° radius as seen in Figure 4.14a and 4.14b. Those that do not in 4.14b have comparable VI and uncertainties. Thus, we can conclude that the apparent variability of these calibrator scans was not intrinsic.

ii) **Gauging Calibration and Cleaning Quality**

This analysis allows us to evaluate the effectiveness of the calibration and cleaning processes. Notably, we observed that the sources within the0.5° to 1.2° radius exhibited a more constrained average variability parameter behaviour (less deviation from the average of averages or weighted mean per scan) as compared to the sources closer to the phase centre (Figure 4.13). We attribute this to two factors: (i) the sources further out are fainter and thus were better deconvolved/cleaned, and (ii) the sources near the calibrator were affected by deconvolution artifacts from the calibrator cleaning (a very bright source), which left residual artifacts during imaging (see Figure 3.10). This extended analysis provides a more comprehensive understanding of variability behaviour across the field and ensures the robustness and accuracy of our conclusions regarding PKS J2152-2828's STV.

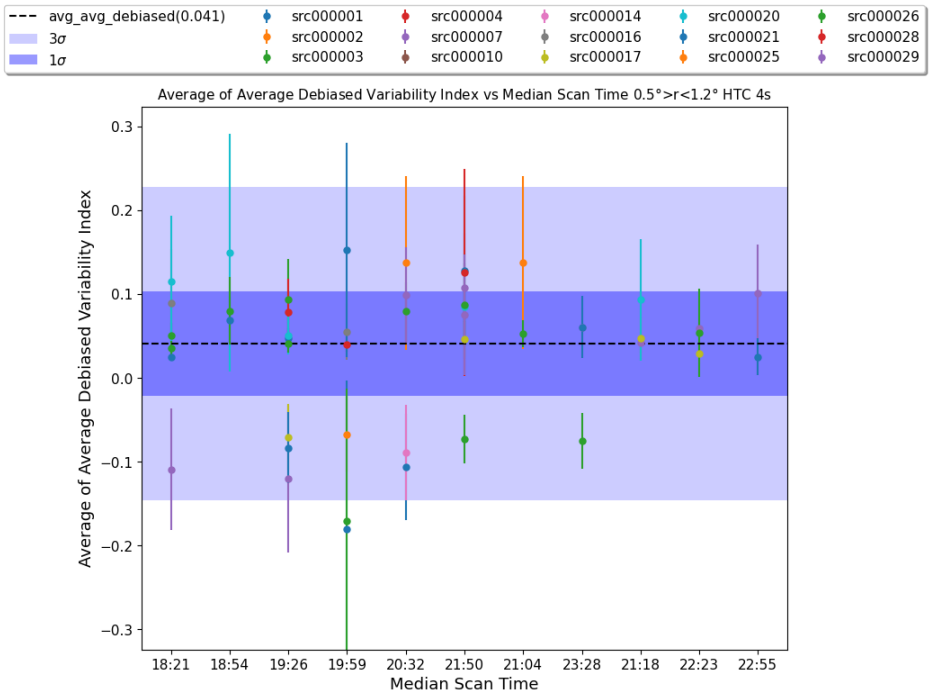

(a) Avg of Avg VI_{debias}

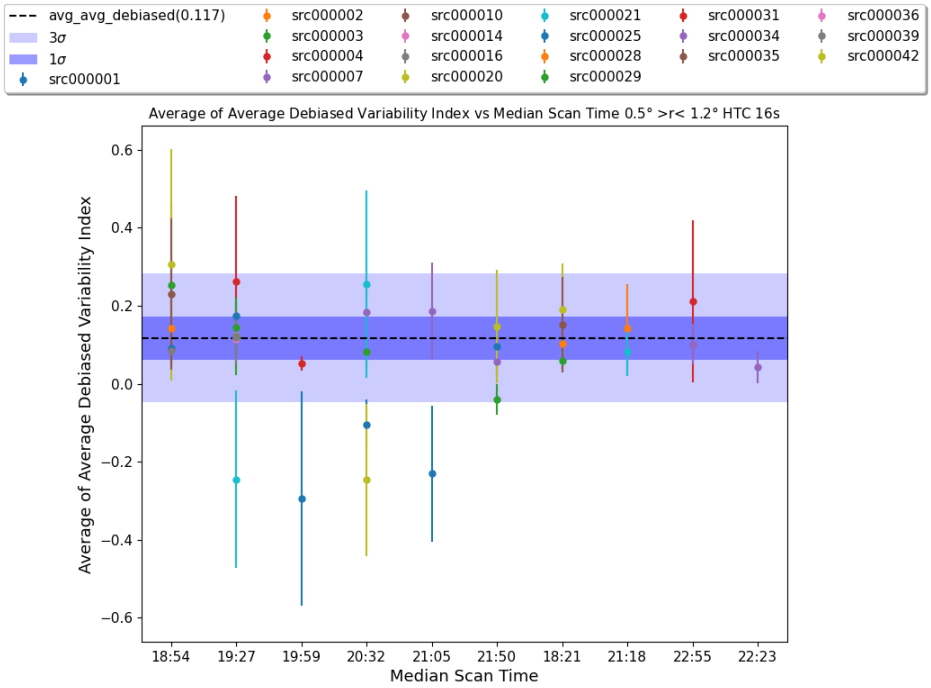

(b) Avg of Avg VI_{debias}

Figure 4.13: The figure shows the Average-of-Averages (the dotted black line) VI_{Aller} (top) and VI_{debias} (bottom) vs Median Scan Time for the 4 s and 16 s cadence image data within $0.5^\circ < r < 1.2^\circ$. The dark blue region shows 1σ and the lighter blue shows 3σ of the avg of avg.

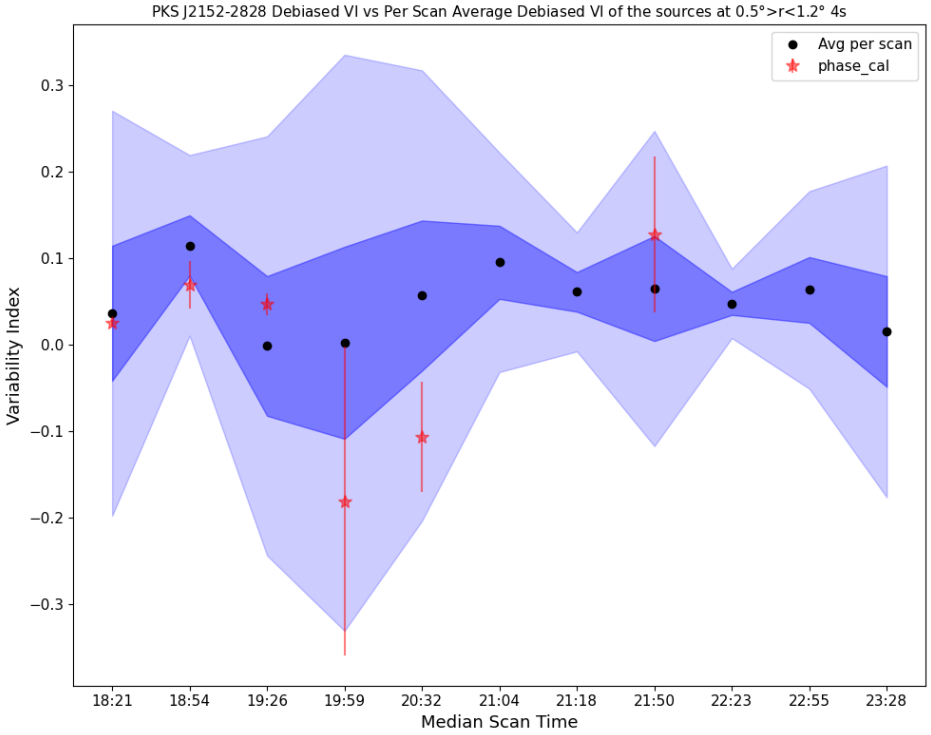

(a) Per-Scan Avg VI_{debias}

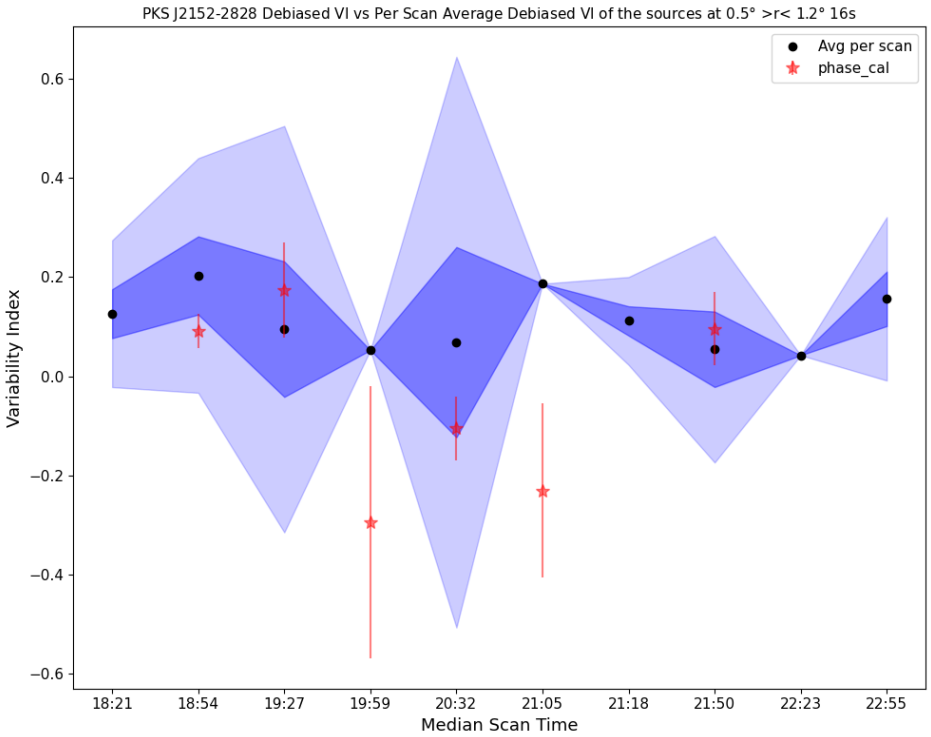

(b) Per-Scan Avg VI_{debias}

Figure 4.14: The figure shows the Per-Scan Average vs Median Scan Time for the 4 s and 16 s cadence image data within $0.5^\circ < r < 1.2^\circ$. The dark blue region shows 1σ and the lighter blue shows 3σ of per-scan average VI_{debias}.

4.3 Summary

In this chapter, we fulfilled our second objective to conduct a comprehensive flux stability analysis of a sample of southern sky calibrators observed by MeerKAT. This was done in two parts: Long-Term Variability (LTV) and Short-Term Variability (STV) analyses.

The LTV analysis was conducted over approximately two years for the three MeerKAT bands, providing crucial insights into the flux stability of our calibrator sample. We calculated multiple VI that provided complementary perspectives on variability in our analysis: VI_{Aller}, VI_{Fan}, NVA, RMSD, and VI_{debias}. The calibrators **PKS J0730-1141** in the U-band, and **PKS J0854+2006** in the L- and S-band showed the largest sustained fluctuations over the two-year monitoring period. We also performed a pair-wise analysis of VI for each of the three MeerKAT bands (see Figures 4.1 - 4.5) with the significant variability threshold set at 3σ. The key finding was the absence of calibrators exhibiting significant variability at frequencies < 1.283 GHz across the majority of our sample. However, the well-known blazar **PKS J0854+2006** (see known information on its variability in Section 2.1.1), consistently exhibited significant variability at frequencies greater than 1.283 GHz, confirming its classification as a variable source. Additionally, from our mutual correlation plots of the variability metrics in Figure 4.6, a distinct source clustering pattern was visually evident: Quasars (QSOs) generally exhibited higher variability metrics compared to Radio Galaxies (RGs).

The Short-Term Variability (STV) analysis was conducted on the phase calibrator PKS J2152-2828 over one observation period ($\approx$ 8 hours), consisting of eleven 2 minute scans. Our analysis was conducted at two radii: 0.5° and between 0.5° to 1.2° of the phase centre to discriminate between source intrinsic and extrinsic variability. We set our threshold for potential scan variability to be a VI value exceeding 3σ and calculated the variability metrics: VI_{Aller} and VI_{debias} for each scan. Initially, the latter calibrator scans at the median times: 21:18, 21:50, 22:23, 22:55, and 23:28 showed some potential variability. Through the pairwise analysis of VI_{Aller} and VI_{debias}, including the Average-of-Averages (Equation4.1) and the Per-scan average (4.2) statistics, we concluded the the apparent variability was due to measurement errors. Additionally, the generation and analysis at 4 s and 16 s, HTC imag-

ing confirmed that the initial rapid fluctuations in the calibrator light curve (see Figure 3.11) were consistent with extrinsic effects (IPS) and not intrinsic to the source. Therefore, we concluded that PKS J2152-2828 exhibited no significant STV, confirming its reliability as a phase calibrator for similar duration observations.

Chapter 5

Conclusions and Future Work

The objectives of this work were two-fold: perform a flux stability analysis of a sample of southern sky calibrators observed by MeerKAT and characterise these calibrators via source modeling. The original sample of calibrators observed by MeerKAT to date consists of approximately 100 sources. We created a sample of 33 calibrators via a selection of sources observed in all three MeerKAT bands (U-band, L-band, and S-band) with at least 4 flux density measurements. The known properties of each calibrator are discussed in Section 2.1.1, and their distribution in the sky is illustrated in Figure 2.1. Source modeling was performed by creating polynomial spectral models using the Specfit package[1]. We found that 26% of the calibrators had a peak, while 15% had a trough in their spectra, and 59% were fit with a linear power law. This analysis provides essential data for high-precision calibration with MeerKAT, aiming to significantly improve the reliability and accuracy of astronomical observations across multiple frequency bands. Furthermore, the classification of calibrators into distinct spectral types offers valuable insights into their underlying astrophysical properties, which can aid in distinguishing and separating classes of unknown radio objects in broader astronomical surveys.

For the flux stability analysis, we investigated Long-Term Variability (LTV), ≈ 2 years and Short-Term Variability (STV), an ≈ 8 hour observation. The LTV analysis was carried out for the years 2021-2023 in the U-band, 2020-2022 in the L-band, and 2022-2023 in the

[1] https://github.com/tmolteno/specfit

S-band. To investigate the potential long-term variability of these sources, we extracted the variability metrics as discussed in detail in Section 4.1.1. The LTV light curves are presented in appendix B. The calibrators **PKS J0730-1141** in the U-band, and **PKS J0854+2006** in the L- and S-band showed the largest sustained fluctuations over the two-year monitoring period. It is worth noting that PKS J0730-1141 is classified as a quasar (QSO) with Kellermann et al. (1998) reporting that the source's substructure revealed a jet with a $\geq 90^{\circ}$ bend. PKS J0854+2006 is a well-studied BL Lac object with a possible brightening and dimming 12-year cycle (Hovatta et al., 2008). Their known properties are summarised in Sections 2.1.1 and 2.1.1 respectively. We also performed a pairwise analysis of the variability metrics for each of the three MeerKAT bands. We set the threshold for a significantly variable source as one whose VI value exceeded 3σ, where σ is the standard deviation of the variability parameter under consideration. No calibrator sources from our sample showed any considerable variability at frequencies $< 1.283\,\mathrm{GHz}$, while the source **PKS J0854+2006** exhibited variability at frequencies $> 1.283\,\mathrm{GHz}$. Therefore, we concluded that PKS J0854+2006 exhibits LTV. It is worth noting that the LTV pairwise analysis holds the potential to distinguish sources that are genuinely broadband variable from those whose variation is confined to a single frequency range, which could help constrain physical mechanisms (e.g., synchrotron self-absorption). Additionally, from our mutual correlation plots of the variability metrics in Figure 4.6, a distinct source clustering pattern was visually evident: Quasars (QSOs) generally exhibited higher variability parameters compared to Radio Galaxies (RGs). This clustering, while not quantitatively validated with a full statistical test in this study, strongly suggests that such variability analysis could be a useful tool for initially separating classes of unknown radio objects. Subsequent optical spectroscopy could then be employed for more definitive classification, potentially revealing distinct variability characteristics among QSO subclasses (e.g., flat-spectrum radio quasars, high optical polarisation quasars) that are known to exhibit diverse variability behaviours.

The STV analysis began with a data reduction process where we flagged, calibrated, imaged, and extracted light curves for the MeerKAT-observed calibrator datasets summarised in Table 3.1. We performed STV for the phase calibrator PKS J2152-2828 in Section 4.2. Our analysis was conducted at two radii: 0.5° and between 0.5° to 1.2° of the phase cen-

tre to discriminate between source intrinsic and extrinsic variability. We set our threshold for potential scan variability to be a VI value exceeding 3σ and calculated the variability metrics: VI_{Aller} and VI_{debias} for each scan. Initially, the latter calibrator scans at the median times: 21:18, 21:50, 22:23, 22:55, and 23:28 showed some potential variability. Through the pairwise analysis of VI_{Aller} and VI_{debias}, including the Average-of-Averages (Equation4.1) and the Per-scan average (4.2) statistics, we concluded the the apparent variability was due to measurement errors. Additionally, the generation and analysis at 4 s and 16 s, HTC imagingconfirmed that the initial rapid fluctuations in the calibrator light curve (see Figure 3.11) were consistent with extrinsic effects (IPS) and not intrinsic to the source. We therefore concluded that PKS J2152-2828 exhibited no significant STV, confirming its reliability as a phase calibrator for similar duration observations ($\approx$ 8 hours).

It is essential to acknowledge the critical methodological limitations that may impact our conclusion that PKS J2152-2828 exhibits no STV. Our STV analysis, which relies on residual fluxes (DATA - MODEL) extracted from the imaging process, inherently assumes the accuracy of the subtracted deep sky model. Any inaccuracies in this model could potentially influence the derived variability results. Furthermore, the extensive deconvolution process for very bright calibrators, such as PKS J2152-2828, is prone to introducing residual deconvolution artifacts. These artifacts were observed to particularly affect sources close to the phase centre (within 0.5°), potentially influencing their measured variability.

5.1 Future Work

- An extension of the comprehensive spectral characterization conducted in Section 2.2.1 to the full MeerKAT calibrator catalog ($\approx$ 100 sources) would provide a more comprehensive and representative understanding of the spectral properties across the entire calibrator population, thereby addressing potential biases inherent in a limited sample.

- Future work should also extend the Long-Term Variability analysis to the remaining calibrator sources observed by MeerKAT. The original sample of calibrators is $\approx$ 100 sources. Developing a pipeline to conduct both LTV and STV for all these sources

would be beneficial for a long-term monitoring program of the calibrator sources used to characterize MeerKAT.

- Future work should extend the Short-Term Variability analysis to the remaining reduced data for the MeerKAT-observed calibrator datasets summarized in Table 3.1 to broaden our understanding of STV across the sample. The calibrated images are presented in Appendix A. The data reduction and analysis of one measurement set takes a long time, considering that these are calibrator fields with very bright sources that are not easy to clean.

- Although we concluded that PKS J2152-2828 showed no short-term variability in our analysis, this variability analysis was carried out on the residual flux (DATA-MODEL) of the source (see Section 3.4.12). This was done under the assumption that the subtracted deep sky model was accurate. Thus, future work should further investigate the use of this technique to validate its impact on STV conclusions.

Appendix A

L-BAND images

In this section, we present the first-generation calibrated image for the primary calibrator PKS J1939-6342 in the MeerKAT L-Band. We also present the first and second-generation calibrated images of the phase calibrators PKS J2152-2828 and PKS J1008+0730 in the MeerKAT L-Band. These were produced after following the data processing steps in Chapter 3 up to the final imaging step in Section 3.4.5.

A.1 PKS J1939-6342

The image produced after the first-generation calibration of the flux calibrator PKS J1939-6342 is shown in Figure A.1a. Figure A.1b shows the residual image. Second-generation calibration was not conducted since the image quality was good with no cleaning artifacts. The 2D Gaussian fit on a region centered on the source revealed a compact radio source centered at RA 19:39:25.03, Dec -63:42:45.70 with a peak intensity of 14.66 Jy/beam and an integrated flux of 14.61 Jy. The extracted angular size of the source is $8.60''$ along its major axis and $5.14''$ along its minor axis.

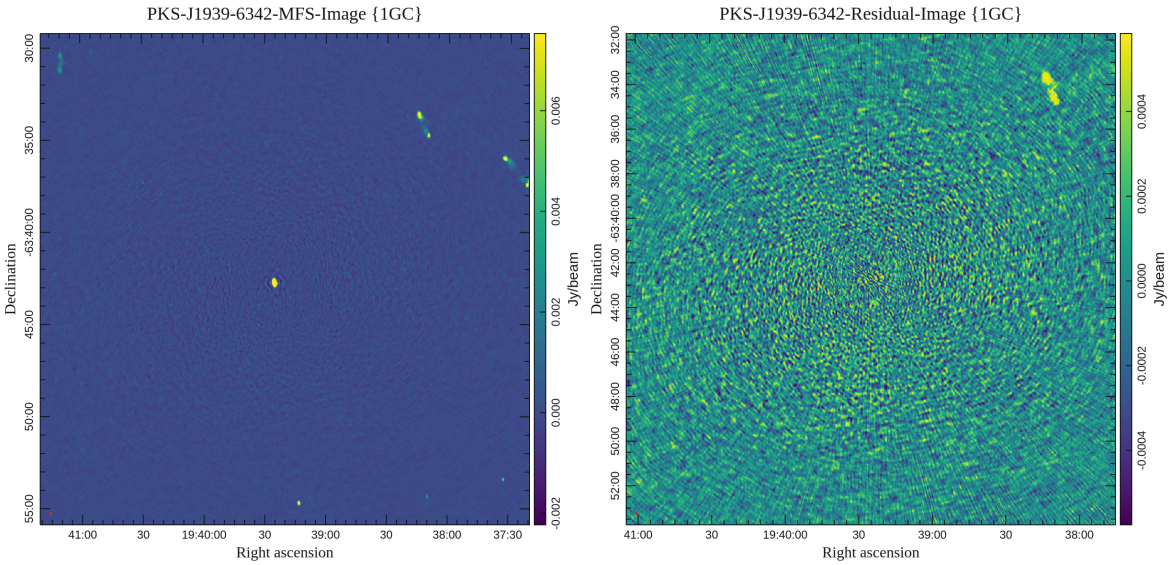

(a) PKS J1939-6342

(b) PKS J1939-6342 residual

Figure A.1: MFS and Residual Images of the flux calibrator PKS J1939-6342 after the 1st generation calibration in the L-band. From Figure A.1a we notice that the image does not have pronounced cleaning artifacts and faint sources are picked up. The residual image in Figure A.1b shows no over-cleaning (no negative holes).

A.2 PKS J2152-2828

The image produced after the first-generation calibration of the phase calibrator PKS J2152-2828 is shown in Figure A.2a. Figure A.2b shows the residual image. The 2D Gaussian fit on a region centered on the source revealed a compact radio source centered at RA 21:52:03.78, Dec -28:28:29.01 with a peak intensity of 2.87 Jy/beam and an integrated flux of 2.97 Jy. The source extracted angular size is 6.76″ along its major axis and 5.36″ along its minor axis.

In the second-generation image in Figure A.3a, the bright PSF around the calibrator has been reduced, and the faint sources close to the calibrator are clearly visible.

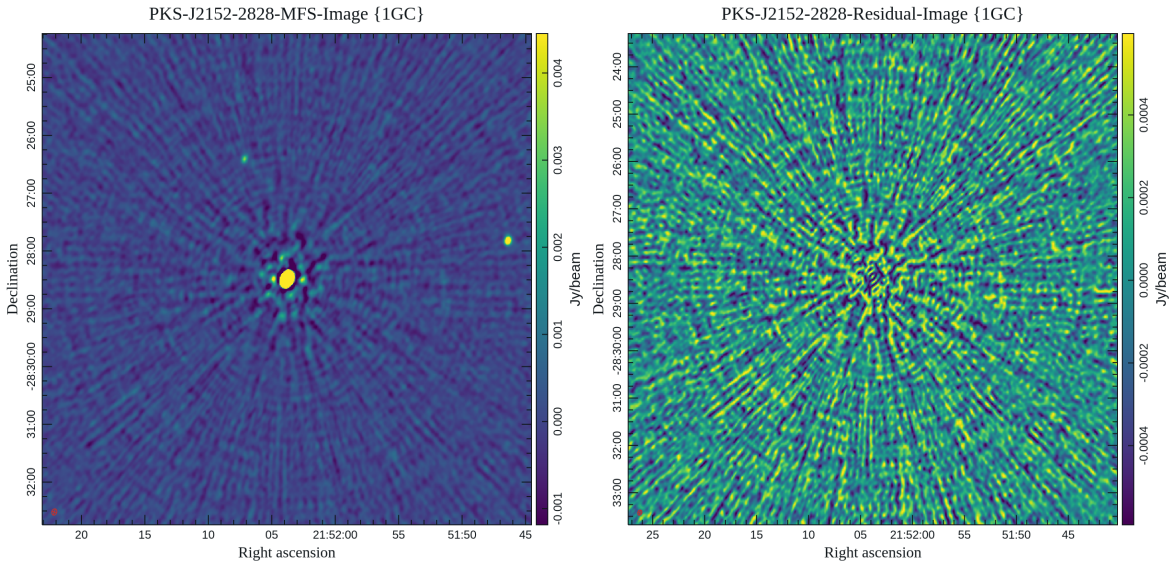

(a) PKS J2152-2828

(b) PKS J2152-2828 residual

Figure A.2: MFS and Residual Images of the phase calibrator PKS J2152-2828 after the 1st generation calibration in the L-band. From Figure A.2a, we can see that the bright PSF around the calibrator is poorly cleaned. The residual image in Figure A.2b confirms that no over-cleaning occurred (no negative holes).

A.3 PKS J1008+0730

The image produced after the first-generation calibration of the second phase calibrator PKS J1008+0730 is shown in Figure A.4a. Figure A.4b shows the residual image. The 2D Gaussian fit on a region centered on the source revealed a compact radio source centered at RA 10:08:00.02, Dec 7:30:16.60 with a peak intensity of 9.94 Jy/beam and integrated flux of 10.12 Jy. The source extracted angular size is 15.04″ along its major axis and 11.50″ along its minor axis. In the second generation image in Figure A.5a, the bright PSF around the calibrator has been reduced with the faint sources to the southeast of the calibrator clearly visible.

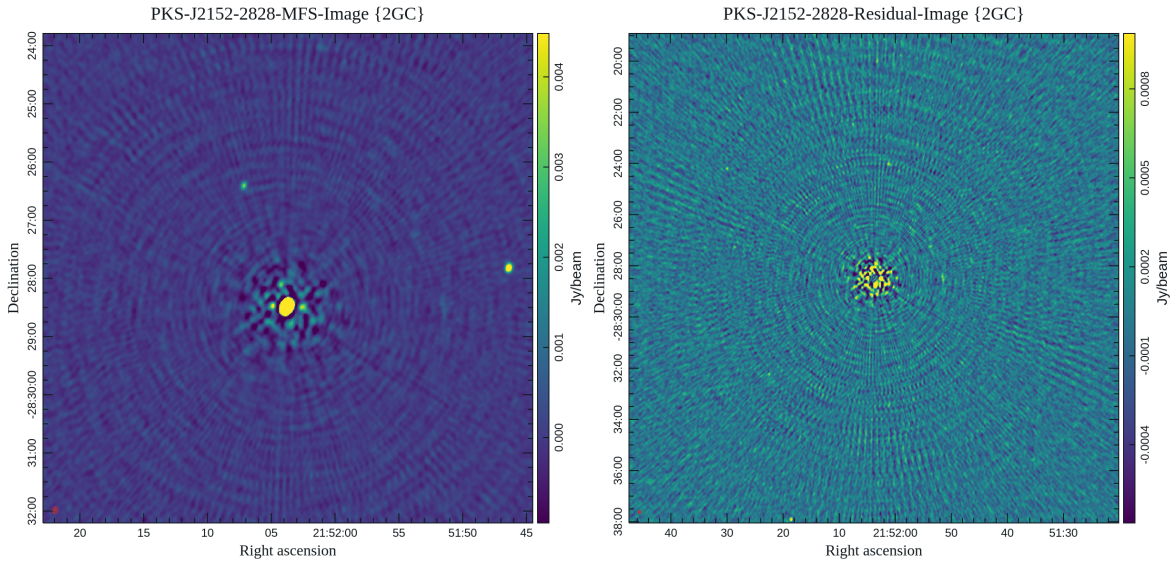

(a) PKS J2152-2828

(b) PKS J2152-2828 residual

Figure A.3: MFS and Residual Images of the phase calibrator PKS J2152-2828 after 2nd generation calibration in the L-band. In Figure A.3a, we note that the bright PSF around the calibrator has been reduced and the faint sources close to the calibrator are clearly visible. The residual image in Fig.(A.3b) indicates that some degree of over-cleaning occurred (negative holes).

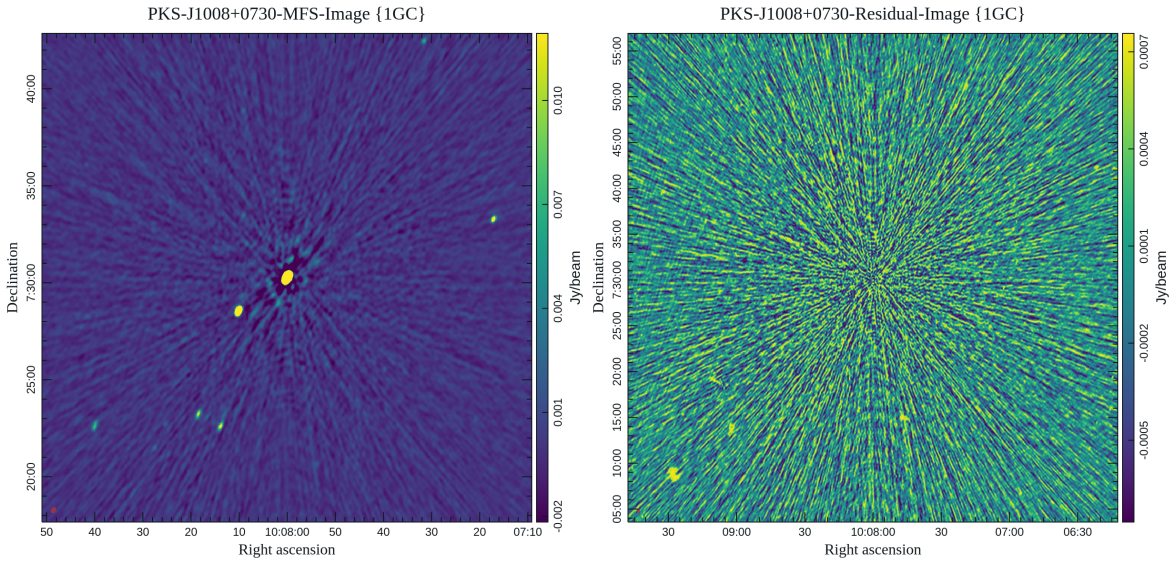

(a) PKS J1008+0730

(b) PKS J1008+0730 residual

Figure A.4: MFS and Residual Images of the phase calibrator PKS J1008+0730 after the 1st generation calibration in the L-band. From Figure 3.8a, we note that the bright PSF around the calibrator has not been cleaned well. The residual image in Figure A.4b indicates that no over-cleaning occurred (no negative holes).

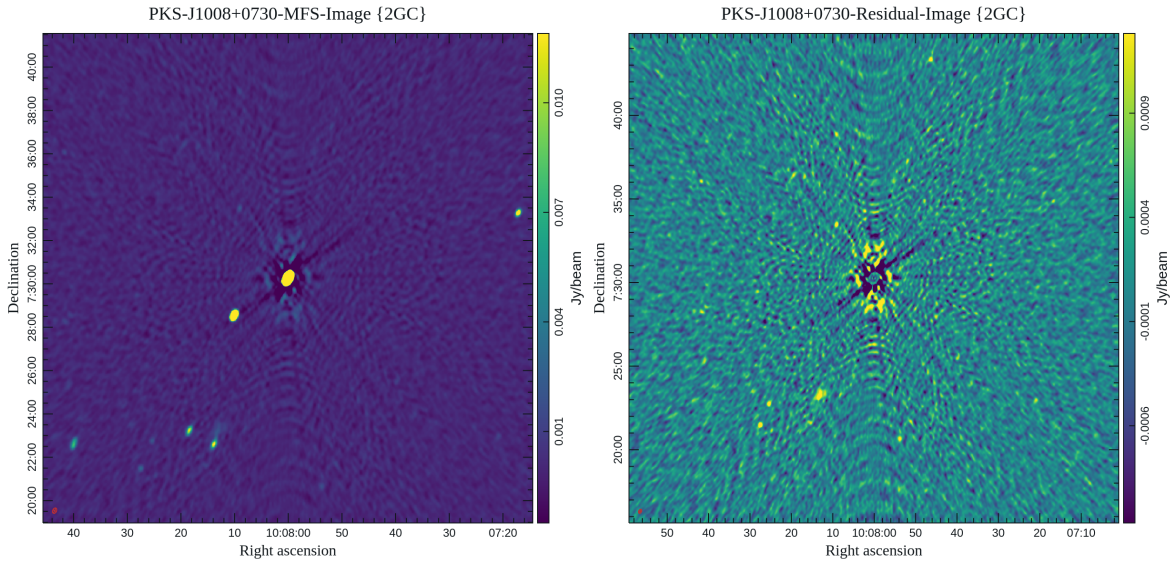

(a) PKS J1008+0730

(b) PKS J1008+0730 residual

Figure A.5: MFS and Residual Image of the phase calibrator PKS J1008+0730 after the 2nd generation calibration in the L-band. From Figure 3.8a, we note that the bright PSF around the calibrator has been reduced with the faint sources to the southeast of the calibrator clearly visible. The residual image in Figure A.5b indicates that no over-cleaning occurred (no negative holes).

Appendix B

LTV Radio Light Curves

The radio light curves in this section were produced for each calibrator in our sub-sample based on the fluxes extracted from the SDP pipeline and the three MeerKAT bands (U-band, L-band, and S4 sub-band). The light curves cover a two-year period; the years 2021-2023 in the U-band, 2020-2022 in the L-band, and 2022-2023 in the S4 sub-band.

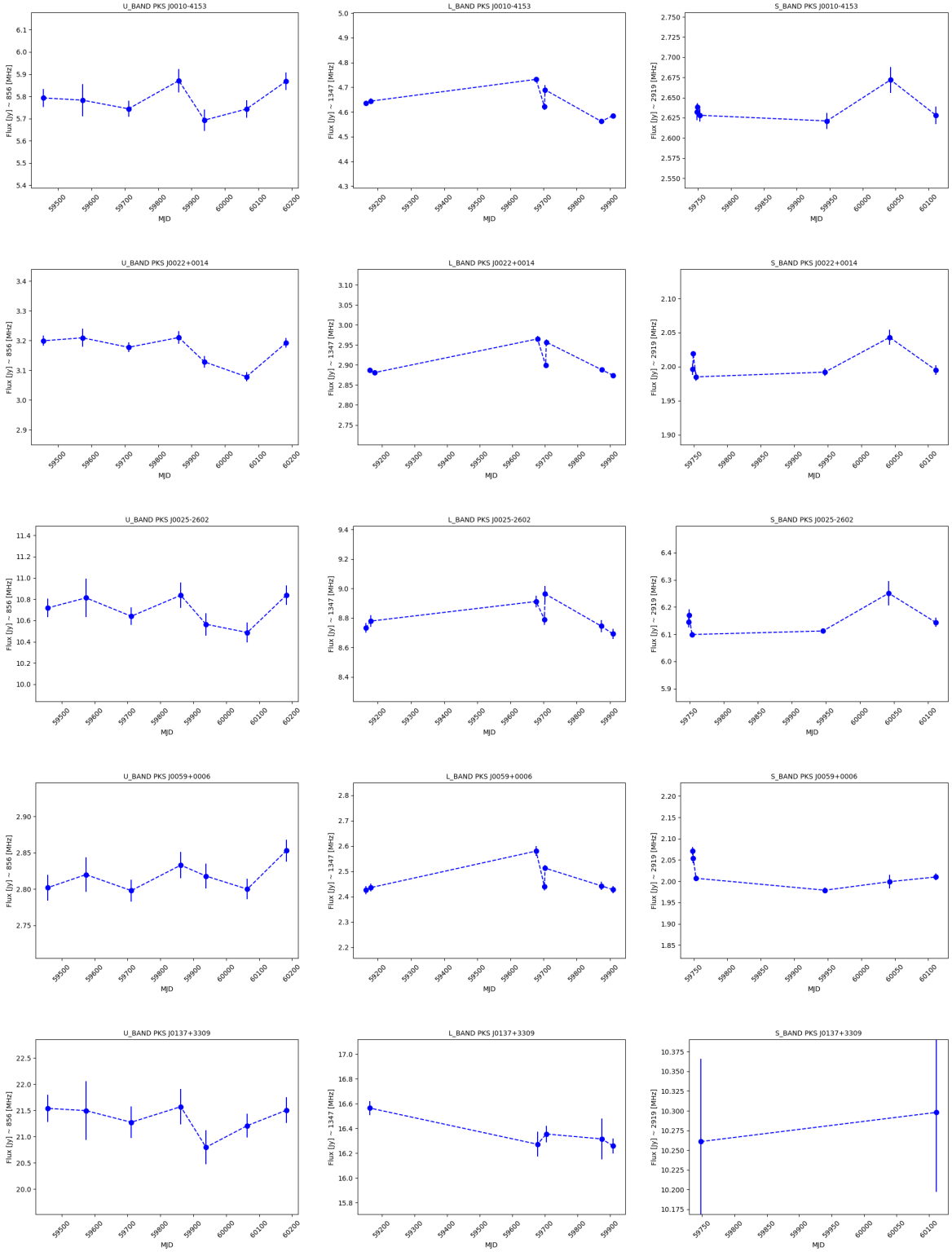

Figure B.1: Flux variability as a function of MJD

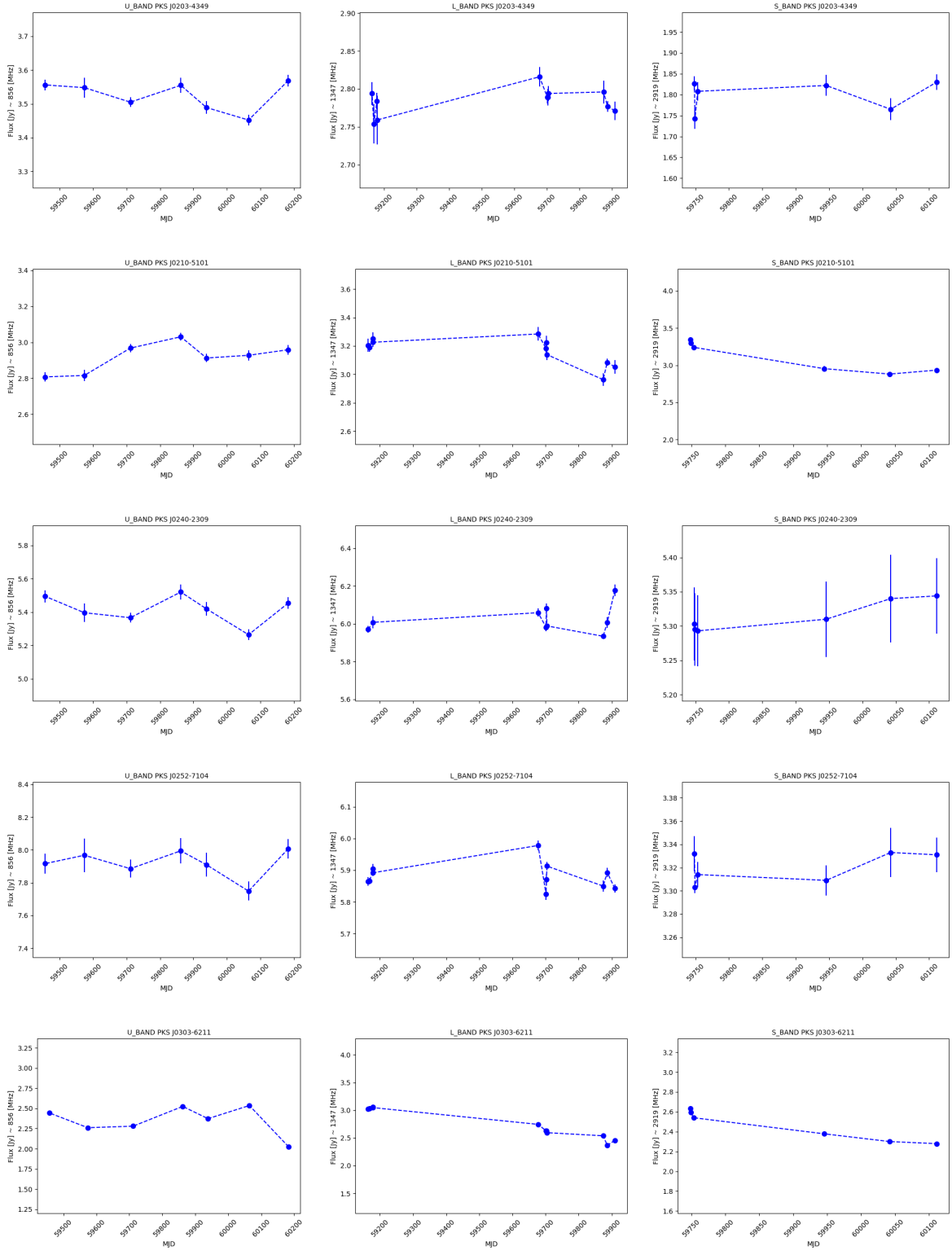

Figure B.2: Flux variability as a function of MJD

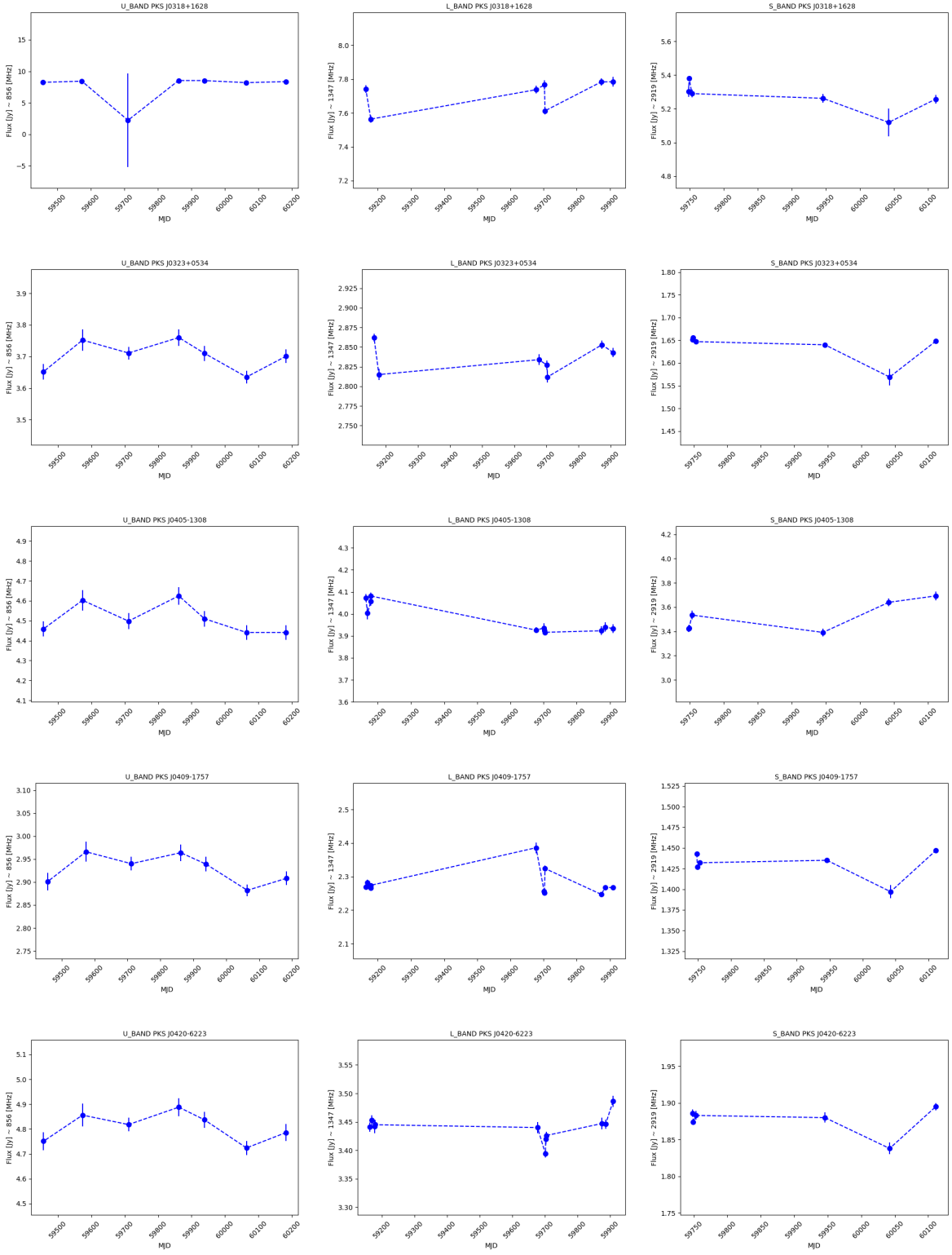

Figure B.3: Flux variability as a function of MJD

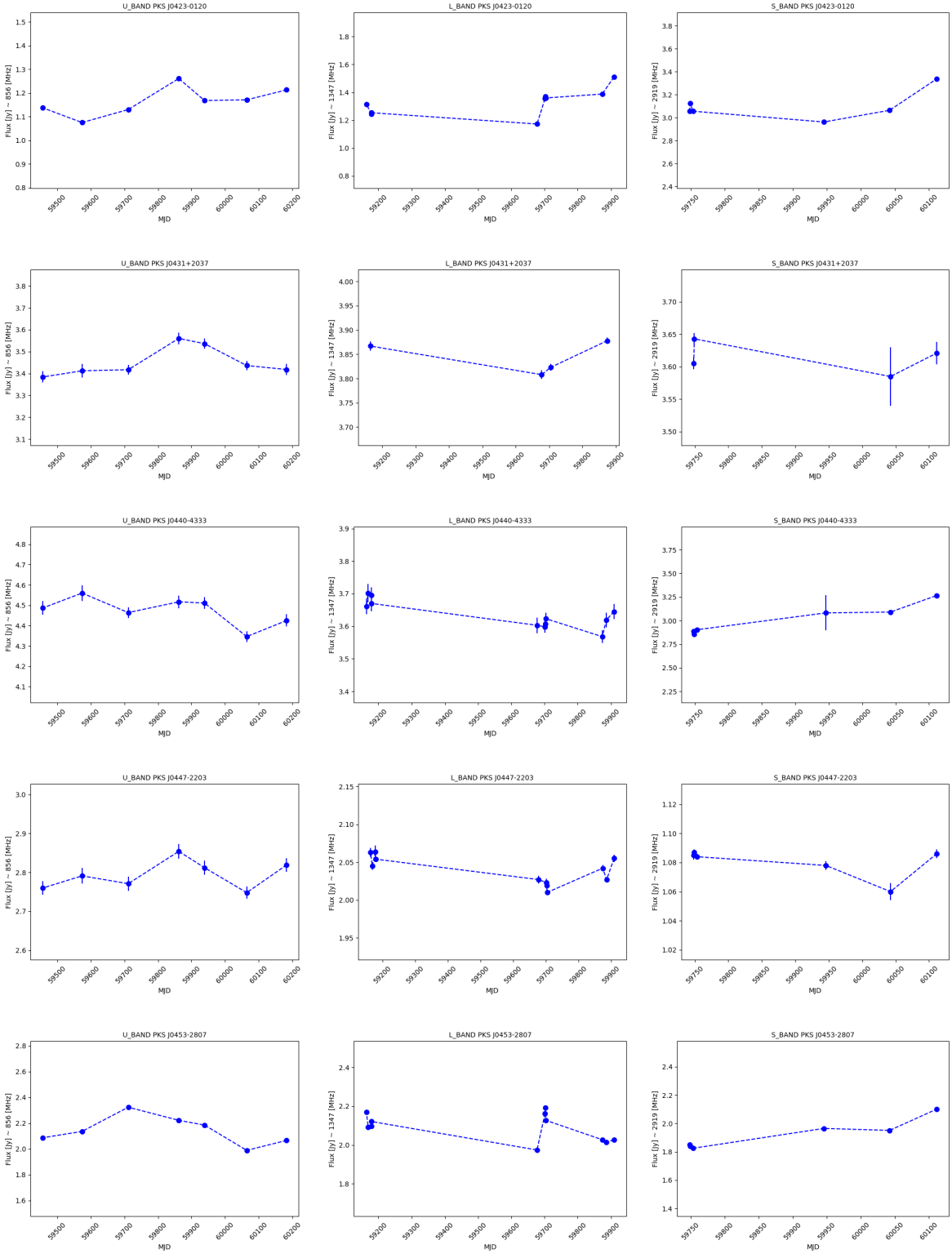

Figure B.4: Flux variability as a function of MJD

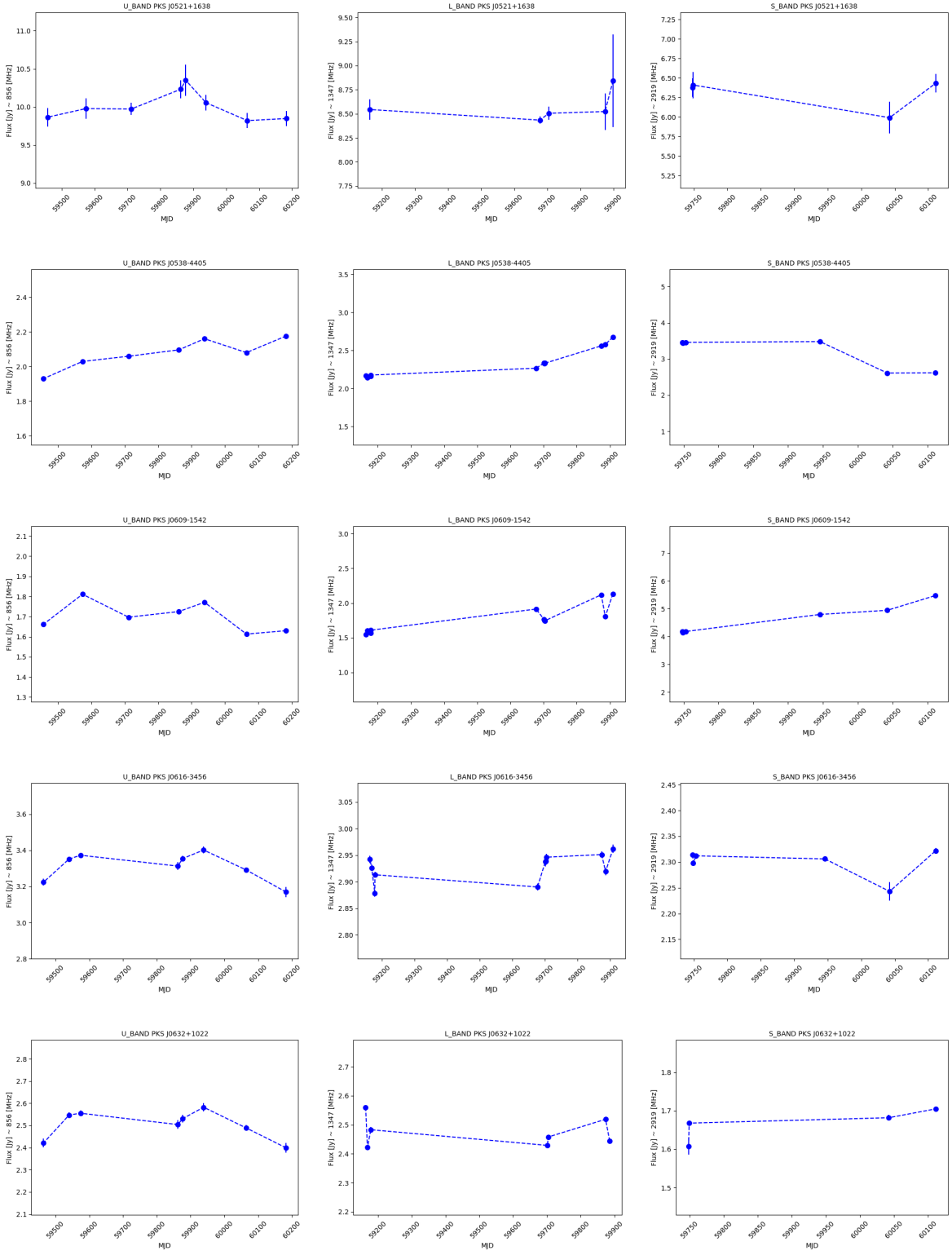

Figure B.5: Flux variability as a function of MJD

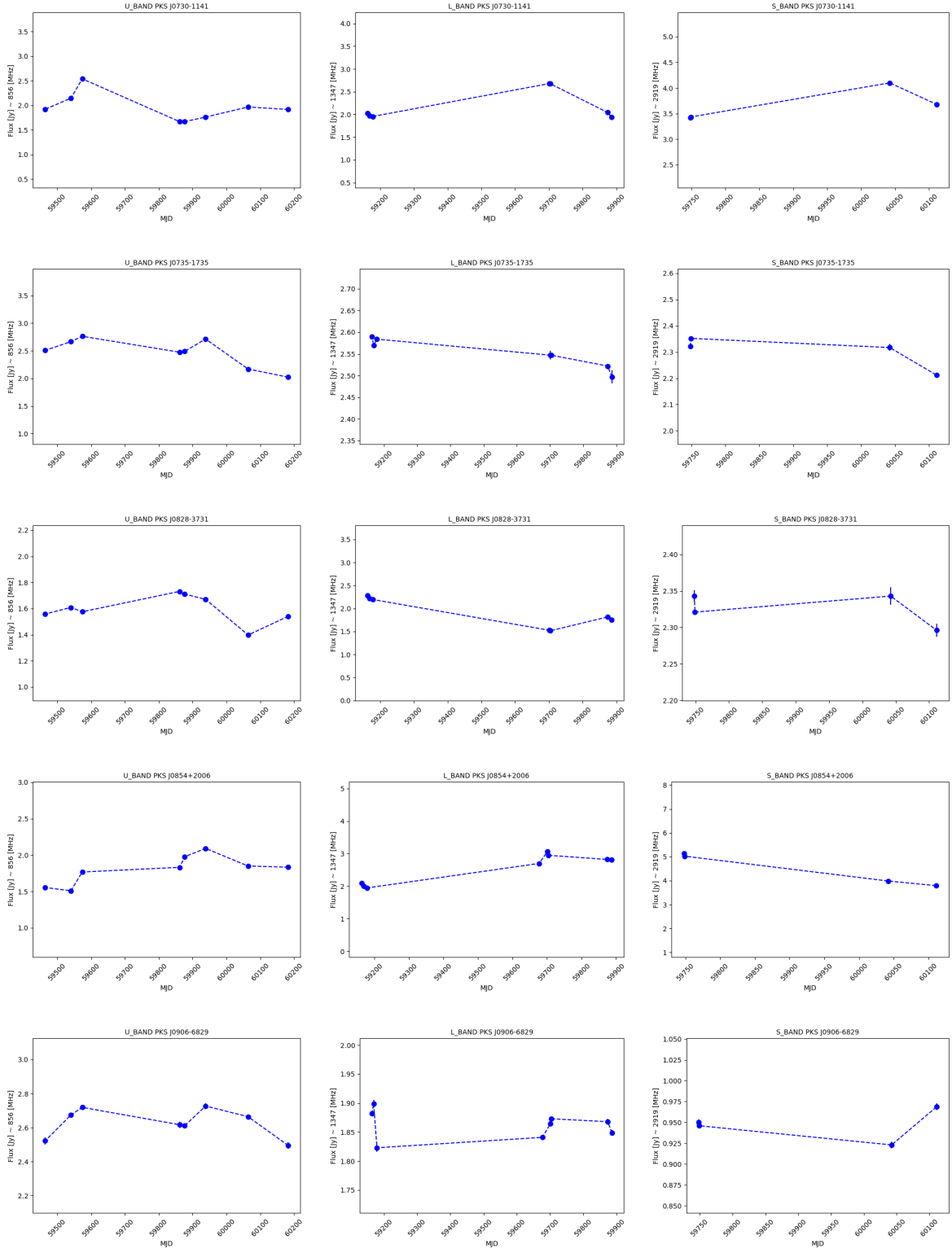

Figure B.6: Flux variability as a function of MJD

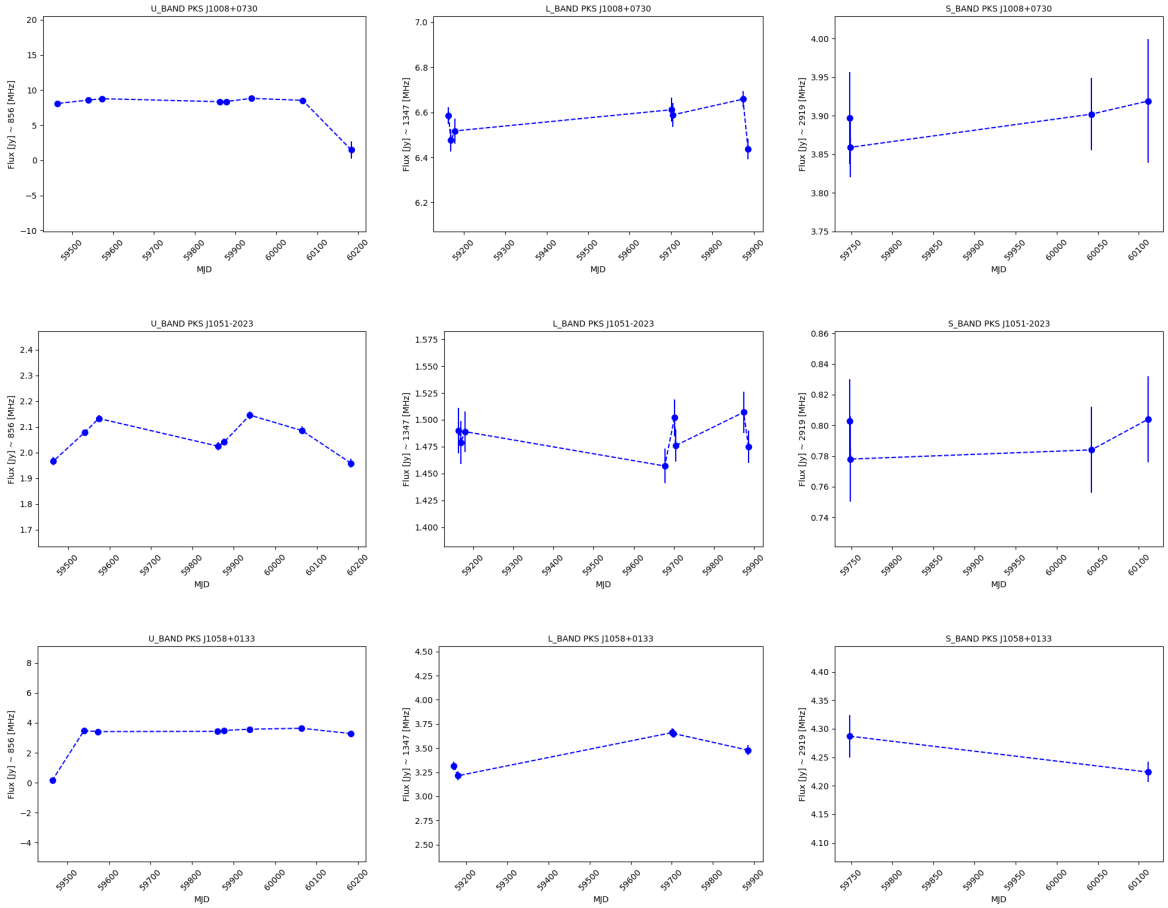

Figure B.7: Flux variability as a function of MJD

Bibliography

M. F. Aller, H. D. Aller, and P. A. Hughes. Radioband Properties of AGNs. In *American Astronomical Society Meeting Abstracts*, volume 195 of *American Astronomical Society Meeting Abstracts*, page 16.09, Dec. 1999.

ASSA. Astronomical society of south australia radio astronomy web site. https://www.assa.org.au/resources/radio-astronomy/(Accessed: 1 July 2022).

ATCA Database. Atca calibrator database v3. https://www.narrabri.atnf.csiro.au/calibrators/calibrator_database_viewcal?source=1549-790(Accessed: 12 May 2024).

D. J. Axon, A. Capetti, R. Fanti, R. Morganti, A. Robinson, and R. Spencer. The Morphology of the Emission-Line Region Of Compact Steep-Spectrum Radio Sources. , 120(5):2284–2299, Nov. 2000. doi: 10.1086/316838.

R. Barvainis, J. Lehár, M. Birkinshaw, H. Falcke, and K. M. Blundell. Radio variability of radio-quiet and radio-loud quasars. *The Astrophysical Journal*, 618(1):108, jan 2005. doi: 10.1086/425859. URL https://dx.doi.org/10.1086/425859.

P. N. Best, L. M. Ker, C. Simpson, E. E. Rigby, and J. Sabater. The cosmic evolution of radio-AGN feedback to z = 1. , 445(1):955–969, Nov. 2014. doi: 10.1093/mnras/stu1776.

A. M. Burgess and R. W. Hunstead. The Molonglo Southern 4 Jy Sample (MS4). II. ATCA Imaging and Optical Identification. , 131(1):114–132, Jan. 2006. doi: 10.1086/498679.

F. Camilo, P. Scholz, M. Serylak, S. Buchner, M. Merryfield, V. M. Kaspi, R. F. Archibald, M. Bailes, A. Jameson, W. v. Straten, J. Sarkissian, J. E. Reynolds, S. Johnston, G. Hobbs, T. D. Abbott, R. M. Adam, G. B. Adams, T. Alberts, R. Andreas, K. M. B. Asad, D. E.

Baker, T. Baloyi, E. F. Bauermeister, T. Baxana, T. G. H. Bennett, G. Bernardi, D. Booisen, R. S. Booth, D. H. Botha, L. Boyana, L. R. S. Brederode, J. P. Burger, T. Cheetham, J. Conradie, J. P. Conradie, D. B. Davidson, G. D. Bruin, B. d. Swardt, C. d. Villiers, D. I. L. d. Villiers, M. S. d. Villiers, W. d. Villiers, C. D. Waal, M. A. Dikgale, G. d. Toit, L. J. d. Toit, S. W. P. Esterhuyse, B. Fanaroff, S. Fataar, A. R. Foley, G. Foster, D. Fourie, R. Gamatham, T. Gatsi, R. Geschke, S. Goedhart, T. L. Grobler, S. C. Gumede, M. J. Hlakola, A. Hokwana, D. H. Hoorn, D. Horn, J. Horrell, B. Hugo, A. Isaacson, O. Jacobs, J. P. J. van Rensburg, J. L. Jonas, B. Jordaan, A. Joubert, F. Joubert, G. I. G. Józsa, R. Julie, C. C. Julius, F. Kapp, A. Karastergiou, F. Karels, M. Kariseb, R. Karuppusamy, V. Kasper, E. C. Knox-Davies, D. Koch, P. P. A. Kotzé, A. Krebs, N. Kriek, H. Kriel, T. Kusel, S. Lamoor, R. Lehmensiek, D. Liebenberg, I. Liebenberg, R. T. Lord, B. Lunsky, N. Mabombo, T. Macdonald, P. Macfarlane, K. Madisa, L. Mafhungo, L. G. Magnus, C. Magozore, O. Mahgoub, J. P. L. Main, S. Makhathini, J. A. Malan, P. Malgas, J. R. Manley, M. Manzini, L. Marais, N. Marais, S. J. Marais, M. Maree, A. Martens, S. D. Matshawule, N. Matthysen, T. Mauch, L. D. M. Nally, B. Merry, R. P. Millenaar, C. Mjikelo, N. Mkhabela, N. Mnyandu, I. T. Moeng, O. J. Mokone, T. E. Monama, K. Montshiwa, V. Moss, M. Mphego, W. New, B. Ngcebetsha, K. Ngoasheng, H. Niehaus, P. Ntuli, A. Nzama, F. Obies, M. Obrocka, M. T. Ockards, C. Olyn, N. Oozeer, A. J. Otto, Y. Padayachee, S. Passmoor, A. A. Patel, S. Paula, A. Peens-Hough, B. Pholoholo, P. Prozesky, S. Rakoma, A. J. T. Ramaila, I. Rammala, Z. R. Ramudzuli, M. Rasivhaga, S. Ratcliffe, H. C. Reader, R. Renil, L. Richter, A. Robyntjies, D. Rosekrans, A. Rust, S. Salie, N. Sambu, C. T. G. Schollar, L. Schwardt, S. Seranyane, G. Sethosa, C. Sharpe, R. Siebrits, S. K. Sirothia, M. J. Slabber, O. Smirnov, S. Smith, L. Sofeya, N. Songqumase, R. Spann, B. Stappers, D. Steyn, T. J. Steyn, R. Strong, A. Struthers, C. Stuart, P. Sunnylall, P. S. Swart, B. Taljaard, C. Tasse, G. Taylor, I. P. Theron, V. Thondikulam, K. Thorat, A. Tiplady, O. Toruvanda, J. v. Aardt, T. v. Balla, L. v. d. Heever, A. v. d. Byl, C. v. d. Merwe, P. v. d. Merwe, P. C. v. Niekerk, R. v. Rooyen, J. P. v. Staden, V. v. Tonder, R. v. Wyk, I. Wait, A. L. Walker, B. Wallace, M. Welz, L. P. Williams, B. Xaia, N. Young, and S. Zitha. Revival of the magnetar psr j1622–4950: Observations with meerkat, parkes, xmm-newton, swift, chandra, and nustar. *The Astrophysical Journal*, 856(2):180, Apr. 2018. ISSN 1538-4357. doi: 10.3847/1538-4357/aab35a. URL

http://dx.doi.org/10.3847/1538-4357/aab35a.

CASA Documentation. Casa documentation. https://casadocs.readthedocs.io/en/v6.5.5/index.html(Accessed: 16 March 2023).

CASA Team, B. Bean, S. Bhatnagar, S. Castro, J. Donovan Meyer, B. Emonts, E. Garcia, R. Garwood, K. Golap, J. Gonzalez Villalba, P. Harris, Y. Hayashi, J. Hoskins, M. Hsieh, P. Jagannathan, W. Kawasaki, A. Keimpema, M. Kettenis, J. Lopez, J. Marvil, J. Masters, A. McNichols, D. Mehringer, R. Miel, G. Moellenbrock, F. Montesino, T. Nakazato, J. Ott, D. Petry, M. Pokorny, R. Raba, U. Rau, D. Schiebel, N. Schweighart, S. Sekhar, K. Shimada, D. Small, J.-W. Steeb, K. Sugimoto, V. Suoranta, T. Tsutsumi, I. M. van Bemmel, M. Verkouter, A. Wells, W. Xiong, A. Szomoru, M. Griffith, B. Glendenning, and J. Kern. CASA, the Common Astronomy Software Applications for Radio Astronomy. , 134(1041):114501, Nov. 2022. doi: 10.1088/1538-3873/ac9642.

P. Charlot, C. S. Jacobs, D. Gordon, S. Lambert, A. de Witt, J. Böhm, A. L. Fey, R. Heinkelmann, E. Skurikhina, O. Titov, E. F. Arias, S. Bolotin, G. Bourda, C. Ma, Z. Malkin, A. Nothnagel, D. Mayer, D. S. MacMillan, T. Nilsson, and R. Gaume. The third realization of the International Celestial Reference Frame by very long baseline interferometry. , 644:A159, dec 2020. doi: 10.1051/0004-6361/202038368.

J. H. Y. Ching, E. M. Sadler, S. M. Croom, H. M. Johnston, M. B. Pracy, W. J. Couch, A. M. Hopkins, R. J. Jurek, and K. A. Pimbblet. The Large Area Radio Galaxy Evolution Spectroscopic Survey (LARGESS): survey design, data catalogue and GAMA/WiggleZ spectroscopy. , 464(2):1306–1332, Jan. 2017. doi: 10.1093/mnras/stw2396.

J. J. Condon and S. M. Ransom. *Essential Radio Astronomy*. Princeton University Press, 2016.

J. J. Condon, W. D. Cotton, E. W. Greisen, Q. F. Yin, R. A. Perley, G. B. Taylor, and J. J. Broderick. The NRAO VLA Sky Survey. , 115(5):1693–1716, May 1998a. doi: 10.1086/300337.

J. J. Condon, W. D. Cotton, E. W. Greisen, Q. F. Yin, R. A. Perley, G. B. Taylor, and J. J.

Broderick. The NRAO VLA Sky Survey. , 115(5):1693–1716, May 1998b. doi: 10.1086/300337.

W. Cotton. Obit: A development environment for astronomical algorithms. *Publications of the Astronomical Society of the Pacific*, 120(866):439, 2008.

P. V. de la Parra, A. C. S. Readhead, T. Herbig, S. Kiehlmann, M. L. Lister, V. Pavlidou, R. A. Reeves, A. Siemiginowska, A. G. Sullivan, T. Surti, A. Synani, K. Tassis, G. B. Taylor, P. N. Wilkinson, M. F. Aller, R. D. Blandford, N. Globus, C. R. Lawrence, B. Molina, S. O'Neill, and T. J. Pearson. The Radio Spectra of High-luminosity Compact Symmetric Objects: Implications for Studies of Compact Jetted Active Galactic Nuclei. , 977(2):195, Dec. 2024. doi: 10.3847/1538-4357/ad89bb.

R. Dodson, E. B. Fomalont, K. Wiik, S. Horiuchi, H. Hirabayashi, P. G. Edwards, Y. Murata, Y. Asaki, G. A. Moellenbrock, W. K. Scott, A. R. Taylor, L. I. Gurvits, Z. Paragi, S. Frey, Z. Q. Shen, J. E. J. Lovell, S. J. Tingay, M. J. Rioja, S. Fodor, M. L. Lister, L. Mosoni, G. Coldwell, B. G. Piner, and J. Yang. The VSOP 5 GHz Active Galactic Nucleus Survey. V. Imaging Results for the Remaining 140 Sources. , 175(2):314–355, Apr. 2008. doi: 10.1086/525025.

J. N. Douglas, F. N. Bash, F. A. Bozyan, G. W. Torrence, and C. Wolfe. The Texas Survey of Radio Sources Covering -35.5 degrees < declination < 71.5 degrees at 365 MHz. , 111: 1945, May 1996. doi: 10.1086/117932.

P. G. Edwards and S. J. Tingay. New candidate GHz peaked spectrum and compact steep spectrum sources. , 424:91–106, Sept. 2004. doi: 10.1051/0004-6361:20035749.

P. G. Edwards and S. J. Tingay. New candidate ghz peaked spectrum and compact steep spectrum sources. *Astronomy amp; Astrophysics*, 424(1):91–106, 2004. doi: 10.1051/0004-6361:20042435749.

J. H. Fan, Y. Liu, Y. H. Yuan, Q. Guo, T. X. Hua, Y. W. Zhang, J. B. Su, J. S. Zhang, and J. Y. Zhang. Radio Variability Properties for Radio Sources. In L. C. Ho and J. W. Wang, editors, *The Central Engine of Active Galactic Nuclei*, volume 373 of *Astronomical Society of the Pacific Conference Series*, page 195, Oct. 2007.

A. R. Foley, T. Alberts, R. P. Armstrong, A. Barta, E. F. Bauermeister, H. Bester, S. Blose, R. S. Booth, D. H. Botha, S. J. Buchner, C. Carignan, T. Cheetham, K. Cloete, G. Coreejes, R. C. Crida, S. D. Cross, F. Curtolo, A. Dikgale, M. S. de Villiers, L. J. du Toit, S. W. P. Esterhuyse, B. Fanaroff, R. P. Fender, M. Fijalkowski, D. Fourie, B. Frank, D. George, P. Gibbs, S. Goedhart, J. Grobbelaar, S. C. Gumede, P. Herselman, K. M. Hess, N. Hoek, J. Horrell, J. L. Jonas, J. D. B. Jordaan, R. Julie, F. Kapp, P. Kotzé, T. Kusel, A. Langman, R. Lehmensiek, D. Liebenberg, I. J. V. Liebenberg, A. Loots, R. T. Lord, D. M. Lucero, J. Ludick, P. Macfarlane, M. Madlavana, L. Magnus, C. Magozore, J. A. Malan, J. R. Manley, L. Marais, N. Marais, S. J. Marais, M. Maree, A. Martens, O. Mokone, V. Moss, S. Mthembu, W. New, G. D. Nicholson, P. C. van Niekerk, N. Oozeer, S. S. Passmoor, A. Peens-Hough, A. B. Pińska, P. Prozesky, S. Rajan, S. Ratcliffe, R. Renil, L. L. Richter, D. Rosekrans, A. Rust, A. C. Schröder, L. C. Schwardt, S. Seranyane, M. Serylak, D. S. Shepherd, R. Siebrits, L. Sofeya, R. Spann, R. Springbok, P. S. Swart, V. L. Thondikulam, I. P. Theron, A. Tiplady, O. Toruvanda, S. Tshongweni, L. van den Heever, C. van der Merwe, R. van Rooyen, S. Wakhaba, A. L. Walker, M. Welz, L. Williams, M. Wolleben, P. A. Woudt, N. J. Young, and J. T. L. Zwart. Engineering and science highlights of the kat-7 radio telescope. *Monthly Notices of the Royal Astronomical Society*, 460(2):1664–1679, 05 2016. ISSN 0035-8711. doi: 10.1093/mnras/stw1040. URL https://doi.org/10.1093/mnras/stw1040.

GAVRT. *Basics of Radio Astronomy: For the Goldstone-Apple Valley Radio Telescope*. National Aeronautics and Space Administration Jet Propulsion Laboratory, 1997. URL https://books.google.co.ke/books?id=5tUHkAEACAAJ.

A. C. Gupta, D. P. K. Banerjee, N. M. Ashok, and U. C. Joshi. Near infrared intraday variability of Mrk 421. , 422:505–508, Aug. 2004. doi: 10.1051/0004-6361:20040306.

N. Gupta, C. J. Salter, D. J. Saikia, T. Ghosh, and S. Jeyakumar. Probing radio source environments via HI and OH absorption. , 373(3):972–992, Dec. 2006. doi: 10.1111/j.1365-2966.2006.11064.x.

C. L. Hale, D. McConnell, A. J. M. Thomson, E. Lenc, G. H. Heald, A. W. Hotan, J. K. Leung, V. A. Moss, T. Murphy, J. Pritchard, E. M. Sadler, A. J. Stewart, and M. T. Whiting.

The Rapid ASKAP Continuum Survey Paper II: First Stokes I Source Catalogue Data Release. , 38:e058, Nov. 2021. doi: 10.1017/pasa.2021.47.

J. P. Hamaker, J. D. Bregman, and R. J. Sault. Understanding radio polarimetry. I. Mathematical foundations. , 117:137–147, May 1996.

J. Högbom. Astronomy & astrophysics suppl. In *Ser*, volume 15, page 417, 1974.

T. Hovatta, H. J. Lehto, and M. Tornikoski. Wavelet analysis of a large sample of AGN at high radio frequencies. , 488(3):897–903, Sept. 2008. doi: 10.1051/0004-6361:200810200.

B. V. Hugo, S. Perkins, B. Merry, T. Mauch, and O. M. Smirnov. Tricolour: An Optimized SumThreshold Flagger for MeerKAT. In J. E. Ruiz, F. Pierfedereci, and P. Teuben, editors, *Astronomical Society of the Pacific Conference Series*, volume 532 of *Astronomical Society of the Pacific Conference Series*, page 541, July 2022. doi: 10.48550/arXiv.2206.09179.

N. Hurley-Walker, J. R. Callingham, P. J. Hancock, T. M. O. Franzen, L. Hindson, A. D. Kapińska, J. Morgan, A. R. Offringa, R. B. Wayth, C. Wu, Q. Zheng, T. Murphy, M. E. Bell, K. S. Dwarakanath, B. For, B. M. Gaensler, M. Johnston-Hollitt, E. Lenc, P. Procopio, L. Staveley-Smith, R. Ekers, J. D. Bowman, F. Briggs, R. J. Cappallo, A. A. Deshpande, L. Greenhill, B. J. Hazelton, D. L. Kaplan, C. J. Lonsdale, S. R. McWhirter, D. A. Mitchell, M. F. Morales, E. Morgan, D. Oberoi, S. M. Ord, T. Prabu, N. U. Shankar, K. S. Srivani, R. Subrahmanyan, S. J. Tingay, R. L. Webster, A. Williams, and C. L. Williams. GaLactic and Extragalactic All-sky Murchison Widefield Array (GLEAM) survey - I. A low-frequency extragalactic catalogue. , 464(1):1146–1167, Jan. 2017. doi: 10.1093/mnras/stw2337.

J. Jonas and MeerKAT Team. The MeerKAT Radio Telescope. In *MeerKAT Science: On the Pathway to the SKA*, page 1, Jan. 2016. doi: 10.22323/1.277.0001.

S. G. Jorstad, A. P. Marscher, M. L. Lister, A. M. Stirling, T. V. Cawthorne, W. K. Gear, J. L. Gómez, J. A. Stevens, P. S. Smith, J. R. Forster, and E. I. Robson. Polarimetric Observations of 15 Active Galactic Nuclei at High Frequencies: Jet Kinematics from

Bimonthly Monitoring with the Very Long Baseline Array. , 130(4):1418–1465, Oct. 2005. doi: 10.1086/444593.

G. I. G. Jozsa, S. V. White, K. Thorat, O. M. Smirnov, P. Serra, M. Ramatsoku, A. J. T. Ramaila, S. J. Perkins, D. C. Molnár, S. Makhathini, F. M. Maccagni, D. Kleiner, P. Kamphuis, B. V. Hugo, W. J. G. de Blok, and L. A. L. Andati. Meerkathi - an end-to-end data reduction pipeline for meerkat and other radio telescopes. In R. Pizzo, E. Deul, J.-D. Mol, J. de Plaa, and H. Verkouter, editors, *ADASS XXIX*, volume 527 of *ASP Conf. Ser.*, pages 635–638, San Francisco, 2020.

E. A. Kassaye. *A study of potential calibrators using the KAT-7 Radio Telescope*. PhD thesis, University of Cape Town, 2015.

L. L. Kedziora-Chudczer, D. L. Jauncey, M. H. Wieringa, J. E. Reynolds, and A. K. Tzioumis. Four Southern Intraday Variable Radio Sources. In J. A. Zensus, G. B. Taylor, and J. M. Wrobel, editors, *IAU Colloq. 164: Radio Emission from Galactic and Extragalactic Compact Sources*, volume 144 of *Astronomical Society of the Pacific Conference Series*, page 271, Jan. 1998.

M. A. Keim, J. R. Callingham, and H. J. A. Röttgering. Extragalactic megahertz-peaked spectrum radio sources at milliarcsecond scales. , 628:A56, Aug. 2019. doi: 10.1051/0004-6361/201936107.

K. I. Kellermann, R. C. Vermeulen, J. A. Zensus, and M. H. Cohen. Sub-Milliarcsecond Imaging of Quasars and Active Galactic Nuclei. , 115(4):1295–1318, Apr. 1998. doi: 10.1086/300308.

A. K. Kembhavi and J. V. Narlikar. *Quasars and active galactic nuclei : an introduction*. 1999.

J. Kenyon, S. Perkins, H. Bester, O. Smirnov, C. Russeeawon, and B. Hugo. Africanus ii. quartical: Calibrating radio interferometer data at scale using numba and dask. *Astronomy and Computing*, 52:100962, 2025. ISSN 2213-1337. doi: https://doi.org/10.1016/j.ascom.2025.100962. URL https://www.sciencedirect.com/science/article/pii/S2213133725000356.

P. Kharb, M. L. Lister, and N. J. Cooper. Extended Radio Emission in MOJAVE Blazars: Challenges to Unification. , 710(1):764–782, Feb. 2010. doi: 10.1088/0004-637X/710/1/764.

H. Kuehr, A. Witzel, I. I. K. Pauliny-Toth, and U. Nauber. A Catalogue of Extragalactic Radio Sources Having Flux Densities Greater than 1-JY at 5-GHZ. , 45:367, Sept. 1981.

A. Labiano, P. D. Barthel, C. P. O'Dea, W. H. de Vries, I. Pérez, and S. A. Baum. GPS radio sources: new optical observations and an updated master list. , 463(1):97–104, Feb. 2007. doi: 10.1051/0004-6361:20066183.

R. A. Laing and J. A. Peacock. The relation between radio luminosity and spectrum for extended extragalactic radio sources. , 190:903–924, Mar. 1980. doi: 10.1093/mnras/190.4.903.

Lal. Gmrt observer's manual. http://www.ncra.tifr.res.in/ncra/gmrt/gmrt-users/observing-help/manual_7jul15.pdf, 2015. Accessed: [31 July 2024].

M. I. Large, B. Y. Mills, A. G. Little, D. F. Crawford, and J. M. Sutton. The Molonglo Reference Catalogue of radio sources. , 194:693–704, Feb. 1981. doi: 10.1093/mnras/194.3.693.

S. A. Laurent-Muehleisen, R. I. Kollgaard, P. J. Ryan, E. D. Feigelson, W. Brinkmann, and J. Siebert. Radio-loud active galaxies in the northern ROSAT All-Sky Survey. I. Radio identifications. , 122:235–247, Apr. 1997. doi: 10.1051/aas:1997331.

D. Lin, N. A. Webb, and D. Barret. Classification of X-Ray Sources in the XMM-Newton Serendipitous Source Catalog. , 756(1):27, Sept. 2012. doi: 10.1088/0004-637X/756/1/27.

M. L. Lister, A. P. Marscher, and W. K. Gear. Submilliarcsecond Polarimetric Imaging of Blazar Jets at 43 GHz. , 504(2):702–719, Sept. 1998. doi: 10.1086/306112.

F. K. Liu and Y. H. Zhang. A new list of extra-galactic radio jets. , 381:757–760, Jan. 2002. doi: 10.1051/0004-6361:20011572.

X. Liu, L. Cui, W.-F. Luo, W.-Z. Shi, and H.-G. Song. Vlbi observations of nineteen ghz-peaked-spectrum radio sources at 1.6 ghz. *Astronomy amp; Astrophysics*, 470(1):97–104, 2007. doi: 10.1051/0004-6361:20077265.

F. J. Lockman. *Radio astronomy: Observing the invisible universe, course guidebook*. The Teaching Company, 2017.

F. Mantovani, K. H. Mack, F. M. Montenegro-Montes, A. Rossetti, and A. Kraus. Effelsberg 100-m polarimetric observations of a sample of compact steep-spectrum sources. , 502 (1):61–65, July 2009. doi: 10.1051/0004-6361/200911815.

J. M. Marr, R. L. Snell, and S. E. Kurtz. *Fundamentals of Radio Astronomy: Observational Methods (Series in Astronomy and Astrophysics)*. Taylor Francis Group, 2015.

L. D. Matthews and M. J. Reid. Very Large Array Observations of H I in the Circumstellar Envelopes of Asymptotic Giant Branch Stars. , 133(5):2291–2309, May 2007. doi: 10.1086/512613.

T. Mauch, T. Murphy, H. J. Buttery, J. Curran, R. W. Hunstead, B. Piestrzynski, J. G. Robertson, and E. M. Sadler. SUMSS: a wide-field radio imaging survey of the southern sky - II. The source catalogue. , 342(4):1117–1130, July 2003a. doi: 10.1046/j.1365-8711.2003.06605.x.

T. Mauch, T. Murphy, H. J. Buttery, J. Curran, R. W. Hunstead, B. Piestrzynski, J. G. Robertson, and E. M. Sadler. SUMSS: a wide-field radio imaging survey of the southern sky - II. The source catalogue. , 342(4):1117–1130, July 2003b. doi: 10.1046/j.1365-8711.2003.06605.x.

B. W. Meyers, N. Hurley-Walker, P. J. Hancock, T. M. O. Franzen, E. Carretti, L. Staveley-Smith, B. M. Gaensler, M. Haverkorn, and S. Poppi. A Southern-Sky Total Intensity Source Catalogue at 2.3 GHz from S-Band Polarisation All-Sky Survey Data. , 34:e013, Mar. 2017. doi: 10.1017/pasa.2017.5.

N. Mohan and D. Rafferty. PyBDSF: Python Blob Detection and Source Finder. Astrophysics Source Code Library, record ascl:1502.007, Feb. 2015.

T. C. A. Molteno. Correlation structure in flux-density calibrator models. , 527(3):5732–5740, Jan. 2024. doi: 10.1093/mnras/stad3519.

J. S. Morgan, J.-P. Macquart, R. Ekers, R. Chhetri, M. Tokumaru, P. K. Manoharan, S. Tremblay, M. M. Bisi, and B. V. Jackson. Interplanetary scintillation with the murchison wide-field array i: a sub-arcsecond survey over 900 deg2 at 79 and 158 mhz. *Monthly Notices of the Royal Astronomical Society*, 473(3):2965–2983, 09 2017. ISSN 0035-8711. doi: 10.1093/mnras/stx2284. URL https://doi.org/10.1093/mnras/stx2284.

T. Murphy, E. M. Sadler, R. D. Ekers, M. Massardi, P. J. Hancock, E. Mahony, R. Ricci, S. Burke-Spolaor, M. Calabretta, R. Chhetri, G. de Zotti, P. G. Edwards, J. A. Ekers, C. A. Jackson, M. J. Kesteven, E. Lindley, K. Newton-McGee, C. Phillips, P. Roberts, R. J. Sault, L. Staveley-Smith, R. Subrahmanyan, M. A. Walker, and W. E. Wilson. The Australia Telescope 20 GHz Survey: the source catalogue. , 402(4):2403–2423, Mar. 2010. doi: 10.1111/j.1365-2966.2009.15961.x.

J. E. Noordam and O. M. Smirnov. The MeqTrees software system and its use for third-generation calibration of radio interferometers. , 524:A61, Dec. 2010. doi: 10.1051/0004-6361/201015013.

Ochsenbein, F., Bauer, P., and Marcout, J. The vizier database of astronomical catalogues. *Astron. Astrophys. Suppl. Ser.*, 143(1):23–32, 2000. doi: 10.1051/aas:2000169. URL https://doi.org/10.1051/aas:2000169.

C. P. O'Dea. The Compact Steep-Spectrum and Gigahertz Peaked-Spectrum Radio Sources. , 110(747):493–532, May 1998. doi: 10.1086/316162.

A. R. Offringa and O. Smirnov. An optimized algorithm for multiscale wideband deconvolution of radio astronomical images. , 471(1):301–316, Oct. 2017. doi: 10.1093/mnras/stx1547.

A. R. Offringa, B. McKinley, N. Hurley-Walker, F. H. Briggs, R. B. Wayth, D. L. Kaplan, M. E. Bell, L. Feng, A. R. Neben, J. D. Hughes, J. Rhee, T. Murphy, N. D. R. Bhat, G. Bernardi, J. D. Bowman, R. J. Cappallo, B. E. Corey, A. A. Deshpande, D. Emrich, A. Ewall-Wice, B. M. Gaensler, R. Goeke, L. J. Greenhill, B. J. Hazelton, L. Hindson,

M. Johnston-Hollitt, D. C. Jacobs, J. C. Kasper, E. Kratzenberg, E. Lenc, C. J. Lonsdale, M. J. Lynch, S. R. McWhirter, D. A. Mitchell, M. F. Morales, E. Morgan, N. Kudryavtseva, D. Oberoi, S. M. Ord, B. Pindor, P. Procopio, T. Prabu, J. Riding, D. A. Roshi, N. U. Shankar, K. S. Srivani, R. Subrahmanyan, S. J. Tingay, M. Waterson, R. L. Webster, A. R. Whitney, A. Williams, and C. L. Williams. WSCLEAN: an implementation of a fast, generic wide-field imager for radio astronomy. , 444(1):606–619, Oct. 2014. doi: 10.1093/mnras/stu1368.

N. Oozeer, T. Mauch, and R. Booth. Blazar monitoring with KAT-7: PKS1510-089 a test case. , 86:42, Jan. 2015.

J. Ott, R. Raba, and J. Hibbard. CARTA: Cube Analysis and Rendering Tool for Astronomy 2.0 → 3.0. In *American Astronomical Society Meeting #240*, volume 240 of *American Astronomical Society Meeting Abstracts*, page 215.05, June 2022.

B. Peng, A. Kraus, T. P. Krichbaum, and A. Witzel. Long-term monitoring of selected radio sources. , 145:1–10, July 2000. doi: 10.1051/aas:2000230.

R. A. Perley and B. J. Butler. An accurate flux density scale from 1 to 50 ghz. *The Astrophysical Journal Supplement Series*, 204(2):19, jan 2013. doi: 10.1088/0067-0049/204/2/19. URL https://dx.doi.org/10.1088/0067-0049/204/2/19.

K. E. Randall, A. M. Hopkins, R. P. Norris, and P. G. Edwards. An unbiased sample of bright southern compact steep spectrum and gigahertz peaked spectrum sources. *Monthly Notices of the Royal Astronomical Society*, 416(2):1135–1151, 09 2011. ISSN 0035-8711. doi: 10.1111/j.1365-2966.2011.19116.x. URL https://doi.org/10.1111/j.1365-2966.2011.19116.x.

J. Reynolds. A revised flux scale for the at compact array. *ATCA memo series*, 39.3/040, 1994.

J. Roland, S. Britzen, A. Witzel, and J. A. Zensus. The origin of intrinsic variability of intraday variable sources. , 496(3):645–651, Mar. 2009. doi: 10.1051/0004-6361/200810709.

K. Ross, J. R. Callingham, N. Hurley-Walker, N. Seymour, P. Hancock, T. M. O. Franzen, J. Morgan, S. V. White, M. E. Bell, and P. Patil. Spectral variability of radio sources at

low frequencies. *Monthly Notices of the Royal Astronomical Society*, 501(4):6139–6155, 12 2020. ISSN 0035-8711. doi: 10.1093/mnras/staa3795. URL https://doi.org/10.1093/mnras/staa3795.

E. M. Sadler, R. Ricci, R. D. Ekers, J. A. Ekers, P. J. Hancock, C. A. Jackson, M. J. Kesteven, T. Murphy, C. Phillips, R. F. Reinfrank, L. Staveley-Smith, R. Subrahmanyan, M. A. Walker, W. E. Wilson, and G. De Zotti. The properties of extragalactic radio sources selected at 20ghz. *Monthly Notices of the Royal Astronomical Society*, 371(2):898–914, 08 2006. ISSN 0035-8711. doi: 10.1111/j.1365-2966.2006.10729.x. URL https://doi.org/10.1111/j.1365-2966.2006.10729.x.

SARAO. The meerkat knowledge base. "https://skaafrica.atlassian.net/wiki/spaces/ESDKB/overview?homepageId=41025669. Accessed: [12 May 2024].

W. K. Scott, E. B. Fomalont, S. Horiuchi, J. E. Lovell, G. A. Moellenbrock, R. G. Dodson, P. G. Edwards, G. V. Coldwell, S. Fodor, S. Frey, and et al. The vsop 5 ghz active galactic nucleus survey. iii. imaging results for the first 102 sources. *The Astrophysical Journal Supplement Series*, 155(1):33–72, 2004. doi: 10.1086/424819.

W. K. Scott, E. B. Fomalont, S. Horiuchi, J. E. J. Lovell, G. A. Moellenbrock, R. G. Dodson, P. G. Edwards, G. V. Coldwell, S. Fodor, S. Frey, L. I. Gurvits, H. Hirabayashi, M. L. Lister, L. Mosoni, Y. Murata, Z. Paragi, B. G. Piner, Z. Q. Shen, A. R. Taylor, and S. J. Tingay. The VSOP 5 GHz Active Galactic Nucleus Survey. III. Imaging Results for the First 102 Sources. , 155(1):33–72, Nov. 2004. doi: 10.1086/424819.

P. Serra, F. M. Maccagni, D. Kleiner, D. Molnár, M. Ramatsoku, A. Loni, F. Loi, W. J. G. de Blok, G. L. Bryan, R. J. Dettmar, B. S. Frank, J. H. van Gorkom, F. Govoni, E. Iodice, G. I. G. Józsa, P. Kamphuis, R. Kraan-Korteweg, S. I. Loubser, M. Murgia, T. A. Oosterloo, R. Peletier, D. J. Pisano, M. W. L. Smith, S. C. Trager, and M. A. W. Verheijen. The MeerKAT Fornax Survey. I. Survey description and first evidence of ram pressure in the Fornax galaxy cluster. , 673:A146, May 2023. doi: 10.1051/0004-6361/202346071.

Z. Q. Shen, T. S. Wan, J. M. Moran, D. L. Jauncey, J. E. Reynolds, A. K. Tzioumis, R. G. Gough, R. H. Ferris, M. W. Sinclair, D. R. Jiang, X. Y. Hong, S. G. Liang, P. G. Edwards,

M. E. Costa, S. J. Tingay, P. M. McCulloch, J. E. J. Lovell, E. A. King, G. D. Nicolson, D. W. Murphy, D. L. Meier, T. D. van Ommen, and G. L. White. A 5 GHz Southern Hemisphere VLBI Survey of Compact Radio Sources. II. , 115(4):1357–1370, Apr. 1998. doi: 10.1086/300284.

I. Sihlangu, N. Oozeer, and B. Bassett. Nature and Evolution of UHF and L-band Radio Frequency Interference at the MeerKAT Radio Telescope. In *The RFI 2022 Workshop at UCMWF*, page 1, Jan. 2022. doi: 10.48550/arXiv.2211.08879.

O. M. Smirnov. Revisiting the radio interferometer measurement equation. IV. A generalized tensor formalism. , 531:A159, July 2011. doi: 10.1051/0004-6361/201116764.

O. M. Smirnov, B. W. Stappers, C. Tasse, H. L. Bester, H. Bignall, M. A. Walker, M. Caleb, K. M. Rajwade, S. Buchner, P. Woudt, M. Ivchenko, L. Roth, J. E. Noordam, and F. Camilo. The RATT PARROT: serendipitous discovery of a peculiarly scintillating pulsar in MeerKAT imaging observations of the Great Saturn - Jupiter Conjunction of 2020. I. Dynamic imaging and data analysis. , 528(4):6517–6537, Mar. 2024. doi: 10.1093/mnras/stae303.

U. A. M. Sob. *Calibration and Imaging with Variable Radio Sources*. PhD thesis, Rhodes University, 2017.

L. S. Sparke and J. S. Gallagher. *Galaxies in the universe : an introduction*. Cambridge Univ. Press, Cambridge, 2010. ISBN 9780521671866.

C. N. Tadhunter, R. Morganti, S. di Serego Alighieri, R. A. Fosbury, and I. J. Danziger. Optical spectroscopy of a complete sample of southern 2-JY radio sources*. *Monthly Notices of the Royal Astronomical Society*, 263(4):999–1022, 1993. doi: 10.1093/mnras/263.4.999.

J. R. Taylor. *An Introduction to Error Analysis: The Study of Uncertainties in Physical Measurements*. University Science Books, Sausalito, CA, 2nd edition, 1997.

A. R. Thompson, J. M. Moran, and G. W. Swenson. *Interferometry and synthesis in radio astronomy*. Wiley, 2001.

A. R. Thompson, J. M. Moran, and G. W. Swenson. *Interferometry and Synthesis in Radio Astronomy*. Springer International Publishing, Cham, 3rd edition, 2017. ISBN 978-3-319-44431-4.

S. J. Tingay, D. L. Jauncey, E. A. King, A. K. Tzioumis, J. E. Lovell, and P. G. Edwards. Atca monitoring observations of 202 compact radio sources in support of the vsop agn survey. *Publications of the Astronomical Society of Japan*, 550(2):351–384, 2003. doi: 10.1093/pasj/55.2.351.

M. Tucci, J. A. Rubiño-Martin, R. Rebolo, R. Genova-Santos, R. A. Watson, R. A. Battye, K. A. Cleary, R. D. Davies, R. J. Davis, K. Grainge, M. Hobson, R. D. E. Saunders, A. Scaife, and P. F. Scott. Multifrequency spectral analysis of extragalactic radio sources in the 33-ghz vsa catalogue: sources with flattening and upturn spectrum. *Monthly Notices of the Royal Astronomical Society*, 386(3):1729–1738, 04 2008. ISSN 0035-8711. doi: 10.1111/j.1365-2966.2008.13161.x. URL https://doi.org/10.1111/j.1365-2966.2008.13161.x.

S. A. Tyul'Bashev and P. A. Chernikov. Physical Conditions in Steep-Spectrum Radio Sources. *Astronomy Reports*, 44(5):286–297, May 2000a. doi: 10.1134/1.163852.

S. A. Tyul'Bashev and P. A. Chernikov. Physical Conditions in Steep-Spectrum Radio Sources. *Astronomy Reports*, 44(5):286–297, May 2000b. doi: 10.1134/1.163852.

M. P. Véron-Cetty and P. Véron. A catalogue of quasars and active nuclei: 12th edition. , 455(2):773–777, Aug. 2006. doi: 10.1051/0004-6361:20065177.

G. L. Verschuur. *The invisible universe: the story of radio astronomy*. Springer, 2007.

S. J. Wagner and A. Witzel. Intraday Variability In Quasars and BL Lac Objects. , 33: 163–198, Jan. 1995. doi: 10.1146/annurev.aa.33.090195.001115.

J. V. Wall and C. R. Jenkins. *Practical Statistics for Astronomers*. Cambridge Observing Handbooks for Research Astronomers. Cambridge University Press, 2003.

R. L. White and R. H. Becker. A New Catalog of 30,239 1.4 GHz Sources. , 79:331, Apr. 1992. doi: 10.1086/191656.

A. Witzel, J. Schmidt, I. I. K. Pauliny-Toth, and U. Nauber. 21 cm flux density measurements of sources from the NRAO-MPIfR 6 cm surveys. , 84:942–945, July 1979. doi: 10.1086/112496.

A. Wright and R. Otrupcek. Parkes Catalog, 1990, Australia telescope national facility. *PKS Catalog (1990*, page 0, Jan. 1990.

A. E. Wright, M. R. Griffith, B. F. Burke, and R. D. Ekers. The Parkes-MIT-NRAO (PMN) Surveys. II. Source Catalog for the Southern Survey (-87.5 degrees < δ < -37 degrees). , 91:111, Mar. 1994. doi: 10.1086/191939.